TECHNISCHE UNIVERSITÄT MÜNCHEN
Fakultät für Maschinenwesen
Lehrstuhl für Nukleartechnik

Development and Application of a Fourier Transform based Methodology for the Identification of Instability in Boiling Water Reactors at a local Scale

Stefan Franz Walser

Vollständiger Abdruck der von der Fakultät für Maschinenwesen der Technischen Universität München zur Erlangung des akademischen Grades eines

Doktor-Ingenieurs

genehmigten Dissertation.

Vorsitzender:	Univ.-Prof. Dr.-Ing. Georg Wachtmeister
Prüfer der Dissertation:	1. Univ.-Prof. Rafael Macián-Juan, Ph.D.
	2. Prof. Dr.-Ing. Rafael Miró-Herrero Universidad Politécnica de Valencia / Spanien

Die Dissertation wurde am 19.09.2016 bei der Technischen Universität München eingereicht und durch die Fakultät für Maschinenwesen am 06.04.2017 angenommen.

Erklärung

Hiermit versichere ich, die vorliegende Arbeit selbstständig und ohne Hilfe Dritter angefertigt zu haben. Gedanken und Zitate, die ich aus fremden Quellen direkt oder indirekt übernommen habe, sind als solche kenntlich gemacht. Diese Arbeit hat in gleicher oder ähnlicher Form noch keiner Prüfungsbehörde vorgelegen und wurde bisher nicht veröffentlicht.

Ich erkläre mich damit einverstanden, dass die Arbeit durch den Lehrstuhl für Nukleartechnik der Öffentlichkeit zugänglich gemacht werden kann.

München, den 14. September 2016

Stefan Walser

Abstract

This thesis addresses the development of an analysis methodology for BWR instability phenomena and aims at the identification of in-core, local thermal-hydraulic processes during a transient. The analysis methodology is designed to apply as input data the simulation results of time domain coupled system codes. For the application described in this thesis, a coupled TRACE/PARCS model representing the Oskarshamn-2 (O2) NPP with a one-to-one core channel representation has been used. The coupled model simulates the O2-1999 feedwater transient; an instability event characterized by an in-phase mode of oscillation with reactor power amplitudes up to 132 %.

The analysis methodology is a two-step approach and uses in the first step the fast-fourier transform algorithm applied on normalized core parameters in two-dimensional spacial direction of the core. The normalization of the data implies the advantage of directly comparable results in spectral representation. The spectral analysis results show for each data node the oscillation amplitude to its corresponding frequency. In the second step the dominating frequency of each single parameter is determined and the relative phase shift of the dominating components is calculated.

The application of the developed methodology on the simulation results of the O2-1999 feedwater transient show that the channel mass flow rates have among all investigated parameters the clearest differences in the local expression of oscillation and are a governing indicator for BWR instability due to the density wave mechanism. The spectral analysis of the core channel in planar direction points out a heterogeneous oscillation behavior of the fuel assemblies mass flow rates. A

certain pattern of core channels with striking mass flow rate oscillations is prevailing and the pattern shows proportionality to the fuel assemblies relative power ratio. Moreover the mass flow rate oscillations of the peripheral core channels are observed to employ a quasi out-of-phase behavior with the central core channels, concluding a positive feedback for the growth of the core mass flow oscillation.

Acknowledgment

The present work was performed during the time as a research assistant at the Department of Nuclear Engineering under the direction of Prof. Rafael Macián-Juan to whom I would like to express my special thanks for giving me the opportunity to perform this work and for his valuable support and scientific input.
Many thanks are also dedicated to Prof. Rafael Miró-Herrero who kindly accepted the role of an examiner of this dissertation and especially for hosting me several times at Universitat Politècnica de València where I could gain very helpful insight for my research.
I would like to thank the organizers of the Oskarshamn-2 Benchmark for providing the data and model input.
My thanks go to my department colleagues and all my students who supported and influenced this work and also contributed to a friendly working atmosphere at the department.
Special thanks are given to my friends Sabin Ceuca, Sean Roshan and Jakob Wasza for providing in many ways very important support, input and the fruitful discussions.
Last but not least I want to express my sincere thanks to my family, my parents Renate and Franz and my brother Florian who gave me strength and support and encouraged me in all situations.

Contents

List of Figures

List of Tables

List of Acronyms

BC Boundary Condition

BWR Boiling Water Reactor

CFL Courant-Friedrich-Levy Number = $\frac{v\Delta t}{\Delta x}$

DFT Discrete Fourier Transform

FFT Fast Fourier Transform

FW Feedwater

IFFT Inverse Fast Fourier Transform

LOCA Loss of Coolant Accident

LWR Light Water Reactors

NK Neutron Kinetik

NPP Nuclear Power Plant

O2 Oskarshamn-2

PARCS Purdue Advanced Reactor Core Simulator

PDE Partial Differential Equation

PWR Pressurized Water Reactor

ROMs Reduced Order Models

RPV Reactor Pressure Vessel

TRACE TRAC/RELAP Advanced Computational Engine

TUM Technische Universiät München

USNRC U.S. Nuclear Regulatory Commission

Chapter 1

Introduction

The worldwide Boiling Water Reactor (BWR) fleet includes more than 80 operating units, in which water is evaporated directly in the reactor core and the produced steam directly drives a steam turbine. Such a power plant design thus transforms fission power into electrical energy by using only a relative simple industrial system.

Since the early days of the BWR technology, concerns were risen about the possibility of thermal-hydraulic oscillations and coupled thermohydraulic-neutronic instabilities with the major concern on the fuel cooling efficiency and the cladding integrity. After the first occurred instability events, authorities in all countries operating this power plant design requested specific analyses and changes in the procedures and plant safety features. As an example, it is common practice to avoid operating regions where power oscillations could occur.

However, over the last 35 years several BWR instability events occurred that are summarized in Table 1.1. Some of these events were inadvertent whereas others were intentionally induced as an experiment. The most probable type of instability has been the coupled neutronic-thermohydraulic instability that results in power oscillations at a frequency 0.4 - 0.5 Hz and has its roots in the density wave mechanism [7].

The main objectives of BWR stability analysis covers the assessment of stability margins, the prediction of the transient behavior in the case of an unstable condi-

tion and the prevention and mitigation of consequences of instabilities due to the design and the assessment of countermeasures.
For the BWR coupled nuclear and thermal-hydraulics analysis, three approaches are in general applied, namely Frequency Domain analysis, Time Domain analysis, and Bifurcation analysis that are briefly described by D'Auria in the following reference [5].
The Frequency Domain approach is designed to analyze the linear stability of BWRs and considers linear equations rather than the full set of differential equations. By applying a perturbation followed by a Laplace transformation of the neutron kinetic equations, the dynamics of the fission power are easily turned into the the linear model for BWR stability.
In Time Domain analysis, specifically developed analysis tools are included in time-domain codes to simulate the transient behavior of plant systems. These codes are based on simulation techniques that numerically integrate the partial differential equations describing the physical time dependent system behavior and have the capability to cope with the non-linear character of BWRs.
The Bifurcation Analysis represents a tool for the stability analysis of non-linear dynamic systems. In the context of BWR stability analysis, usually bifurcation codes are coupled with simplified time domain codes of reduced complexity, so-called Reduced Order Models (ROMs). The stability and semi-analytical bifurcation analysis methods encounter both sub- and super-critical Hopf bifurcations in different regions of the parameter space. Moreover, information on the type of oscillation mode (in-phase or out-of-phase) is obtained by analyzing the properties of the system's eigenvector elements .

In the time-domain analysis many models and computer codes have been developed over the past several years. In most of the work done so far, stability analysis has usually been carried out by evaluating the decay ratios and oscillation frequencies [8]. Real plant conditions leading to BWR instability are founded in a combination of dynamic multi-disciplinary subjects that include thermal-hydraulics, neutronics, fuel dynamics, heat transfer, ex-core systems, plant control systems and many

others. As many as possible of these feed-backs can be taken into account when applying coupled system codes incorporating three-dimensional neutron kinetics together with thermal-hydraulic system codes for stability analysis. This makes possible the development of simulation models, which include a reactor core with a one-to-one fuel assembly representation and allow the study of in-core thermal-hydraulic local effects during a BWR instability event.

From this capability derives the scope of this work, namely the development of a coupled thermal-hydraulic and neutron-kinetic model with the coupled computer codes TRACE and PARCS. The reactor core fuel assemblies are represented one-to-one with the real lay-out in the model. The actual nuclear reactor considered is the Oskarshamn-2 NPP. The BWR instability event analyzed in this thesis with the coupled model is the O2-1999 feedwater transient. It represents the basis for a further detailed analysis of the in-core local thermal-hydraulic phenomena during the stability event.
For the analysis of local parameters, a post-processing method of the results of the simulation is developed, which applies a Fourier-transform based approach and identifies the differences between local core parameters. The capabilities of the method are tested on the simulation results of the O2-1999 feedwater transient and a further generic case.

Date	NPP, Country, Manufacturer	Event
30.06.1982	Caorso, Italy, GE (General Electric)	It occurred during startup of the reactor. The reactor thermal power was 53.5% and the recirculation flow 38%. The operating point of the reactor entered the unstable region, the oscillations diverged and the reactor scrammed on high-high APRM signal (120% power).
13.01.1984	Caorso, Italy, GE	The second event occurred after trip of a recirculation pump and following loss of some preheater trains. The cold feed water and the strongly peaked axial power distribution led to neutron flux oscillations.
13.01.1984	TVO-I, Finland, ABB Atom	A power oscillation event took place when the plant was brought back to power after a short shutdown period. The reactor power was about 60% with a recirculation flow of 30% when increased APRM signal oscillations started to appear.
09.03.1988	LaSalle 2, USA, GE	Underwent a dual recirculation pump trip following which the unit experienced excessive neutron flux oscillations while it was in natural circulation. The resulting perturbation on the switches for anticipated transient without scram resulted in a trip of both recirculation pumps.
15.01.1989	Forsmark 1, Sweden, ABB Atom	After having carried out tests in several of the selected operating points, the stability boundary was very close. Moving from one point to another, the operator chose to switch from the pump speed control mode to the power control mode. This was done at 71% power and 4700 kg/s. A remaining control mismatch led to a small decrease in core flow. The combined effect of the power control system, caused power oscillations with an amplitude that increased to about +-20% after 20 s, enough the initiate a pump run-down.
26.10.1989	Ringhals 1, Sweden, ABB Atom	In 1989 these NPP was starting up for a new cycle, power oscillations were observed in the core. During the oscillation, several LPRMs gave a high level alarm, indicating that the local power in those positions had exceeded 118 %. The core was stabilized about 30 seconds after the partial scram.
08.01.1990	Oskarshamn 2, Sweden, ABB Atom	A planned power reduction from 106% to 65% was performed. The power was reduced by reducing pump speed to minimum. After about 1 minute, power oscillations had developed, having peak-to-peak amplitudes of +-10%. The APRM signals showed the oscillations to be in phase. A manual partial scram was performed which completely quenched the oscillations.
29.01.1991	Cofrentes, Spain, GE	Oscillations appeared after the operator withdraw control rods and reduced core flow in order to transfer the recirculation pumps from low to high speed.
03.07.1991	Isar 1, Germany, Siemens	The Isar 1 NPP had a trip of four internal recirculation pumps, due to a reduction in seal water flow to the 8 recirculation pumps. The power reduction due to the control rod insertion proved to be too slow to prevent the reactor from entering the unstable region of the power-flow map. Neutron flux oscillations with increasing amplitude appeared at about 50% power and 30% core flow. When the oscillations reached peak-to-peak amplitude of 30%, corresponding to a peak power of 67.5 % at 30 % flow, the reactor scrammed on the undelayed setpoint of neutron flux to core flow ratio. This occurred 44 seconds after the trip of the four recirculation pumps.
15.08.1992	WNP 2, USA, GE	The WNP 2 experienced power oscillations during startup. The event occurred early in cycle 8 operation. Upon recognizing the power oscillations, the operators manually initiated a reactor scram. Post event review indicated that the oscillations were inphase and had grown to peak-to-peak amplitude of about 25 % of rated power.
09.07.1993	Perry, USA, GE	Entry into a region of core instability.
01.1995	Laguna Verde 1, Mexico, GE	During startup of the reactor, at 34% power, the operator was waiting to increase pump recirculation speed. Power was increased to 37% by control rod withdrawal and closure of the control valves of the pumps was initiated, thus leading to power reduction. During these operations the operator observed power oscillations with a tendency to diverge and he stopped the closure of the valves. At this time the peak-toppeak amplitude in the oscillations was 6%.
17.07.1996	Forsmark 1, Sweden, ABB Atom	Local oscillations due to a bad seated fuel assembly.
08.02.1998	Oskarshamn 3, Sweden, ABB Atom	Power oscillations due to a bad combination of core design and control-rod pattern during start up.
25.02.1999	Oskarshamn 2, Sweden	Power oscillations after a turbine trip with pump runback.

Table 1.1: Summary of reported BWR instability events [5].

Chapter 2

BWR Instability - Background

The topic of coupled thermohydraulic-neutronic instabilities in boiling water nuclear reactors is explained in detail in March-Leuba and Rey [7], March-Leuba [1], Lahey and Moodey [9] and is summarized in this chapter.
A variety of types of instabilities have to be considered in heated channels with a two-phase flow regime and can be broadly categorized as static and dynamic instabilities.
The static instabilities are explainable according to steady-state laws and have in common the existence of two equilibrium points between the system tends to "jump". Examples of the static instabilities are flow excursion instabilities, flow regime "relaxation" instabilities and geysering or chugging.
Dynamic instabilities require the use of dynamic conservation equations and feedback control analysis. The prevailing examples of dynamic instabilities in BWR technology are density-wave oscillations, pressure drop oscillations and flow regime induced instabilities.

2.1 Densitsy-Wave Oscillations

In commercial BWRs, the most common instability is the density-wave instability, also referred to as "the channel flow instability". It can be described as follows:

The coolant flows upwards through the BWR core as is guided by bundle boxes surrounding the fuel pin lattices. If variations in the density of the fluid at the bottom part of the channel occur, then these variations travel upwards with the flow along the core channel. For example, considering a constant channel power and a decrease in inlet flow results in an increase in void formation in this particular channel. The resulted void packet produces a change in the local pressure drop at each axial location while traveling upwards along the core channel. A propagating density wave is then formed, which is delayed axially by the density-wave propagation time, that is, the effective time for the voids to move upwards along the core. In two-phase flow regimes the local pressure drop is very sensitive to local void fractions, especially at the outlet of the channels, where it reaches its highest values, thus leading to large local pressure drops. With respect to the original perturbation at the inlet, a significant part of the pressure drop is delayed at the channel outlet.

Figure 2.1 illustrates the density wave mechanism with a sinusoidally perturbed

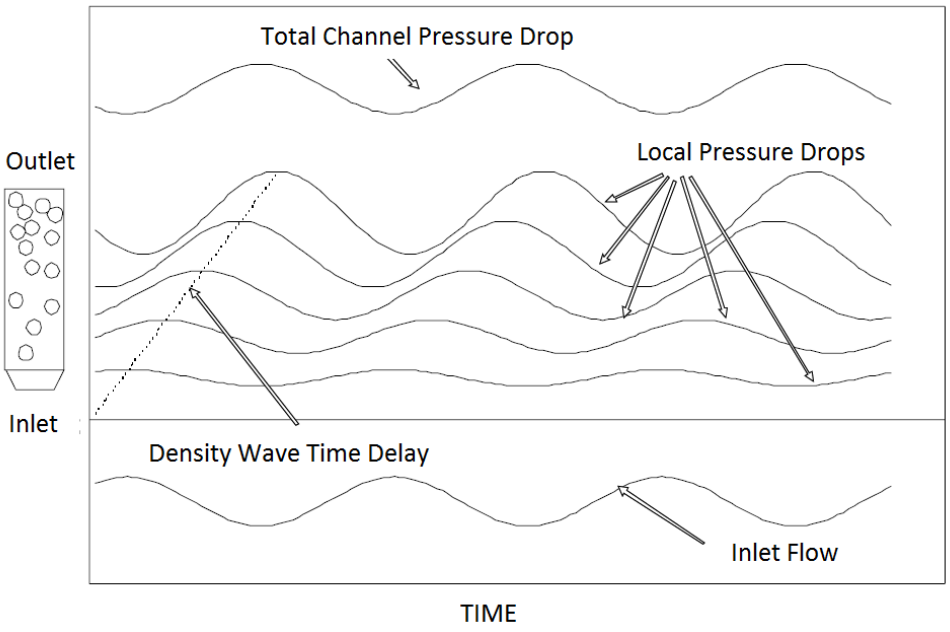

Figure 2.1: Density wave mechanism: inlet flow perturbation, local pressure drop delay and total channel pressure drop [1].

inlet flow and local pressure drops which are also sinusoidal but delayed with respect to the inlet flow. The local pressure drops sum up along the channel to the total pressure drop, which has also a sinusoidal form and is also delayed with respect to the inlet flow perturbation. The total pressure drop may be delayed by 180° with respect to the inlet flow if the condition that the channel outlet pressure drop is larger than the inlet pressure drop is fulfilled. Consequently, an increase in the inlet mass flow rate results in a decrease of the total channel pressure drop, as it is the case in Figure 2.1. Thus, the channel flow is unstable and any inlet flow perturbation has a positive feedback on itself, with the result that oscillations grow at an unstable frequency. When the delayed local outlet pressure drop equals the pressure drop at the inlet at a particular frequency, the critical point, at which the channel flow instability starts, is reached resulting in an effective zero friction at that frequency where any perturbation is self sustaining for that particular channel. The relative flow stability of a channel is dependent on the magnitude of inlet flow feedback, that is governed by the channel boundary conditions. It is distinguished between the following three main types of boundary conditions:

A constant-pressure drop boundary condition occurs when a single channel becomes unstable within an arrangement with a huge amount of parallel channels that forcing the boundary condition to remain essentially constant. This results in the largest number of feedback flow oscillations required to maintain the constant pressure drop and is therefore the most unstable boundary condition among these three types.

A variable pressure drop boundary condition is prevailing when the recirculation loop and the pump dynamics determine the channel inlet flow conditions. In this case, a pressure balance between the channel pressure drop and the pressure drop across the recirculation loop plus the pressure gain at the pump exists for a particular channel flow and loop flow. According to the recirculation-loop dynamics, the pressure drop across the channel is allowed to oscillate and the inlet flow feedback is not as strong as in the constant-pressure-drop boundary condition.

A constant-inlet-flow boundary condition can be obtained in a test section by having a displacement pump forcing a constant inlet flow through the channel,

regardless of pressure. Because the inlet flow is constant, channel oscillations are impossible and, therefore, this is the most stable boundary condition.
As a summary, a thought experiment can be carried out: a constant-pressure-drop boundary condition is assumed together with an unstable channel that has an effective negative friction coefficient at a given frequency. Then, the inlet flow increases due to a perturbation. The negative effective friction coefficient would tend to decrease the pressure drop but in order to compensate for it and keep the pressure drop constant, the channel's inlet flow has to increase further, causing a runaway instability. However, the effective negative friction coefficient is only negative at a particular frequency and the flow increase only happens at that particular frequency. That means, that the instability results from an oscillation at that unstable frequency with growing amplitude.

2.2 Neutronic Feedback During Oscillations

In BWRs the generation of power correlates with the neutron flux, which is a function of the reactivity feedback. Therefore, it is strongly dependent on the core average void fraction. Consequently, the power oscillates according to the neutronic feedback when a void fraction oscillation is established in a BWR. Figure 2.2 illustrates the coupled neutronic / thermal-hydraulic feedback path in a BWR. The key factors can be grouped in the following classes:

- NEUTRONICS: the neutron dynamics determines the power generation in the fuel as a response to the reactivity feedback resulting from the void fraction distribution, doppler reactivity and control rod reactivity.
- FUEL: the fuel dynamics determines the heat flux from the fuel to the coolant.
- CORE T-H: the channel thermal-hydraulics characterizes the void fraction as a function of the heat flux.
- RECIRCULATION LOOP: the recirculation loop imposes the core thermal-hydraulic boundary conditions.

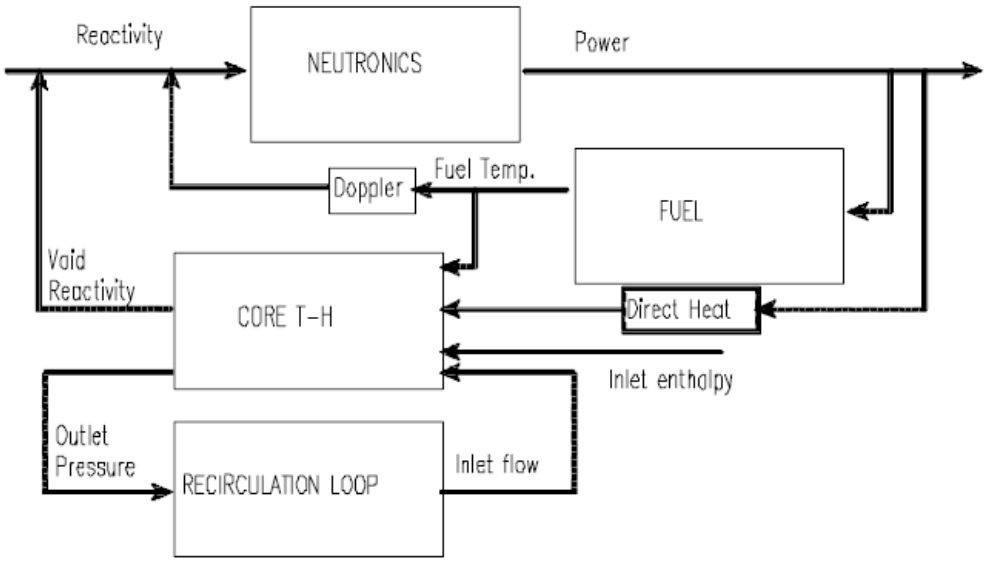

Figure 2.2: Coupled neutronic/thermal-hydraulic feedback in a BWR [1].

An important difference between neutronic feedback and flow feedback arises from the fuel transfer function. When the power is generated in the fuel pellets, it first has to change their temperature to alter the heat flux from the fuel to the coolant, before the power can exert a feedback through the moderator density. This response of the fuel is relatively slow with a time constant between 6 s and 10 s and, thus, the fuel adds a phase delay to the feedback what has a destabilizing effect. Otherwise the fuel has a stabilizing effect due to its inherently filtering of the oscillation amplitude at frequencies higher than 0.1 Hz. It has been shown that the destabilizing effect is dominant and by decreasing the time response of the fuel, through smaller diameter fuels or by increasing the pellet-clad gap conductance, an unstable situation is reached.

2.3 Different Modes of Instability and their Sensitivity to physical Parameters

The most important physical mechanism for observed instability in commercial BWRs is the density-wave oscillation. Three types of instability modes have their

roots in the density-wave mechanism: the core-wide or so called in-phase mode, the regional or so called out-of-phase mode, and the channel thermal-hydraulic instability mode.

2.3.1 Core-Wide Instability Mode

In the fundamental (core-wide) mode of oscillation, the total core inlet flow oscillates in phase with the total core pressure drop, that is, the entira core behaves as a unit. This means that any change in power is accompanied by a change in inlet flow. Figure 2.3 illustrates the high flow intensity and high core pressure drop at a time t and the low flow intensity and low pressure drop at a time $t + T/2$.

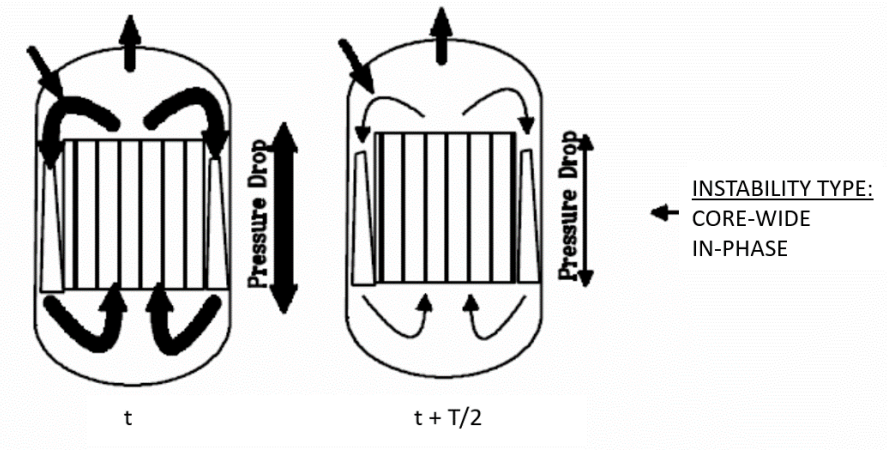

Figure 2.3: Flow pattern for the IN-PHASE mode [1].

In order to obtain an in-phase instability it is generally necessary to decrease the stability in a BWR. This is feasible by increasing the neutronic feedback and by increasing the instability of the density-wave mechanism. The main parameters affecting the core-wide instability mode are:

- Average Void Fraction — operating conditions with higher void fraction have, because of the increased density reactivity coefficient, a stronger neutronic feedback and a larger two-phase pressure drop, and both effects favor the destabilization of the reactor.

- Axial Power Shape — bottom-peaked power shapes tend to increase the axially averaged void fraction and are, therefore, more unstable. Furthermore, as void perturbations start at a lower axial level, a larger time delay is induced.
- Radial Power Shape — the radial power shape considers inherent non-linearities that affect BWR stability. The channel with the highest power is the most unstable channel and, therefore, tends to comprehensively dominate the core oscillatory response, rather than being averaged with the low-power channels.
- Void Velocity — operating conditions should be more unstable, as lower void velocities result in longer delay times for the density wave.
- Inlet Fluid Subcooling — a decrease in the inlet fluid sub-cooling tends on one hand to increase the operating power level which has a destabilizing effect, and on the other hand the boundary of boiling onset is raised, which decreases the density time-delay. Overall the destabilizing effect of the decrease in inlet fluid subcooling is dominating.
- Fuel Gap Conductance — the higher the gap conductance, the higher the amount of power that is deposited in the channel coolant during a neutron flux oscillation, thus resulting in a destabilizing effect.
- Fuel Isotopic Composition — the fuel isotopic composition affects the density reactivity coefficient and depends on burn-up and operating conditions. For this reason, this indirect effect is difficult to predict.

2.3.2 Out-Of-Phase Instability Mode

In the out-of-phase oscillation mode a constant total core inlet flow is maintained and the total core pressure drop is constant. While individual channels increase their flow, opposite channels decrease their flows by the same amount, as schematically presented by the turning in direction of the central arrow in Figure 2.4. This phenomenon allows large flow oscillations within each channel and significantly decreases the reactor's stability.

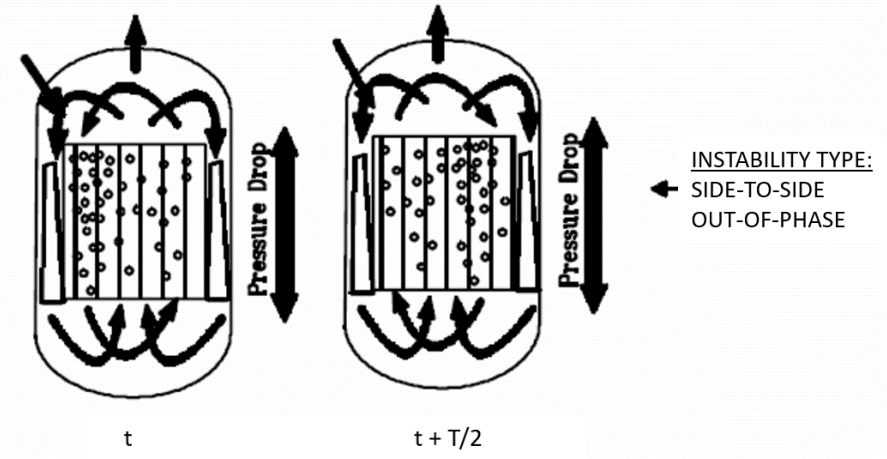

Figure 2.4: Flow pattern for the OUT-OF-PHASE mode [1].

The out-of-phase instability mode is more probable if the sub-critical reactivity value of the out-of-phase mode is reduced or if conditions for out-of-phase density-wave oscillations are likely:

- Low Geometric Buckling — larger cores tend to have more out-of-phase instabilities than smaller cores due to the direct proportionality of the subcritical mode to the difference between the geometric bucklings of the fundamental and subcritical modes.
- High Fission Cross Section — the out-of-phase mode is more likely dominant when the fission cross section is high, as the subcritical mode reactivity is inversely proportional to the fission cross section.
- High Pressure Drop across the Channel — higher core pressure drops favor the out-of-phase density-wave mechanism over the in-phase mechanism due to increased flow feedback.
- High Flow Rate — higher flow rates result in significantly higher friction pressure drops, thus favoring the out-of-phase instability.
- High Friction in the Recirculation-Loop Flow Path — Higher friction in the recirculation-loop's flow paths reduces the flow feedback for in-phase mode and thus favors the out-of-phase mode.

- Highly-Bottom-Peaked Axial Power Shapes — power-shapes that are very highly-bottom-peaked have the effect of a reduction of adjoint weighting at the upper part of the channel, which results in a decrease of the reactivity's neutronic feedback and, therefore, the density-wave flow instability mode is enhanced. This can be the case for axial shapes with peaking factors above 1.6.

- Low Single-Phase Friction — the likelihood of density-wave flow oscillations is increased for plants with loose inlet orifices.

2.3.3 Single Channel Thermal-Hydraulics Instability

The single-channel flow instability is characterized by a single channel with inlet flow oscillations while the total core flow and core pressure drop is essentially constant due to the control of the large number of stable channels as illustrated in Figure 2.5.

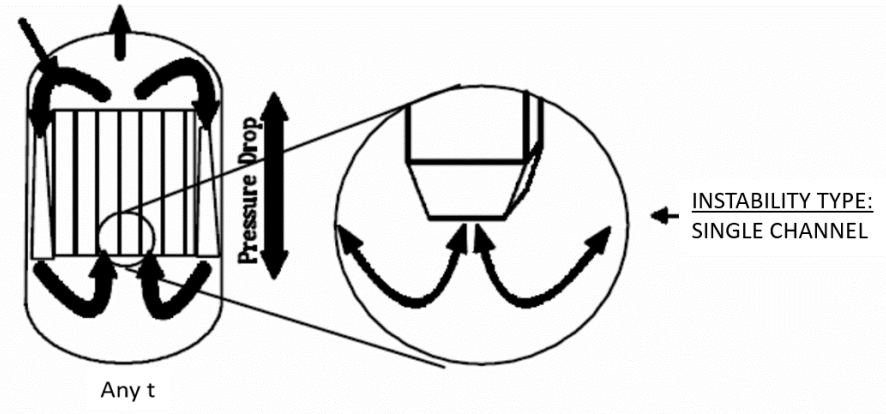

Figure 2.5: Flow pattern for the SINGLE CHANNEL mode [1].

Chapter 3

BWR Stability Event based on the Oskarshamn-2 NPP 1999 Feedwater Transient

This work is based on the data provided through the "OECD/NEA Oskarshamn-2 (O2) BWR Stability Benchmark for Coupled Code Calculations and Uncertainty Analysis in Modelling". The events in the Oskarshamn-2 NPP and the resulting transient are described next.

The Oskarshamn-2 boiling water reactor suffered a stability event on February 25, 1999. The accompanying measurement data with marked event points (Point 1 to 12) are shown in Figure 3.1 that presents the total reactor power, the recirculation mass flowrate, the feedwater temperature, the mass flowrate of the feedwater and of the steam line, the pressure in the feedwater line, in the steam dome and in the steam line, and the reactor water level. The corresponding power/flow map with the marked event points is presented in Figure 3.2.

The plant was operating at full power and minimum recirculation flow while maintenance work was performed on the switchyard outside of the power plant. After completion of work, the normal electric supply was restored. During this action a 150 millisecond power interruption occurred while operating a breaker. The control logic interpreted this interruption as load rejection and caused a turbine

trip, however the load rejection signal was not transmitted to the reactor due to a failure in the relay circuit (Point 1).
The reactor remained at full power and the expected automatic control actions like automatic control rod insertion and main recirculation pump trips did not occur while the generator output power level decreased from 625 MWe to 585 MWe and the excess steam was bypassed directly into the main condenser. In consequence of this turbine trip and the opening of the steam bypass valves, the feedwater preheater system was inoperable and the feedwater temperature decreased. The feedwater temperature decreased by 75 °C within 150 seconds and therefore colder water entered the reactor resulting in a positive reactivity feedback insertion with an increase of the core power level. When the reactor power increased more than 2 % above nominal power level of 106 %, the main recirculation flow was reduced by a pump controller, controlling the rotation of the recirculation pumps, and thereby the power level was reduced (Point 2).
As the cold feedwater continued to enter the reactor vessel and the power level increased again above 108 %, the recirculation flow reduction was repeated a second (Point 4) and third (Point 6) time.
As the event is characterized by an increase in reactor power and a decrease in reactor flow, the operators performed a partial scram by fully inserting seven predefined control rods (Point 8) and reducing core flow to the minimum (Point 9). The partial scram was performed 123 seconds after the initiation of the event and resulted in a reactor power level of 65 % and core flow of 3200 kg/s.
The flow of cold feedwater in the reactor continued and reactor power increased again and the unstable region of the power/flow map was entered (Point 11). This resulted in the onset of power oscillations with increasing amplitudes over a period of 20 seconds until the reactor was automatically scrammed due to high power (Point 12). The scram occurred 3 minutes and 6 seconds after the initiating load rejection event, when the power exceeded 132 % at 2500 kg/s recirculation flow. The scram was performed according to the design, disconnecting the NPP from the main electric grid and thus setting the reactor into the hot shutdown state. [2]

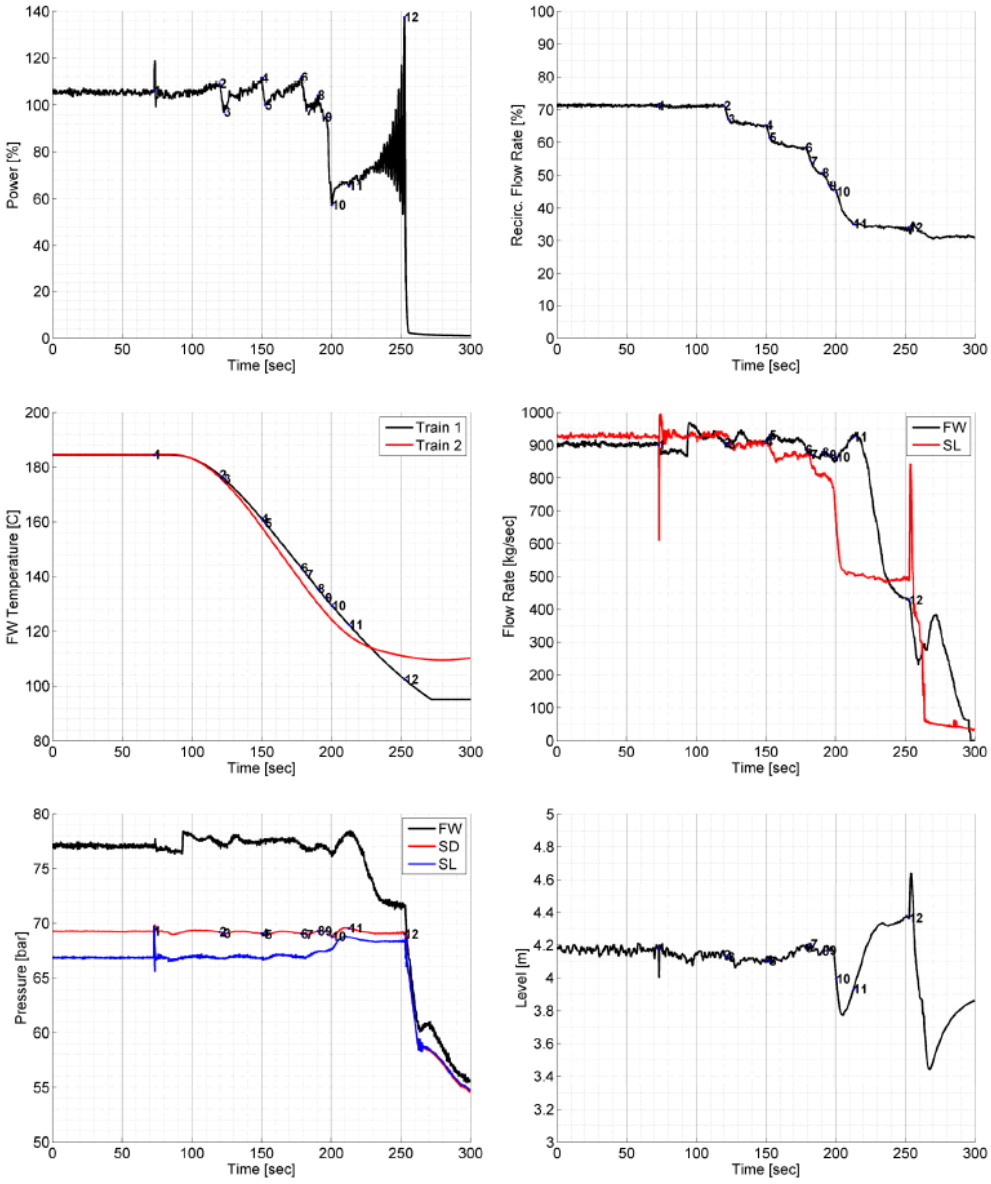

Figure 3.1: Oskarshamn-2 February 25, 1999 feedwater transient measurements [2].

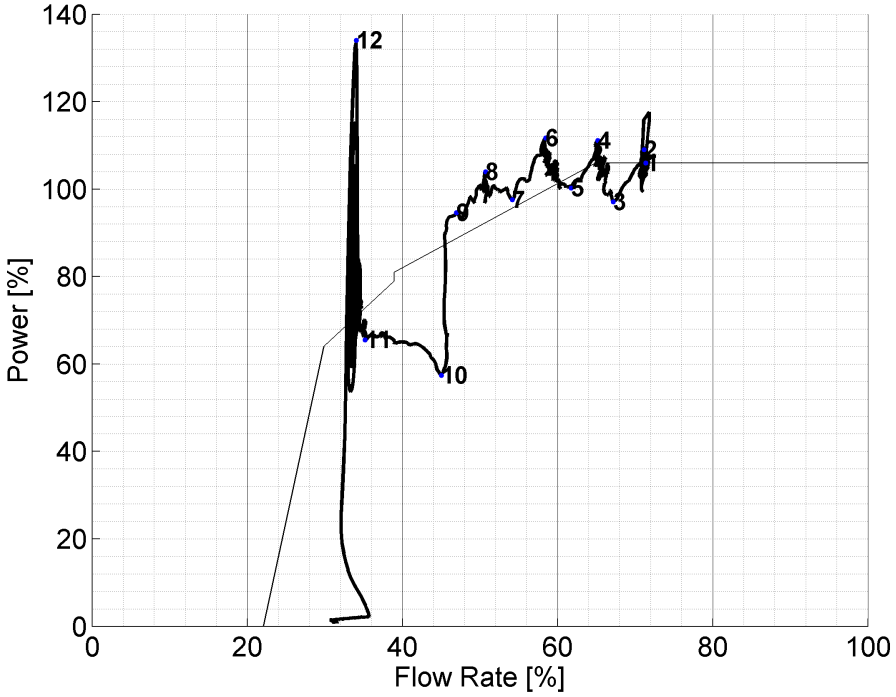

Figure 3.2: Oskarshamn-2 February 25, 1999 feedwater transient power-flow map [2].

Chapter 4

Applied Computer Codes

4.1 The Reactor System Analysis Code TRACE

TRAC/RELAP Advanced Computational Engine (TRACE) is the most advanced reactor system code developed by the U.S. Nuclear Regulatory Commission (USNRC). The applied code version in the scope of this work is TRACE Version 5 patch 3. This thermal-hydraulics system code combines the capabilities of the USNRC's four main system codes (TRAC-P, TRAC-B, RELAP, RAMONA) and has the capability to model thermal-hydraulic phenomena in one-dimensional (1-D) and three-dimensional (3-D) space.
TRACE has been designed to perform best-estimate analyses of steady-state and and transient behavior of light-water reactors such as large/small break loss-of-coolant accidents (LOCAs), operational transients, and other accident scenarios. Besides the analysis capabilities for Pressurized Water Reactors (PWRs) and Boiling Water Reactors (BWRs), it can also model phenomena occurring in experimental facilities [10].

4.1.1 Solution Methods and Field Equations employed by TRACE

To model steam/water flows, the basic two-fluid, a two-phase two-field equations set is employed, which consists of separate mass, energy and momentum conservation equations for the liquid and the gas fields, thus resulting in six partial differential equations (PDEs) in time and space.

The time averaged mass conservation equations have the form presented in Equations (4.1) and (4.2) for the liquid and gas phase:

$$\frac{\partial\left[(1-\alpha)\overline{\rho_l}\right]}{\partial t}+\nabla\cdot\left[(1-\alpha)\overline{\rho_l}\overline{\overrightarrow{V_l}}\right]=-\overline{\Gamma} \tag{4.1}$$

$$\frac{\partial(\alpha\overline{\rho_g})}{\partial t}+\nabla\cdot\left[\alpha\overline{\rho_g}\overline{\overrightarrow{V_g}}\right]=\overline{\Gamma} \tag{4.2}$$

The time averaged energy equations have the form presented in Equation (4.3) and (4.4) for the liquid and gas phase:

$$\begin{aligned}&\frac{\partial\left[(1-\alpha)\overline{\rho_l}\overline{(e_l+V_l^2/2)}\right]}{\partial t}+\nabla\cdot\left[(1-\alpha)\overline{\rho_l}\overline{(e_l+V_l^2/2)\overrightarrow{V_l}}\right]\\&=-\nabla\cdot\left[(1-\alpha)\overline{\overrightarrow{q_l'}}\right]+\nabla\cdot\left[(1-\alpha)\left(\overline{\top_l\cdot\overrightarrow{V_l}}\right)\right]+(1-\alpha)\overline{\rho_l}\,\overline{\overrightarrow{g}\cdot\overrightarrow{V_l}}-\overline{E_i}+\overline{q_{dl}}\end{aligned} \tag{4.3}$$

$$\begin{aligned}&\frac{\partial\left[\alpha\overline{\rho_g}\overline{\left(e_g+V_g^2/2\right)}\right]}{\partial t}+\nabla\cdot\left[\alpha\overline{\rho_g}\overline{(e_g+V_g^2/2)\overrightarrow{V_g}}\right]\\&=-\nabla\cdot\left[\alpha\overline{\overrightarrow{q_g'}}\right]+\nabla\cdot\left[\alpha\left(\overline{\top_g\cdot\overrightarrow{V_g}}\right)\right]+\alpha\overline{\rho_g}\,\overline{\overrightarrow{g}\cdot\overrightarrow{V_g}}+\overline{E_i}+\overline{q_{dg}}\end{aligned} \tag{4.4}$$

The time averaged momentum equations have the form presented in Equation (4.5)

and (4.6) for the liquid and gas phase:

$$\frac{\partial\left[(1-\alpha)\overline{\rho_l}\overrightarrow{\overrightarrow{V_l}}\right]}{\partial t}+\nabla\cdot\left[(1-\alpha)\overline{\rho_l}\overrightarrow{\overrightarrow{V_l}}\overrightarrow{\overrightarrow{V_l}}\right]=\nabla\cdot\left[(1-\alpha)\overline{\top_l}\right]+(1-\alpha)\overline{\rho_l}\,\overrightarrow{g}-\overrightarrow{\overrightarrow{M_i}} \tag{4.5}$$

$$\frac{\partial\left[\alpha\overline{\rho_g}\overrightarrow{\overrightarrow{V_g}}\right]}{\partial t}+\nabla\cdot\left[\alpha\overline{\rho_g}\overrightarrow{\overrightarrow{V_g}}\overrightarrow{\overrightarrow{V_l}}\right]=\nabla\cdot\left[\alpha\overline{\top_g}\right]+\alpha\overline{\rho_g}\,\overrightarrow{g}-\overrightarrow{\overrightarrow{M_i}} \tag{4.6}$$

In these conservation equations an overbar represents a time average, the subscript "g" gas specific terms and the subscript "l" liquid specific terms. The variables used for the description of the equations are: α: the gas volume fraction, ρ: the density, V: the magnitude of the velocity Γ: the interfacial mass-transfer rate (positive from liquid to gas), e: the internal energy, q': the heat flux, $\top$: the stress tensor, g: the magnitude of the gravity vector, E_i: the rate of energy transfer per unit volume across phase change, q_d: the power deposition directly to the gas or liquid (without heat-conduction process), and $\overrightarrow{M_i}$: the rate of momentum transfer per unit volume across phase interfaces.

Generally, there is a considerably difference between the general form of a conservation equation and its implementation in a computer code, which requires additional processing operations. The form of the above equations is therefore different from the form in which TRACE solves the field equations. In order to reduce the complexity of the numerical solution and the computation cost required, the conservative forms of the energy, mass, and momentum equations are modified in TRACE in order to provide a set of numerically equivalent energy and motion equations [11]. More in-depth information is provided in the TRACE Theory Manual [12].

Next a series of approximations made in TRACE and relevant to the work developed in this thesis are highlighted: (i) The volume average of a product is assumed to be equal to the product of volume averages; (ii) only contributions from wall heat fluxes and heat fluxes at phase interfaces within the averaging volume are usually included in the volume averages of the divergence of the heat flux, and (iii)

only contributions from the stress tensor due to shear at metal surfaces or phase interfaces within the averaging volume are considered [12].

TRACE discretizes the two-phase flow computational domain using finite volumes and solves the above mentioned PDEs in them. A semi-implicit, time-differencing technique evaluates the heat-transfer equations, while the fluid-dynamic equations in the spatial components use by default a multi-step time differencing procedure (SETS) that allows the material Courant-limit to be exceeded. Alternatively, a more straight forward semi-implicit (SI) time-differencing method is also available. In the SI approximation of the flow equations, the solution of the difference equations is represented by a rather straightforward set of steps in each stage. A first step evaluates all quantities dependent only on the state at the beginning of the time step, including heat-transfer, friction coefficients and physical properties such as viscosity and conductivity. The next step solves the algebraic difference equations and the final end steps generate the needed values for various other variables. The SETS method starts with a pre-pass step that calculates a solution of motion equations for "stabilizer" velocities. Then the semi-implicit equations for motion mass and energy are solved. In the final post-pass step the stabilizer mass and energy equations are solved.

4.1.2 TRACE modeling features

A reactor system is modeled in TRACE with various components. This so-called component-based approach allows to represent each physical piece of equipment in a flow loop by some typical components. Each model component is nodalized into a certain number of physical volumes (also called cells) over which the equations for fluid, conduction and kinetics are averaged and all quantities except for the velocities are centered in the hydrodynamic cell (cell-centered), and the velocities are cell-edge quantities, resulting in a staggered grid approach. The number of utilized components and the number of volumes within them is arbitrary and, theoretically, only limited by the available computer memory.

Among the various number of available TRACE components, a selection of the relevant components employed in the context of the work, is briefly described below.

PIPE Coolant flow in one directional for a tube, channel, duct or pipe is modeled in TRACE with a so-called PIPE component consisting of one or more cells (computational nodes). All quantities are centered in the hydrodynamic cell except the velocities, which are cell-edge quantities. It can model coolant flow-area changes, wall heat sources, wall heat transfer between the wall inner and outer surfaces, as well as, wall's conduction heat-transfer calculation with different material types available in the code. Wall friction and irreversible form losses caused by flow area changes are evaluated by specifying option values in the input. The PIPE's geometry is specified by volume and length provided for each computational cell, the flow area and hydraulic diameter at the cell edges. The PIPE can be connected to other components with the junction interface variables.

VESSEL The VESSEL component models the light water reactor vessel and the internals which include the downcomer, reactor core and upper and lower plenum. In order to evaluate the flow through and around all internals, a three-dimensional model can be used. Modeling options allow for the application of the VESSEL component in 3D cylindrical geometry, where the number of radial rings, azimuthal sectors and the number of axial levels is user defined. Internal structures can be modeled as restrictions of fluid flow areas at the cell faces and as reductions in fluid volumes when the cells are dimensioned. Based on the difference between the geometric dimensions of a cell and its fluid portion, flow-area restrictions, the volume occupied by structures within each mesh cell can be modeled. For example, by setting the appropriate cell-face flow-area fractions to zero, the downcomer wall can be modeled as shown in Figure 4.1 and, furthermore, flow-area fractions between zero and one are specified to model the flow restrictions at the top and the bottom core-support plates. One-dimensional hydraulic components can be connected to the VESSEL component internally as well as externally by specifying the pipe connections to the faces of the VESSEL cells.

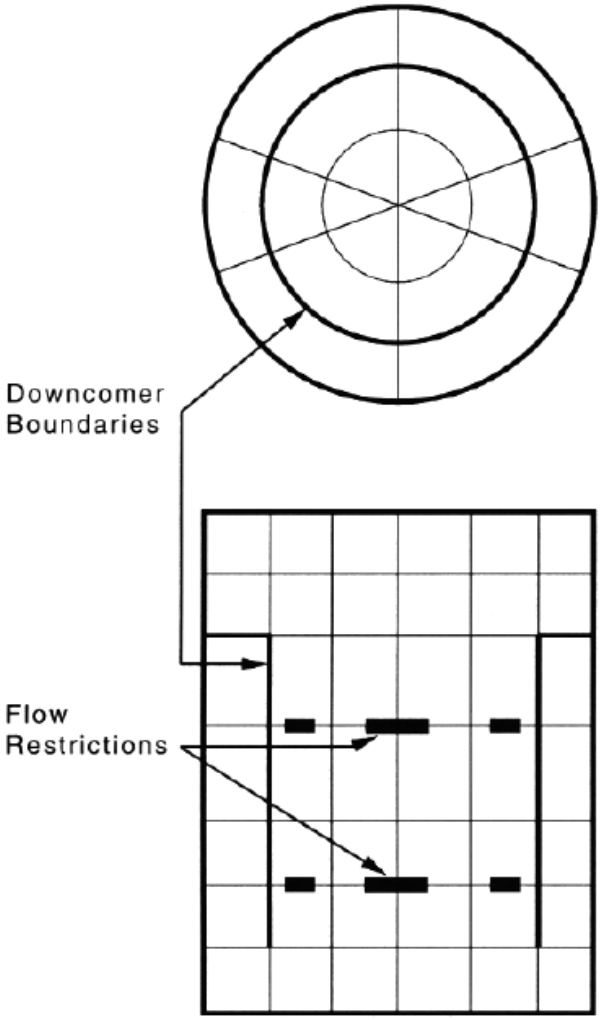

Figure 4.1: Flow restrictions and downcomer modeling [3].

PUMP The PUMP component represents a centrifugal pump and is modeled by a 1D hydraulic component. The pressure differential is calculated across the cell interface corresponding to the pump impeller and the pump impellers angular velocity as a function of the fluid flow rate and its properties. The model can simulate any centrifugal pump, while six types of pumps are selectable by the user. For example, the pump-impeller rotational speed can be specified by the control system and the user can specify the pump characteristic curves.

SEPD The steam separators and moisture dryers inside the reactor vessel of boiling water reactors are modeled with the SEPD component used in connection with internal junctions in a VESSEL component. The basic concept of the SEPD component represents a "black box" consisting of a control cell (the J-cell) with three junctions: the separator inlet junction considering two-phase mixture, the exit flow junction considering wet steam, and the discharge flow junction with a bulk of liquid with traces of gas. At the J-cell the separator model triggers a special solution in order to match the prescribed separator performance in terms of the x_{CO} (carry-over quality) and the x_{CU} (carry-under quality) specified values. There are various user options with different conceptual levels of the model, ranging from the simplest approach with user-defined constant x_{CO} and x_{CU} up to a mechanistic separator option, in which the separator performance is calculated by the code as a function of the local flow conditions.

FILL The FILL component is a boundary condition to model the flow into the system and it imposes a coolant velocity or a massflow boundary condition at it's junction with any other 1D component junction. There are different types of FILLs, for example boundary conditions can be varied individually by the control system as a function of time during transient calculations.

BREAK The BREAK component is a pressure boundary condition and represents the known hydrodynamic conditions at an actual physical location in the system. It is commonly used to specify the boundary condition in transient behavior and can impose a given pressure to one cell adjacent to the BREAK. Additionally, the pressure can be input as a series of interpolated value contained in tables as a function of time.

HTSTR The heat structure component HTSTR evaluates the heat transfer in fuel-rods or solid structure hardware elements by treating the dynamics of conduction, convection and gap-gas heat transfer. All fluid components (PIPE, CHAN, etc.) that model a pipe wall use the HTSTR component by internally spawning one or more HTSTR components for the evaluation of conduction and convection from the structure wall to the fluid.

RADENC The RADENC component models thermal-radiation heat transfer and is based on the radiation-enclosure method that evaluates radiative exchange between discrete surfaces of HTSTR components.

POWER The POWER component supplies HTSTR or CHAN components with power. The total power is optionally determined from a specified table of power, an initial power, point kinetics calculation or from 3D transient neutronics calculation performed by PARCS. In case of a coupled TRACE/PARCS calculation, the 3D power distribution is determined by PARCS, although in the TRACE model a POWER component is needed to set up the arrays that provide the PARCS power densities to TRACE heat structure. When the POWER component powers CHAN components that may have one or more HTSTR components, some input part of the POWER is specified in the input part of the CHAN component whereas an additional power distribution array is needed to identify the CHAN-to-CHAN

power distribution.

CHAN A BWR fuel assembly is schematically presented in Figure 4.2. The fuel assembly consist of a fuel bundle surrounded by a fuel channel box. The fuel bundles are generally a square array consisting the fuel rods with full length and part length as well as water rods, tie rods and hardware to support and maintain the proper spacing between the fuel rods. The fuel bundle is surrounded by the channel box, a metal box directing the coolant flow through the bundle. The cruciform control rods enter from below in the region between the fuel assemblies and are guided by the channel boxes. The region between the fuel assemblies is called core bypass region and is flowed by coolant exchanging heat with the channel boxes.
In TRACE, BWR fuel assemblies are modeled with the CHAN component that contains all required input and internally generates a number of other TRACE sub-components such as 1D hydraulic components (PIPE), heat structures (HTSTR), and radiation heat transfer (RADENC) components.
PIPE sub-components are used to simulate:

- the flow through a BWR fuel assembly,
- the leakage path from BWR fuel assembly inlet nozzle to core bypass,
- the flow through any water rods.

HTSTR sub-components are used to simulate:

- the conduction and gap-gas heat transfer within the fuel rods,
- the convective heat transfer from the fuel rods to the fluid inside the fuel assembly,
- the heat transfer between the fluid inside the water rods, through the water rod walls and to the fluid inside the BWR fuel assembly,

- the heat transfer between the fuel assembly fluid, through the channel box walls and to the fluid in the core bypass.

The RADENC component is spawned to simulate the radiation heat-transfer enclosure within the BWR fuel assembly and includes the full length fuel rod group, the partial fuel rod group, the water rod group and the inside surface of the channel box wall.

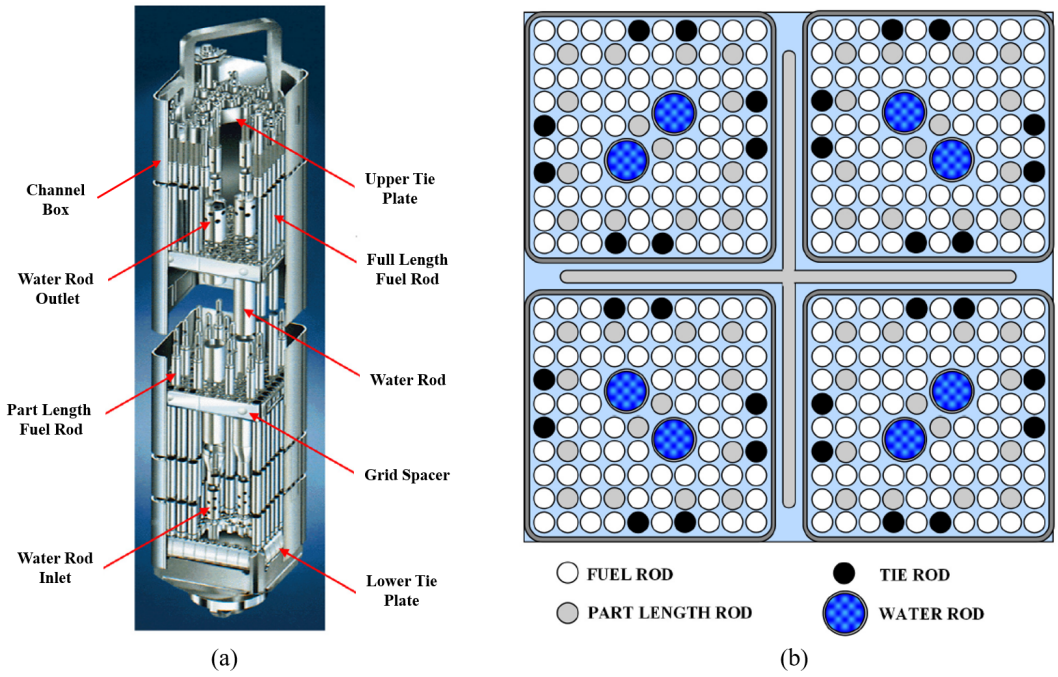

Figure 4.2: Fuel bundle configuration. (a) 10x10 fuel assembly, (b) 4-bundle fuel [3].

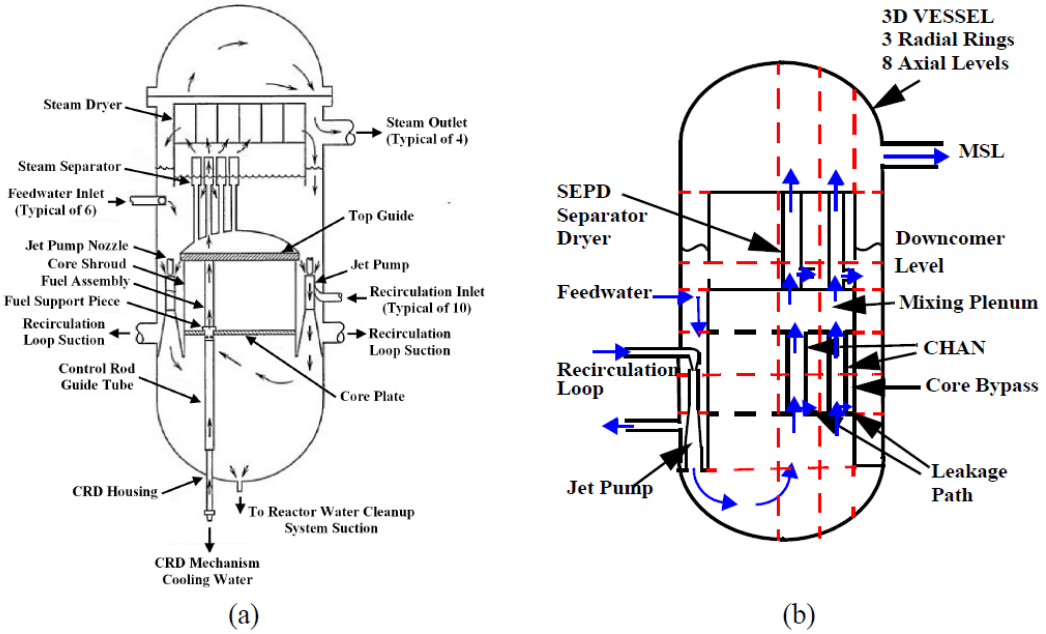

Figure 4.3: BWR reactor vessel; (a) cut-away diagram of a reactor vessel; (b) schematic representation of a TRACE reactor vessel with internals [3].

Interface between the components in a BWR model The CHAN components are modeled within the VESSEL component by defining junction connections between the CHAN's first and last cells with the VESSEL cells at the appropriate elevation. The outside surface of the CHAN's canister walls are in contact with fluid in the VESSEL's core bypass region. The occurring heat transfer is enabled by specifying in a CHAN's input array the VESSEL's axial levels in contact with the outside surface of the canister wall at each CHAN's axial level.

Figure 4.3 (b) shows a TRACE BWR reactor vessel schematic with the included internals. The black solid lines in the VESSEL represent the cell-face flow area fractions of zero (i.e no fluid flow between the cells) in order to model for example the downcomer. The dashed lines represent cell-edge flow-area fraction for modeling the top and bottom core support. The integration of other 1D components such as the SEPD or PIPEs (e.g. feedwater, steam line, recirculation loop) is also indicated in Figure 4.3.

Control System The TRACE control system is general, flexible and provides the same level of control over the computer model as a reactor operator has over the actual reactor system. It consists of four main building blocks: signal variables, control blocks, trips, and component-action tables.
Signal variables are modeled system parameters with real values by which information is communicated to the control system. Signal variables extract parameter information at any desired location in the computational mesh and process it to its own output. Such variables include global parameters (e.g. time), parameters of hydrodynamic component database (e.g. pressure), parameters of heat structure database (e.g. wall temperature), parameters of kinetics database (e.g. power) or parameters of the control system itself (e.g. trip output signals).
Control blocks are function operators which use as input signal variables as well as the output of other control blocks, process the input based on their function and return a single output. Examples of function operators are logic gates, functions of independent variables, integrators or adders.
A trip is an ON/OFF logical switch that compares user defined parameters against one or more set-points and returns their status. Essentially, trips are used for the control of the timing of mechanical action, for example, reactor scram, opening and closing valves or adjusting pump speed.
In addition, component-action tables are look-up tables from which the response of adjustable hardware action may be determined as a function of an independent variable. [3]

4.2 The Neutronics Code PARCS

Purdue Advanced Reactor Core Simulator (PARCS), is a computer code that solves the steady-state and time-dependent, multi-group, neutron diffusion and low-order transport equations in three-dimensional Cartesian geometry using nodal methods and is directly coupled to the thermal-hydraulics code TRACE, which provides the temperature and flow field information back to PARCS. The code version used in this work is PARCS 3.0 and its major calculation features include *eigenvalue* calculations, *transient (kinetics)* calculations, *Xenon transient* calculations, *decay heat* calculations, *pin power* calculations, *depletion* calculations, and *adjoint* calculations.

The PARCS *eigenvalue* calculation for steady-state reactor analysis is employed as it provides the initial steady-state for the following transient calculation. During the transient calculation, PARCS solves the time-dependent neutron diffusion and low-order transport equations involving both delayed and prompt neutrons.

The geometric representation of the BWR core in PARCS is done by a group of homogeneous computational nodes.

PARCS uses macroscopic nodal cross sections (Σ) which are functions of boron concentration (B, in ppm), the square root of the effective doppler fuel temperature (T_f), moderator temperature (T_m), moderator density (D_m), void fraction (α), and the effective rodded fractions (ξ). For these state variables, only a linear dependence of the feedback is considered with the exceptions of the moderator density and void fraction, for which a quadratic dependency is additionally provided. This functionalization is adequate for Light Water Reactors and can symbolically be described as:

$$\begin{aligned}\Sigma(B, T_f, T_m, D_m, \alpha, \xi) = \Sigma_0 + a_1(B - B_0) + a_2(\sqrt{T_f} - \sqrt{T_{f0}}) \\ + a_3(T_m - T_{m0}) + a_4(D_m - D_{m0}) + a_5(D_m - D_{m0})^2 \\ + a_6\alpha + a_7\alpha^2 + \xi\Delta\Sigma_{CR}\end{aligned} \tag{4.7}$$

PARCS is directly coupled to TRACE and is activated by setting specific variables in TRACE and PARCS input. TRACE delivers to PARCS the temperature/fluid

conditions, including the coolant density, coolant temperature and the effective fuel temperature. PARCS determines the nodal power information that is transferred back to TRACE. Generally, the neutronic node structure differs from the T-H node structure. The interface file MAPTAB governs together with automatic schemes, the mapping between the TH-nodes and the neutronic nodes. These schemes are able to manage the mapping configuration of multiple BWR CHAN components to a 3D neutronic core. The user is required to input a radial map that assigns the TRACE employed CHAN(s) to each neutronic node used in PARCS. The axial mapping is accomplished without user intervention as a linear interpolation scheme used in order to manage the difference in neutronic and TH-nodalization during the course of data transfer. As previously mentioned, neutronic node sizes may differ from TH-node sizes and in general coarser node sizes are used in T-H calculation than in neutronics calculation.
By the input of a history file, PARCS applies history and T-H state information that according to the burn-up of the core being modeled, namely control rod history, coolant density history, coolant temperature history and xenon and samarium densities. [13]

4.3 Methods applied for the Improvement of the Coupled Simulations

4.3.1 Strategy to minimize Numerical Diffusion in TRACE

As previously mentioned, TRACE offers two numerical solution procedures, namely the Stability Enhanced Two Step (SETS) method and the semi-implicit (SI) numerical method.
Xu et al [14] claim that the SI method in TRACE has to be applied for stability analysis, based on studies by Mahaffy [15], [16] that describe the potential for numerical damping in the SETS method. Applying the SI method for stability

analysis requires the Courant-Friedrich-Lewy number CFL near unity for the purpose of minimizing numerical dissipation. The CFL as used by TRACE takes the form presented in Equation (4.8), where v is the fluid velocity, Δx is the mesh size, and Δt is the time step size.

$$CFL : c = \frac{v\Delta t}{\Delta x} \tag{4.8}$$

The fluid velocities increase in the core channels from the bottom to the top, with the supply of power to the fluid increasing its volume and its vapor content. In order to satisfy the CFL limit, an adjustable axial mesh size, proportional to the maximum vapor velocity, was introduced with smaller axial cells at the bottom and larger cells towards the top of the fuel channels.

4.3.2 Adaptation of PARCS Nodalization to TRACE

The previous subsection 4.3.1 presents the demand for an adjustable axial mesh size for the TRACE fuel channel nodalization.
The current simulation model consists of the thermal-hydraulic part TRACE coupled with the neutron kinetic part PARCS. In the coupled simulation, several thermal-hydraulic and neutron kinetic variables are exchanged between the two codes. TRACE is transferring density and temperature values of the fluid together with temperature of the fuel to PARCS, which is returning the power data back to TRACE.
Generally, the PARCS axial node structure may differ from the TRACE axial node structure, since the mapping of the TRACE nodes and the PARCS nodes is managed by the MAPTAB interface file that stores the weighting factors for the geometrical congruence of two cells. The congruence value is one if the cells used in both codes describe the same volume. But in case the mapped volumes are shifted, then a fractional congruence value, according to the coverage, is introduced.

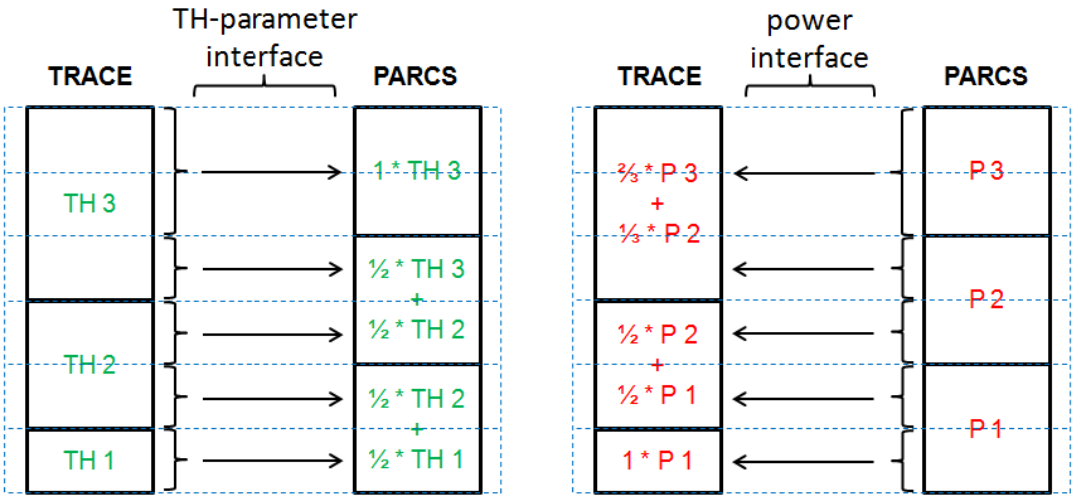

Figure 4.4: Transfer of data between TRACE (adapted cell size) and PARCS (uniform cell size). Left: First transfer of TH-data from TRACE to PARCS ; Right: Second transfer of power data from PARCS to TRACE [4].

Figure 4.4 represents schematically the spatial coupling between TRACE with CFL-optimized nodalization and PARCS with uniform axial node lengths. The thermal-hydraulic parameters are stored in the blocks TH 1 to TH 3 for cell 1 to 3. The interface averages the received values according to the spatial component weighting and transfers them from TRACE to PARCS as shown in Figure 4.4 on the left hand side. PARCS uses the thermal-hydraulic data to compute the power output parameters that are afterward transferred back to TRACE. Figure 4.4 shows on the right hand side the same model as on the left hand side, but this time the power parameters P1 to P3, representing the calculated power in cell 1 to 3, are transferred from PARCS to TRACE. Analogous the interface uses the weighting factors from the MAPTAB file to calculate the averaged parameters for the TRACE cells.

By using different axial cell sizes in TRACE and PARCS and the associated averaging of transferred parameters, inaccuracies are incorporated in the simulation results. This can be avoided by adapting the PARCS axial node sizes, as closely as possible, to the TRACE node sizes. This step was performed within a study research under the direction of this work [17], [4].

4.3.3 The Concept of Space-time convergence

A TRACE/PARCS model is considered as space-time converged when further increase in the number of nodes and further decrease in time step size has an insignificant effect on the simulation solution. A full space and time convergence study for all components in a BWR TRACE model was performed in [18]. This procedure was employed on a TRACE/PARCS model for the "Analysis of the OECD/NEA Oskarshamn-2 BWR stability benchmark" [6].

	Initial Model	Final Model
Nodes in vessel	15	45
Nodes per core channel	28	112
Time step size (s)	0.008 - 0.045 (varies)	0.004 (constant)

Table 4.1: Differences in discretization between the Initial and Final Model [6].

Table 4.1 compares the discretization differences of the "Initial Model" and the "Final Model". As a main simulation result it is stated that in the "Final Model" the oscillations were significantly less damped than in the case of the "Initial Model". However, the calculation time of the "Final Model" is approximately 17 times larger than that of the "Initial Model". Therefore, [6] describes the required trade-off between computational cost and accuracy of the solution.
Since [6] uses a half-core symmetry with 222 core channels and in this work a full-core model with 444 channels is employed, the trade-off in favor of computational capacity is chosen.

4.3.4 Sensitivity and Uncertainty in the TRACE/PARCS BWR-stability prediction

Uncertainties in coupled code calculation arise from different sources such as inaccuracies in the basic data as well as inaccuracies of the simulation tools. The influence of input parameters and the identification of the most influential ones on simulation results for the prediction of BWR stability with the time domain

coupled codes TRACE/PARCS was investigated in [19] and [20] and is briefly summarized here.

Both, neutronics and thermal-hydraulics uncertain parameters were identified and for each parameter sensitivity calculations were performed in order to account for their separable effect and to quantify their importance on stability. The most dominating parameters are: axial power profile, bubbly-slug wall drag coefficient, fuel thermal conductivity and RPV inlet water subcooling.

In the context of this work, it was intended to develop a full-core model that can reproduce the Oskarshamn-2 1999 feedwater transient in order to produce simulation data for the further application of the post-processing methodology. As described in the foregoing section 4.3.3, a trade-off at the expense of accuracy was necessary. Since the simulation results showed to be sensitive to changes in the some important system parameters, especially during the evolution of the power oscillation after the partial scram, minor parameter variations within the in Ref.[19] described uncertainty ranges were used to "tune" the original model in order to reproduce the measurement data of the transient as close as possible.

Chapter 5

Modelling and Simulation with TRACE / PARCS

5.1 Modelling Description

5.1.1 TRACE Nodalization and Input Parameters

The TRACE model is prepared based on the official benchmark specification [2]. It consists of a feedwater line with the mass flow boundary condition, vessel, recirculation loop, 444 core channels, separator and steam line with a pressure boundary condition. Various controller system components are used for obtaining balance-of-plant during steady-state calculation as well as for controlling the boundary conditions during transient calculation. Figure 5.1 shows the TRACE nodalization scheme employed. The feedwater boundary condition is modeled with a *FILL* that introduces sub-cooled water into the *VESSEL* component. Mass flow and liquid temperature values follow the control system. The *FILL* is connected to the feedwater line, a *PIPE* component with six cells that is connected to the *VESSEL* component.

The reactor pressure vessel is modeled with the *VESSEL* component. It contains 45 axial levels with different cell heights in order to match section planes

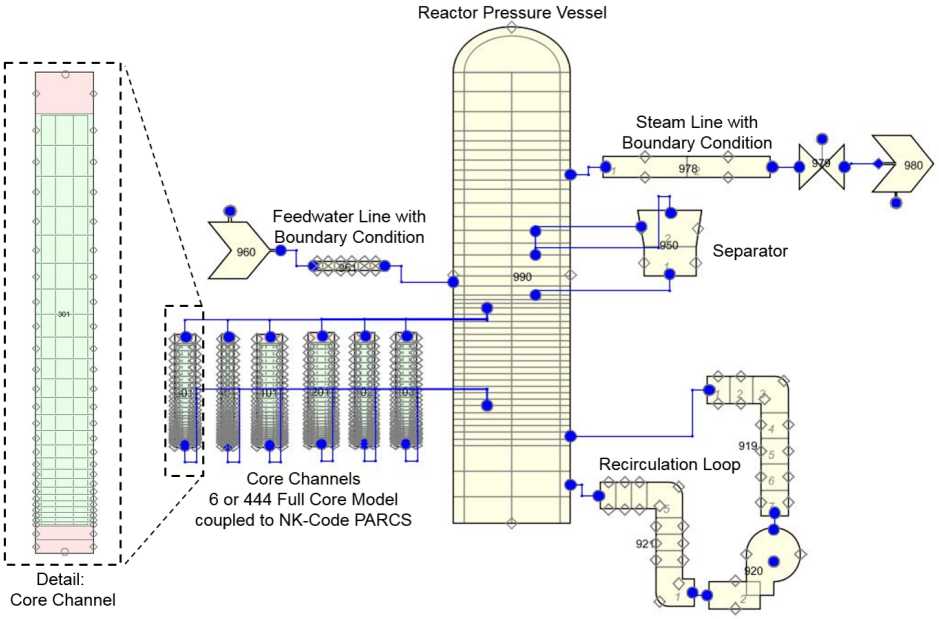

Figure 5.1: Oskarshamn-2 TRACE nodalization scheme.

with the reactor internals. Radially the *VESSEL* is composed of two rings. The outer ring represents the downcomer and the inner ring contains all components inside the core shroud.

The four external recirculation loops are summed up and modeled as one recirculation loop. The suction side of recirculation line is represented as a *PIPE* with seven cells and is connected to the *PUMP* component. The *PUMP* impeller rotation speed is adjusted by a control system to provide the desired recirculation mass flow in steady-state or transient calculation. The outlet of the *PUMP* is connected to the pressure side of the recirculation loop, a *PIPE* with eight cells, closing the loop with a connection to the *VESSEL*.

The core is a full core model with 444 core channels made of *CHAN* components. The core is loaded with four different fuel types. Furthermore, the core is divided into three orifice zones with differing inlet orifice loss coefficients: central, semi-peripheral and peripheral. Since in the semi-peripheral and peripheral orifice

zones only Type 1 fuel is located, six different *CHAN* models are needed.
According to the specifications the following fuel characteristics are considered for each *CHAN* model: geometry of channel box and fuel rods, water rods, partial length fuel rods as well as friction loss coefficients for the inlet orifice, lower tie plate, spacers, and upper tie plate.
Additionally to the detailed view of one example channel in Figure 5.1 it has to be mentioned that all 444 channels are equally modelled in the axial direction from a nodalization point of view. These are divided in 28 nodes, with two nodes for the lower inactive part, 25 nodes for the active part and one node for the upper inactive part. In order to minimize numerical diffusion, as described in section 4.3.1, the node sizes for the active part are proportional to the maximum vapor velocity, which results in smaller axial cells at the bottom of the channel and larger cells towards to top of the active part of the channels.

The Separator is modeled with the *SEPD* component with the option of an ideal separator with constant carry-over and constant carry-under values, two axial cells, and it contains 90 standpipes. The *SEPD* inlet is connected to the *VESSEL* between the mixing plenum, where the steam-water mixture enters the separator, and the steam dome, where the steam leaves the separator. The separated liquid phase is returned by a connection from the separator side arm to the VESSEL to join the downcomer annulus flow.

The steam leaves through the steam dome of the *VESSEL* that is connected to the steam line; a modeled *PIPE* component with two cells that represents the four main steam line loops. The steam line *PIPE* element is connected to a *VALVE* component, that was initially implemented as a Turbine Control Valve but is not applied in the context of this work. The *VALVE* is finally connected to the pressure boundary condition component *BREAK* that imposes the system pressure according to the steady-state or transient demands by a control system.

5.1.2 PARCS Nodalization and Input Parameters

For neutronics calculation PARCS is coupled with TRACE. The PARCS model is developed according to the core composition map presented in Figure 5.2. It shows ten assembly types that have axially different NK information and are marked with different colors: SO, SP, SQ, SR, SS, QA, QC, QB, QD, QE. Assembly type RE represents the reflector. Furthermore, the radial, one-to-one mapping of PARCS neutronic nodes to the TRACE thermal-hydraulics (numbering) nodes is shown in the same figure.

In addition, the PARCS model includes the control rod information of the 109 control rods, arranged in 17 scram groups, with respect to the radial position and the amount of rod withdrawal.

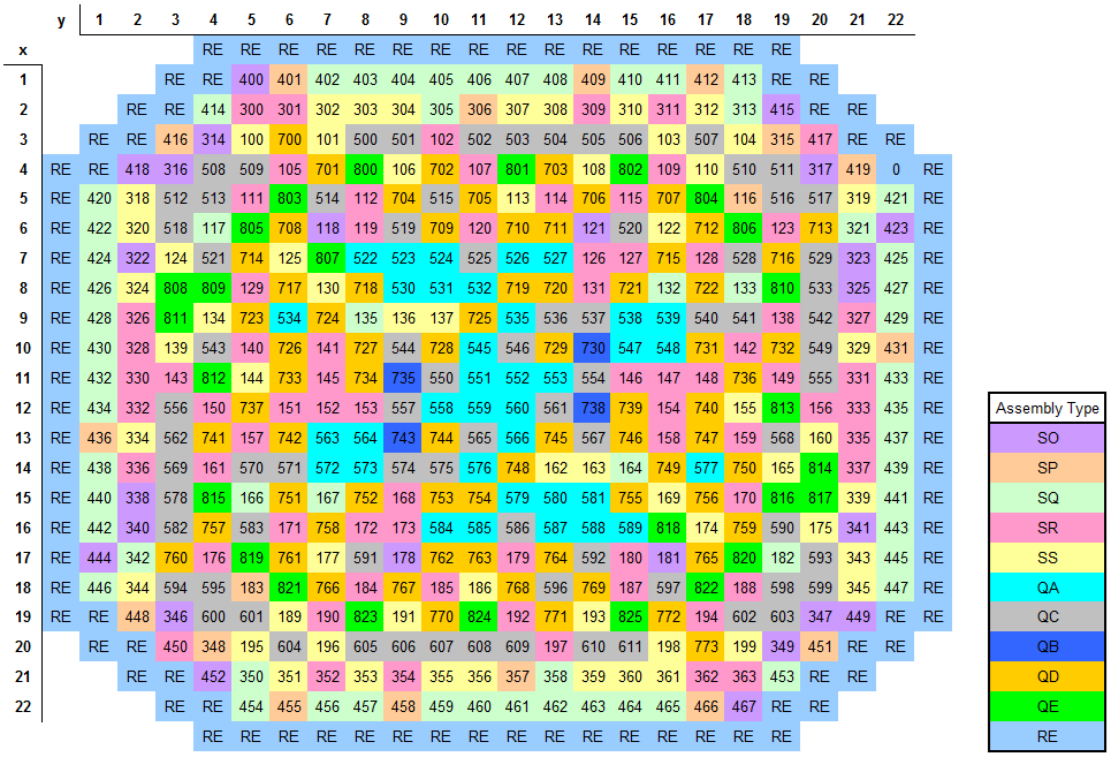

Figure 5.2: Oskarshamn-2 core composition map: assembly type SO, SP, SQ, SR, SS, QA, QC, QB, QD, QD, QE comprise unique axial NK information assigned to the TH (numbered) channels. Assembly type RE represents the reflector.

Oskarshamn-2 Benchmark [2] provides the neutron-kinetic data in PMAXS format. These cross-section libraries, burn-up and history distributions are in a format that represents the core axially in 25 nodes of uniform height.
According to section 4.3.2 these data are adapted in order to match axially with the TRACE CFL-optimized nodalization. On this account, 27 NK axial regions for the active part of the core are needed and the assignment can be seen in Figure 5.3.

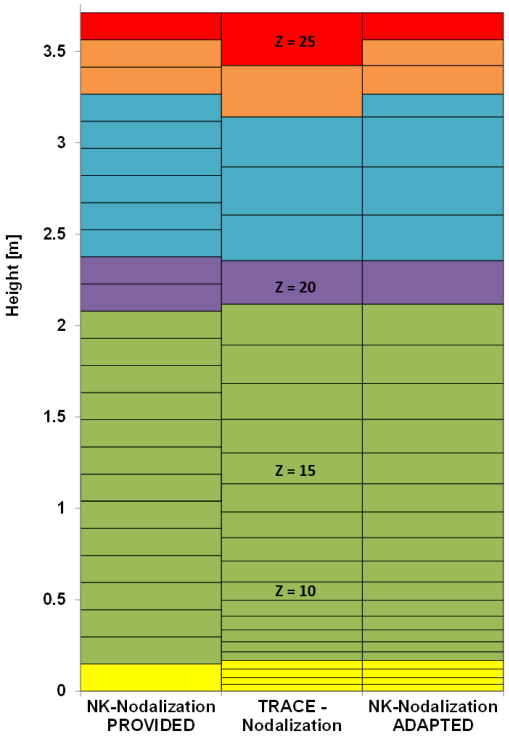

Figure 5.3: NK to TH assignment: provided uniform NK-nodalization (left), TRACE axial nodalization (middle), NK-nodalization adapted and applied in simulation (right).

A coordinate system for the representation of the reactor core is defined: in the radial representation the x-coordinate is defined in direction from top left to bottom left (x: $\downarrow$) beginning from core channels (the reflector is not included); the y-coordinate is defined from top left to top right (y: $\rightarrow$) according to Figure 5.2. The z-coordinate is defined in the flow-direction from core bottom to core top according to Figure 5.3 "TRACE-Nodalization".

5.2 Steady State Solution of the Simulation

In the present TRACE/PARCS model initial and boundary conditions are considered according to the benchmark specifications [2] and the steady-state calculation is performed for the starting-point of the O2-1999 feedwater transient.
Table 5.1 presents a comparison of the TRACE/PARCS simulation steady-state results against plant measurement data, as well as, data provided by the benchmark organizers computational model (Code 2).
Minor differences are already recognizable between the measured and the Code 2 calculated data, but are within a reasonable range regarding the discussion in section 4.3.3 and section 4.3.4 on accuracy versus computational time, as well as, the sensitivity of computational models. The applied TRACE/PARCS model performs in the same range as Code 2 and it can be concluded that the results are in good agreement with the measured data.

	Measured	Code 2 *	TRACE/PARCS
Reactor Power (MW)	1798.6	1802.00	1801.97
Steam Dome Pressure (MPa)	6.93	7.0000	6.9629
Core Inlet Pressure (MPa)		7.1162	7.1455
Core Outlet Pressure (MPa)		7.0141	7.0296
Core Pressure Drop (kPa)		102.00	115.90
Feedwater Temperature (K)	457.65	456.62	457.60
Core Inlet Temperature (K)	547.30	543.57	543.61
Inlet Subcooling (K)		16.59	16.80
Steam Temperature (K)		558.48	558.61
Total Core Flow Rate (kg/s)		5515.90	5515.89
Active Core Flow Rate (kg/s)		4800.40	4740.36
Steam Flow Rate (kg/s)		903.10	903.99
k-eff		1.0092	0.9952

*These results originate from the benchmark organizers' computational model

Table 5.1: Steady-state conditions at the beginning of the O2-1999 FW-Transient.

5.3 Transient Simulation of the O2-1999 Feedwater Transient

The steady-state solution discussed in section 5.2 and summarized in Table 5.1 is used as the initial starting-point for the O2-1999 feedwater transient calculation with the coupled TRACE/PARCS model. According to the benchmark specifications [2] the following boundary conditions are used:

1. Feed Water Temperature (corrected)
2. Feed Water Flow Rate
3. Recirculation Pump Speed
4. System Pressure (referenced at steam dome)
5. Partial Scram @ time=197.6sec

Items 1) to 4) are boundary conditions implemented in the TRACE model by control systems using time dependent tables. Item 5) is implemented in the PARCS model where control rod banks are moved according to the value/time pairs. Figure 5.4 indicates the control rod bank positions before and after the partial scram.

Figure 5.5 shows the TRACE/PARCS simulation results (blue) versus the measured data (red). The boundary condition 'Feed Water Temperature' differs from the measured value, due to a correction applied. The official benchmark specifications [2] also present the requirement for the feedwater temperature correction. The other boundary conditions are equal with the measured values. The TRACE/PARCS calculated power is the simulation output value of the greatest interest and shows a very good reproduction of the transient. A detail view in Figure 5.6 shows that the power evolution after the partial scram, in the time frame 203 s to 209 s, is somewhat higher, followed by a development with slightly lower power in the time interval from 216 s to 230 s.

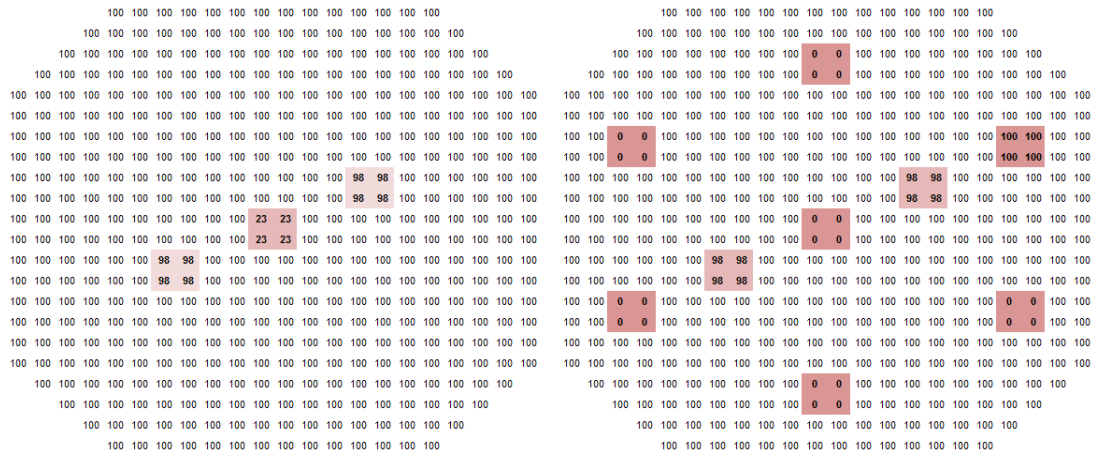

Figure 5.4: Control rod positions before partial scram (left) and after partial scram (right). A value of 100 indicates fully withdrawal of the control rod banks while 0 indicates fully insertion of the control rod banks.

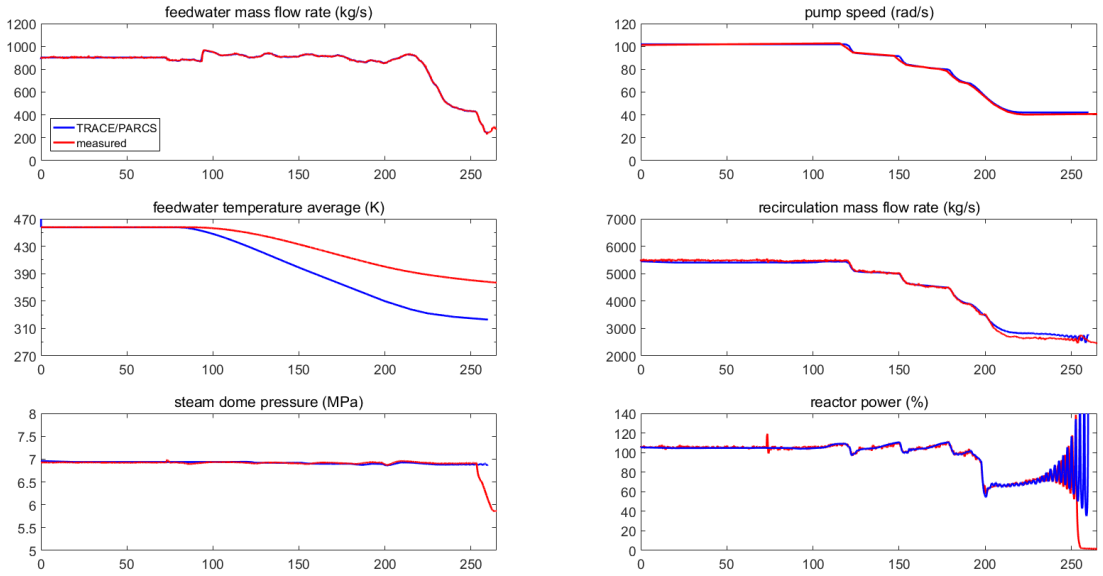

Figure 5.5: O2-1999 FW-Transient, measurement vs. TRACE/PARCS simulation.

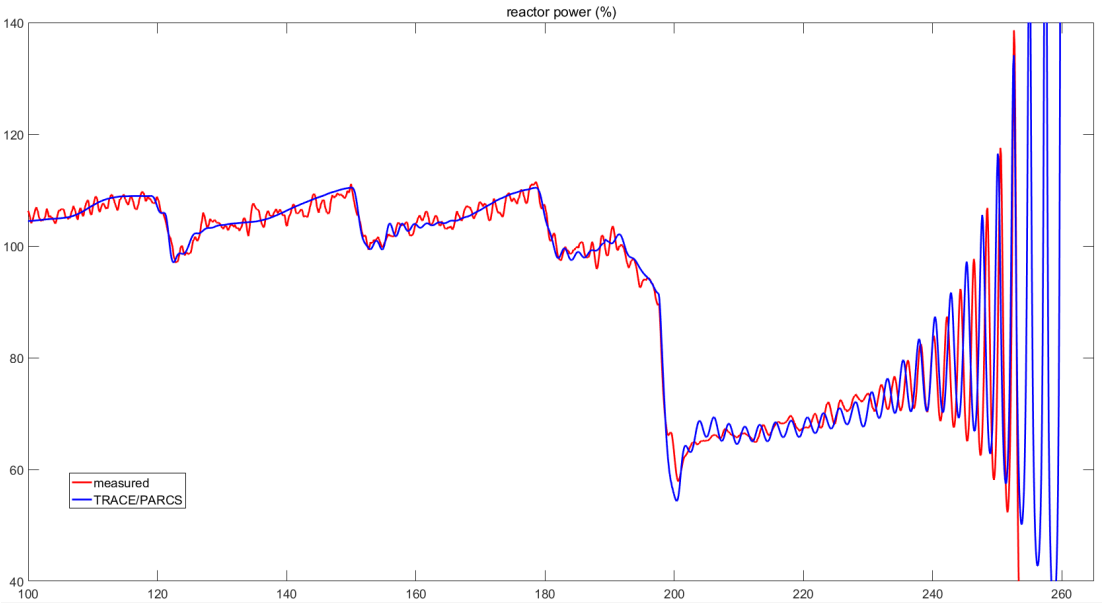

Figure 5.6: O2-1999 FW-Transient: reactor power, detail.

Overall, the oscillation frequency is lower, which can be explained based on the use of a rod gas-gap heat transfer coefficient with a predefined constant value of 6000 $\frac{W}{m^2K}$ according to [2]. Even though [18] acknowledges that the gap conductance is a parameter with a very large uncertainty and high impact on the power's oscillation frequency. The goal of the "fine tuning" of this parameter in order to match the oscillation frequency is not within the scope of this work.
In summary, the coupled TRACE/PARCS simulation captures the Oskarshamn-2 1999 feedwater transient very well and can be regarded as validated and suitable for the further investigations discussed in the next chapters.

Chapter 6

Analysis of BWR Instability Phenomena using Spectral / Frequency Decomposition

In this chapter a spectral analysis method for BWR instability events data is presented. The investigated signals are physical parameters of the reactor core in local scale and the applied mathematical method is the Fourier Transform.

6.1 The Fast Fourier Transform

The process of spectral analysis identifies frequencies and associated amplitudes in data. A periodic function can be represented as a sum of infinite numbers of (co-)sinusoidal components at equally spaced frequencies with a interval of 1/T, the so called Fourier Series, where T is the period of the function. The Fourier Transform is applied to decompose time series signals into frequency components, with each frequency component consisting of an amplitude and phase. The inverse Fourier transformation reconstructs the information from the frequency-domain representation back into the time series signal.
The Discrete Fourier Transform (DFT) is an algorithm to transform a discrete time domain signal into a discrete frequency domain representation and is defined

as:

$$X[k] = \sum_{n=0}^{N-1} x[n] e^{-j2\pi k \frac{n}{N}} \tag{6.1}$$

with

X : the frequency domain representation of the signal time-series signal x. The formula yields one complex number $X[k]$ for every k.

k : the k-th frequency component; $k = 0, 1, ..., N-1$

N : the total number of samples in signal x

x : the time series signal; $n = 0, 1, ...N-1$

n : the n'th sample (in the time domain)

j : the imaginary unit

The k-th basis function is defined as

$$e_k[n] = e^{-j2\pi k \frac{n}{N}} \tag{6.2}$$

The phase angle of the complex number is described as

$$\varphi[n] = \frac{k \cdot n}{N} 2\pi \tag{6.3}$$

The formula for transforming a signal in the frequency-domain back into the time domain, the inverse transform, is calculated as a summation over all the frequency components k:

$$x[n] = \frac{1}{N} \sum_{k=0}^{N-1} X[k] e^{j2\pi k \frac{n}{N}}. \tag{6.4}$$

The Fast Fourier Transform (FFT) is a version of the DFT that uses special algorithms to make the FFT much faster than the DFT and is available as an implemented function in MATLAB. The functions `Y = fft(x)` and `y = ifft(X)` implement a given transform and inverse transform pair for vectors of length N, [21], [22]. These functions are applied in MATLAB within the scope of this work.

6.2 The Application of the FFT on the global Parameter Reactor Power

The data used in the following is the measurement signal of the total reactor power from the Oskarshamn-2 1999 feedwater transient for the time interval from 233.2 s to 249.6 s, as shown in Figure 6.1. Applying the FFT to this signal, the spectral analysis is returned and presented in Figure 6.2.

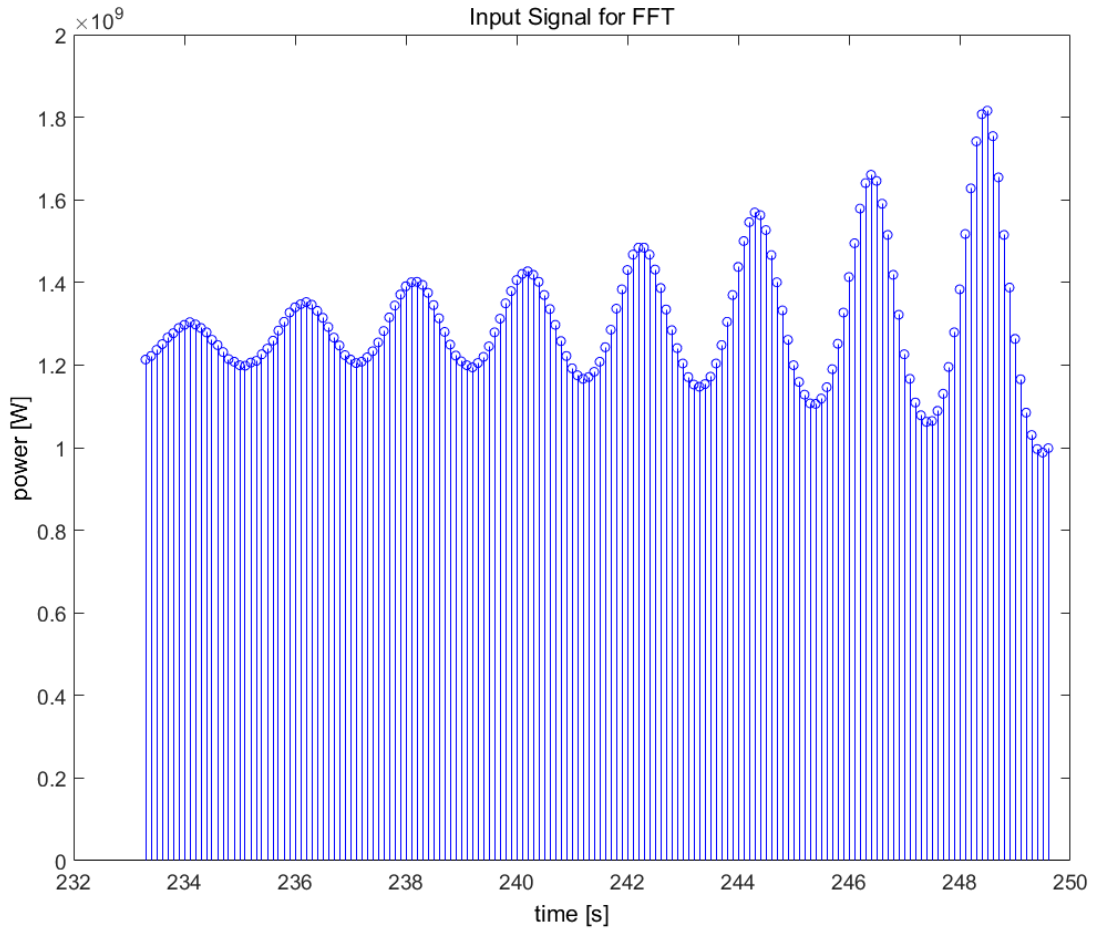

Figure 6.1: O2-1999 FW-Transient: total reactor power.

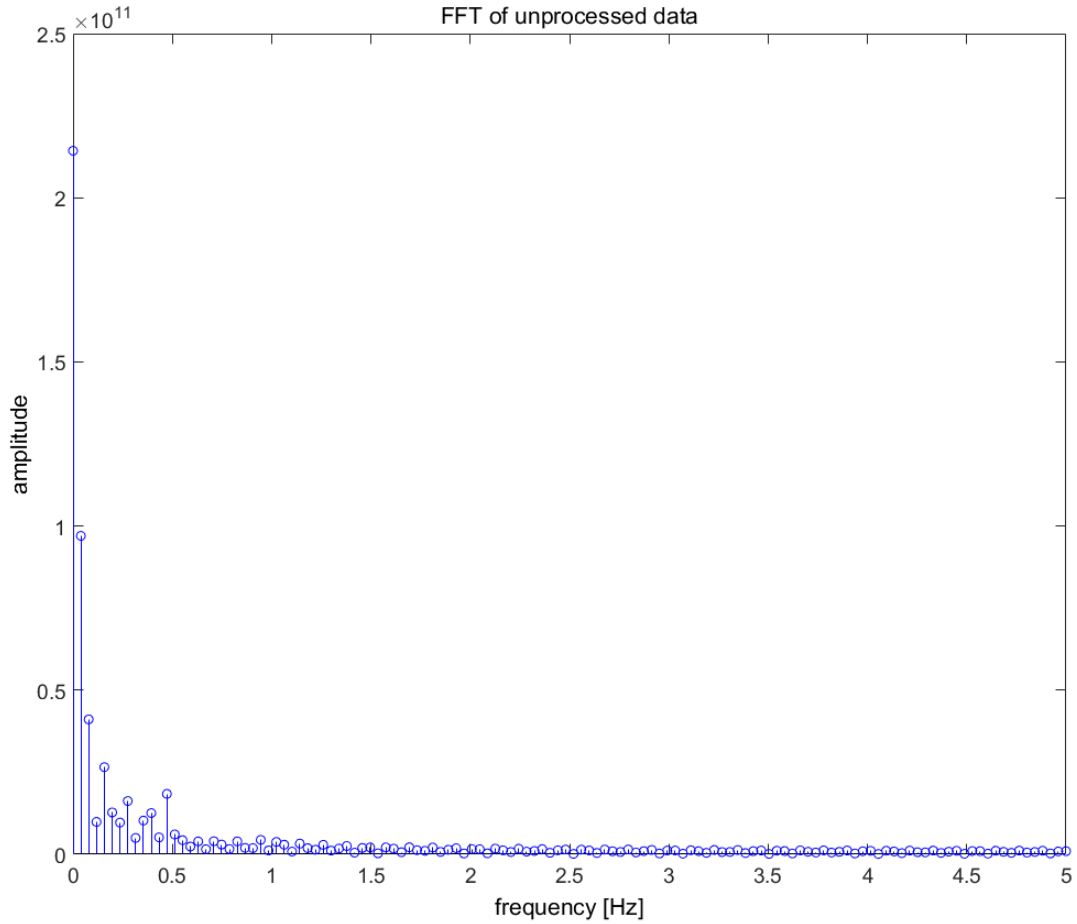

Figure 6.2: Spectral analysis of the power signal.

The signal is characterized by a high amplitude with a frequency of $f = 0\,\mathrm{Hz}$ resulting from to the offset, that is, the mean value, of the input signal.
Generally the parameters in this analysis are physical quantities, which can increase or decrease in their mean values as a response to the transient undergone by the system. The change of the mean value is not of interest in this analysis, but solely the oscillating component of the signal is of peculiar interest in the FFT output. Therefore, the offset and the slope are eliminated from the signal. This is carried out by subtracting a linear function that is fitted to the input signal as presented in Figure 6.3.

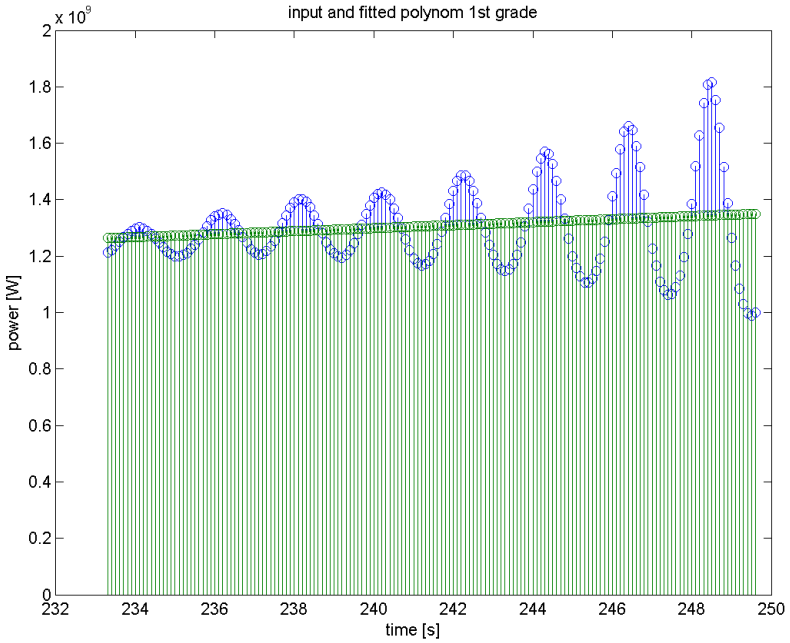

Figure 6.3: Power signal and fitted linear function.

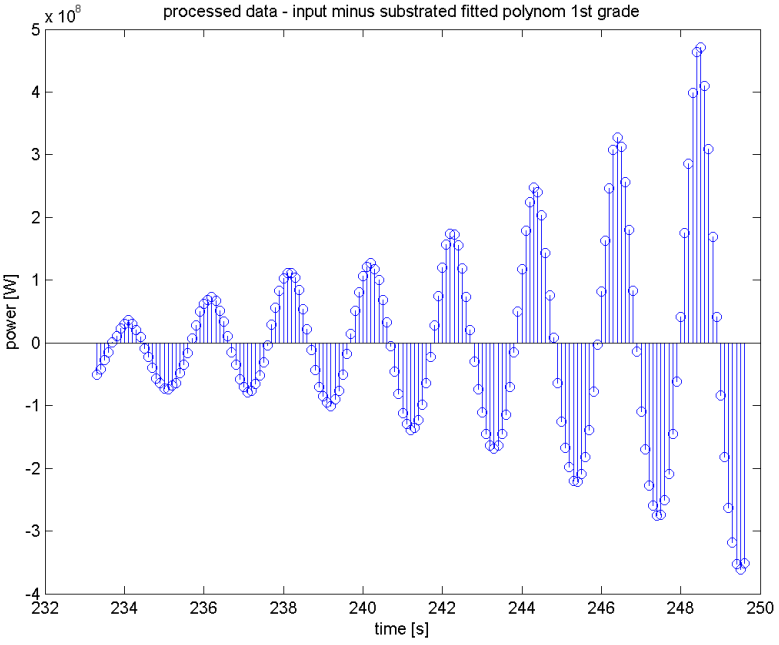

Figure 6.4: Oscillation of the power signal.

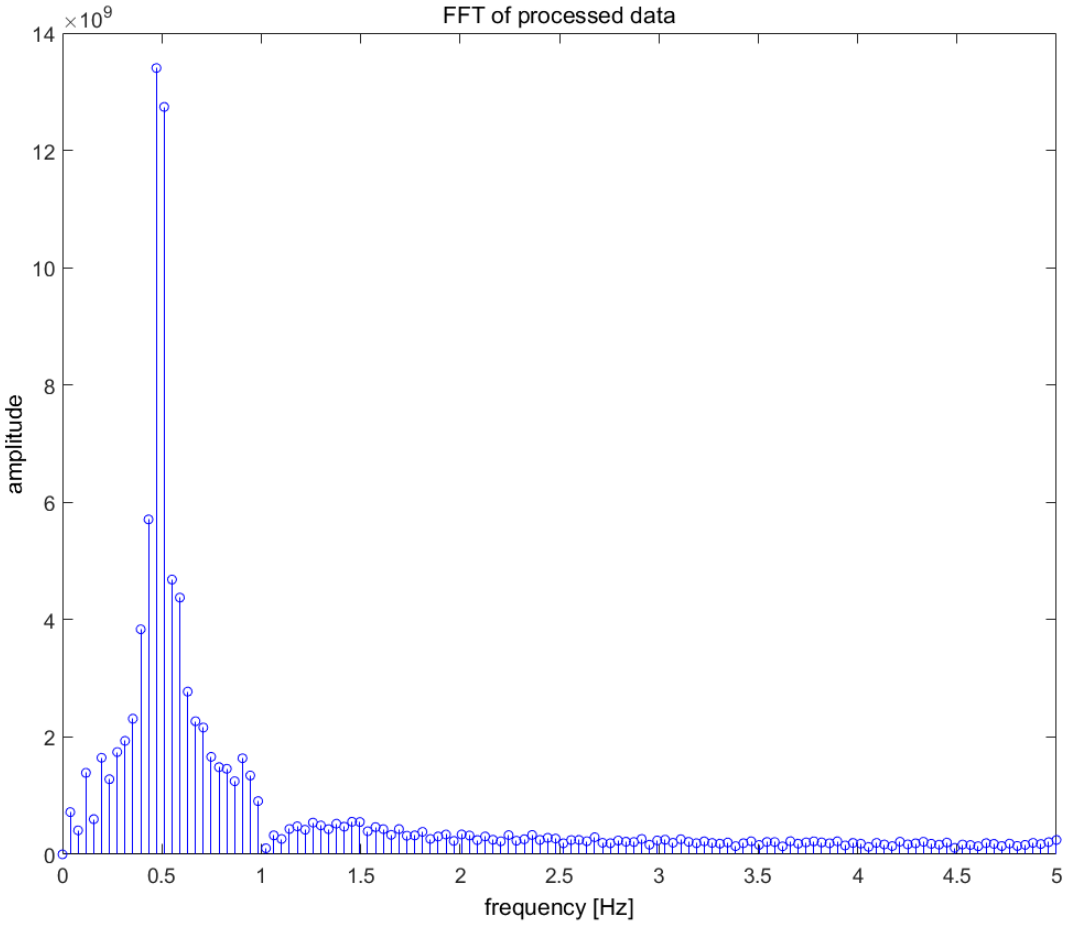

Figure 6.5: Spectral analysis of the oscillation signal.

The processed input signal without its offset and slope, which describes solely the oscillating part of the signal, is shown in Figure 6.4 and again the FFT is applied to this signal and its spectral components are shown in Figure 6.5. Significant amplitude peaks are obvious at a frequency of about $f = 0,5\,\text{Hz}$.
This is in accordance with the definition of the frequency where the number of cycles and the time interval are read from Figure 6.4:

$$f = \frac{\text{number of cycles}}{\text{time interval}} = \frac{8\,\text{oscillations}}{16,4\,\text{seconds}} = 0,488\,\text{Hz}$$

6.3 The Application of the FFT to local physical Parameters

The FFT is applied to computed local variables of the TRACE/PARCS simulation results of the Oskarshamn-2 1999 feedwater transient. For example, in the case of the total mass flow of two adjacent core channels at position $x = 15, y = 11, z = 6$ and $x = 15, y = 12, z = 6$, in the time interval between 235 s and 240 s as shown in Figure 6.6, the results of the FFT analysis are presented in Figure 6.7. The signal on the left hand side ($x = 15, y = 11, z = 6$) has an average value of about 4.3 kg/s but considerably higher oscillation amplitudes compared to the signal on the right hand side ($x = 15, y = 12, z = 6$), with an average value of about 5.4 kg/s.

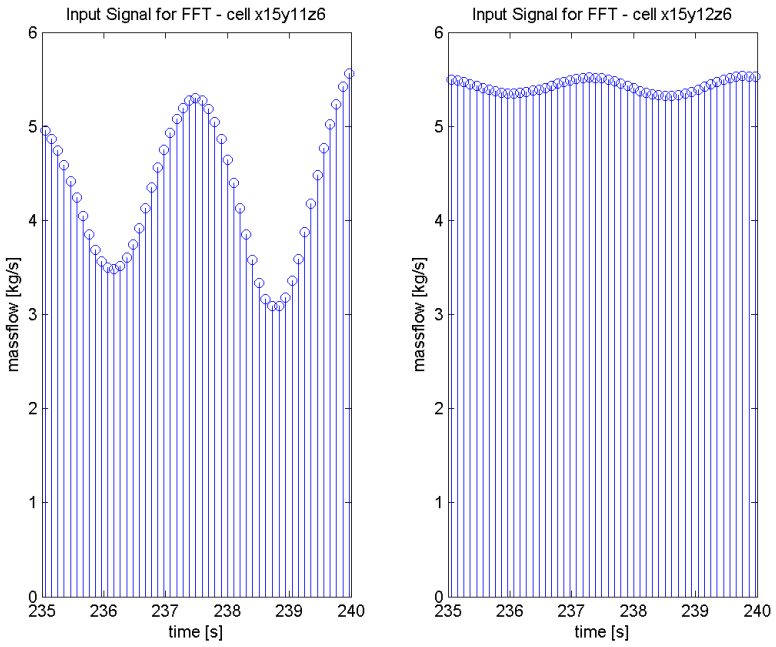

Figure 6.6: Input signals of two adjacent cells.

As in the previous section 6.2, the FFT is applied separately to the unprocessed input signals and the results of the spectral analysis are shown in Figure 6.7. The amplitude at the frequency $f = 0$ Hz is the one governing the result. The

higher average input signal in the case of the channel on the right hand side ($x = 15, y = 12, z = 6$) results in a higher amplitude of the spectral output at $f = 0\,\mathrm{Hz}$.

As the focus of the work is solely on the oscillation component of the signals, the offset and linear functions that are individually fitted to the slope, as shown in Figure 6.8, are subtracted from the input signals and the processed input signals are presented in Figure 6.9.

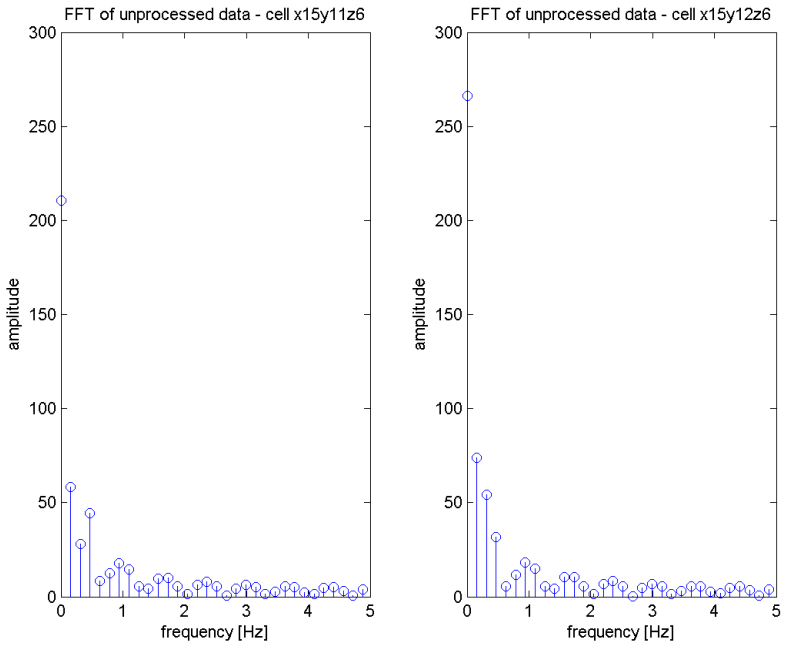

Figure 6.7: Spectral analysis of the unprocessed signals of the adjacent cells.

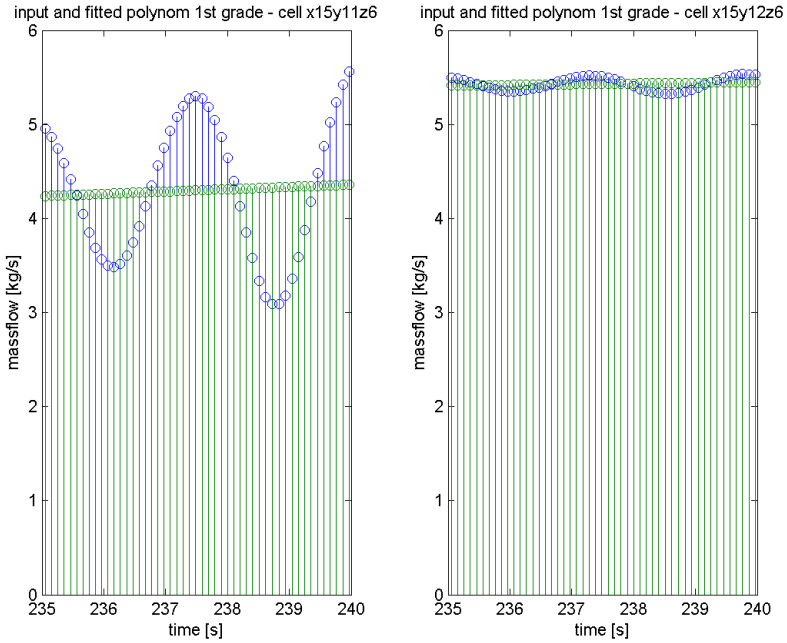

Figure 6.8: Input signals and individually fitted linear functions.

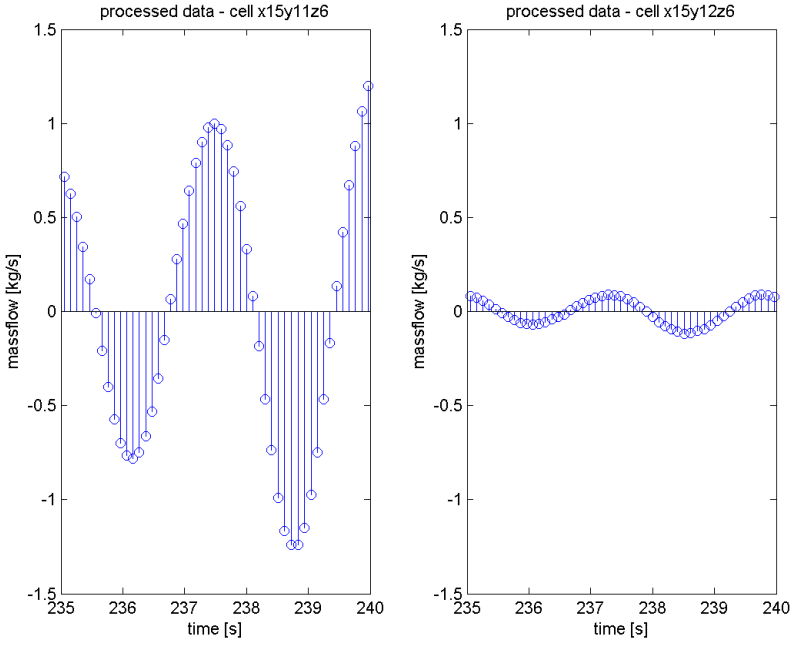

Figure 6.9: Oscillation signals of the adjacent cells.

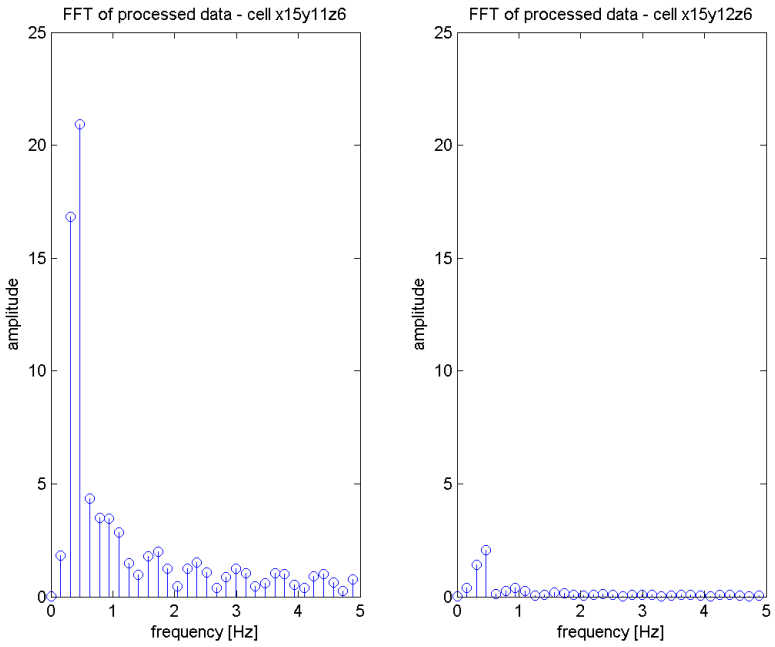

Figure 6.10: Spectral analysis of the oscillation signal of two adjacent cells.

Figure 6.10 shows the result of the spectral analysis of the input signals reduced to their oscillation components. Both outputs show the amplitude peak at the characteristic frequency at about 0.5 Hz. However the amplitudes differ significantly. The amplitude heights represent relatively the *amount* of the specific frequency contained in the spectrum. This means in this case that the input signal of the left cell $(x = 15, y = 11, z = 6)$ has a much higher *amount* of the characteristic frequency. It is obvious that this channel is more strongly oscillating with respect to the amplitude than the channel on the right hand side $(x = 15, y = 12, z = 6)$. Expanding this method from two adjacent cells to a complete axial level of the core, a relative evaluation of the oscillating contribution of each channel can be performed. This is shown in Figure 6.11, where one radial plane of the complete core channels is selected. Similarly, Figure 6.12 shows the results for one axial section.

The steps performed with the described procedure are summarized next:

- A relevant time interval is selected and the unprocessed signal variables are read. The time interval (or time frame) length is freely selectable, but has to be adjusted to the system frequency and to the physical characteristics of the signal. Appendix A.1 gives a study with different time interval lengths and a recommendation for the best fitting time frame length.

- For every single signal the offset and the slope are subtracted individually. This is necessary to obtain solely the oscillating component of the signal and to get rid of components in the signal which stem from transient-dependent system responses, such as the increase or the decrease of the mean value of the signal. This method implies a normalization of the signals and makes the spectral results comparable to each other.

- The output of the FFT is the spectral analysis of the signals in the amplitude versus frequency form. The height of the amplitude in the frequency domain is equal to the height of the amplitude in the time domain for each specific component.

- As the input signals are normalized in this method, it follows for the interpretation of the spectral output results that a nodal cell with a high amplitude has a high oscillation component of the signal compared to a cell with a low amplitude and a low oscillation component in the signal.

- If the output of the spectral analysis shows a significant peak of a certain frequency, it follows than this particular frequency is dominating the signal. Otherwise, in a qualitative meaning, a broad spectrum with no significant peaks means that there is no dominating frequency.

The above described procedure is used in this work for the study of oscillating signals at any local position in the core and for any kind of signal, such as power, mass flow, density or void fraction. The analysis can be carried out in any radial direction (Figure 6.11) or axial direction (Figure 6.12).

For the radial representation of the FFT results, an amplitude scaling factor is given at the top left of the plots (e.g. in Figure 6.11 **Amplitude: 0 - 4**) and it indicates by which value all amplitudes are scaled in order to fit in the plot. With the help of this scaling factor it is possible to compare the amplitude heights of different FFT results in radial representation.

A general remark on the axial representation of FFT results: the nodalization in TRACE has non-uniform node heights according to Figure 5.3. However, for a better visualization of the FFT results in axial direction a uniform box height is shown for all figures in this work.

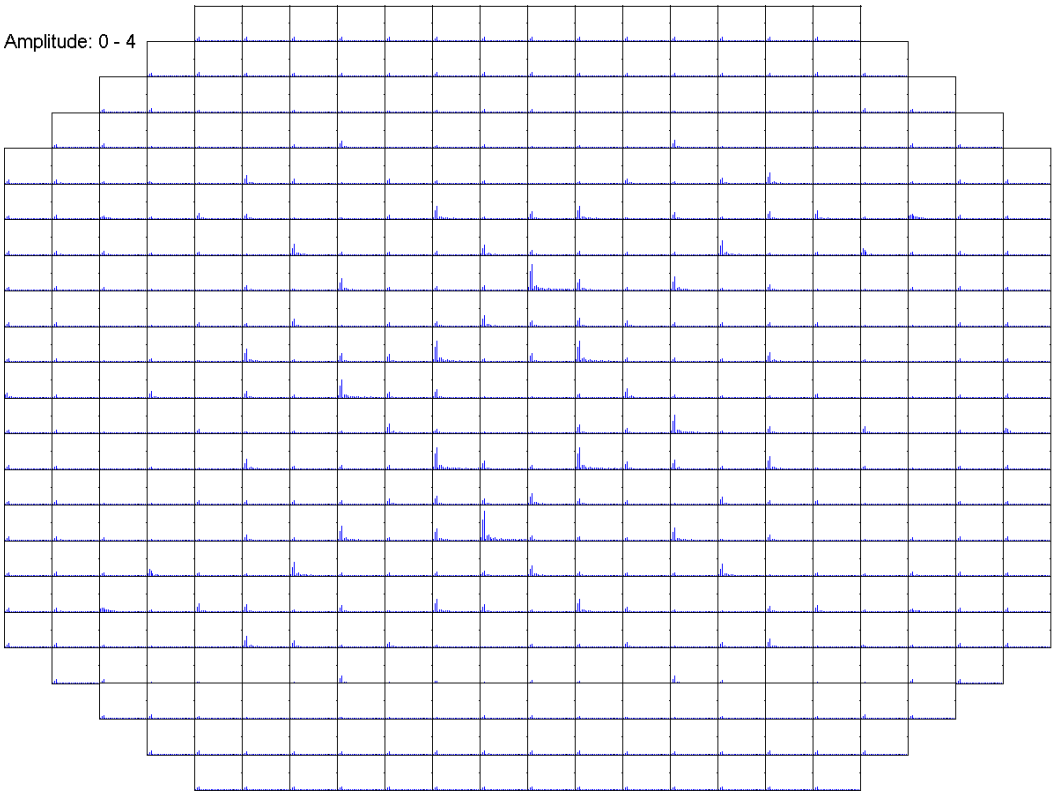

Figure 6.11: Example of a FFT application on the oscillating component of input signals in radial direction.

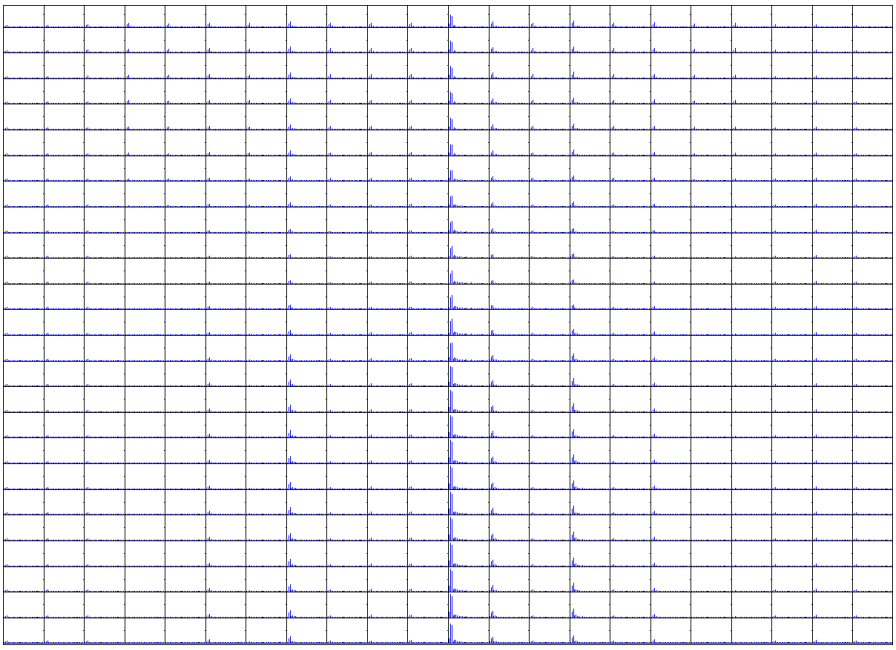

Figure 6.12: Example of a FFT application on the oscillating component of input signals in axial direction.

6.4 Phase Shift Determination between oscillating Parameters

The response behavior of local signals relative to each other during a transient is of special interest. Figure 6.13 shows the time trend of three different simulated signals in the first row and their normalized oscillating component in the second row. The first column represents the total reactor power, the middle and the right column the total mass flow rates of two different channels. It can be noticed that the three signals have a phase shift relative to each other and these phase shifts are determined in using the following procedure.
The described procedure from section 6.3 is repeated and a FFT calculation of each oscillating signal is performed with MATLAB. In the next step for each FFT output the maximum absolute value of the amplitude is determined and marked with a red color as seen in the first row of Figure 6.14. This represents the

dominant frequency in the signal. Next, the corresponding phase is calculated with the MATLAB function `angle` that returns the phase angles in radians for each element of a complex array. The phase angles are further converted from radians to degrees and presented in the second row of Figure 6.14 where the phase angles of the dominant frequencies are again marked red. The determined phase angles in degree are plotted in the second row of Figure 6.15. The power signal is used as a reference and the third row of Figure 6.15 shows the phase shifts, calculated by subtracting the phase of the reference signal from the phase of each signal. With the use of the reference phase, the phase shift of each signal is normalized and the phase shifts of the signals are then comparable.

In order to verify the procedure, the Inverse Fast Fourier Transform (IFFT) is used to transform the dominant signal component from the frequency domain back to the time domain using the MATLAB function `y = ifft (X)` . In Figure 6.15 the first row shows inversely transformed signals (green curves) versus the original signals (blue curves). The reconstructed signals represent the original signals with respect to the frequency and the phase in a good manner.

In this example a signal time frame of 14 seconds is shown. For the analysis of a transient, where the signals change over time, it is an advantage to use very short time frames and analyze one time frame after another in order to investigate changes of the phase of each analyzed signal. In Appendix A.2 this procedure is tested for time frame lengths from 2 seconds to 15 seconds. It is shown that a time frame length shorter than five seconds leads to insufficient results. As the oscillation frequency is of about 0.4 Hz, a time frame length of 5 seconds corresponds to 2 complete oscillation cycles. Therefore in the further analysis of this work a time frame length of 5 seconds is used.

At this point a further remark is necessary. In the above presented procedure the calculation of the phase shift only works correctly if the input signals have a sinusoidal shape. If the signals were be very noisy then a phase shift calculation is hardly helpful. Therefore the described FFT calculation output from section 6.3 would have a low amplitude peak and a broad shape that has to be incorporated in the analysis. Elimination of the noise by filtering procedures may help to yield

a periodic signal which can then be treated in the manner described above.

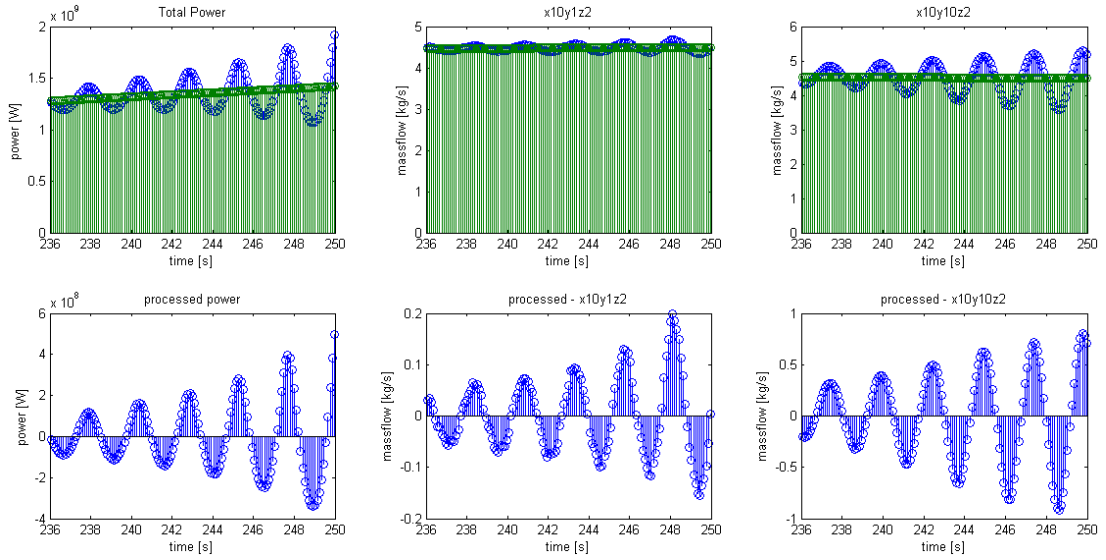

Figure 6.13: Input signals and their oscillating component: total reactor power, massflow channel x10 y1 z2, massflow channel x10 y10 z2.

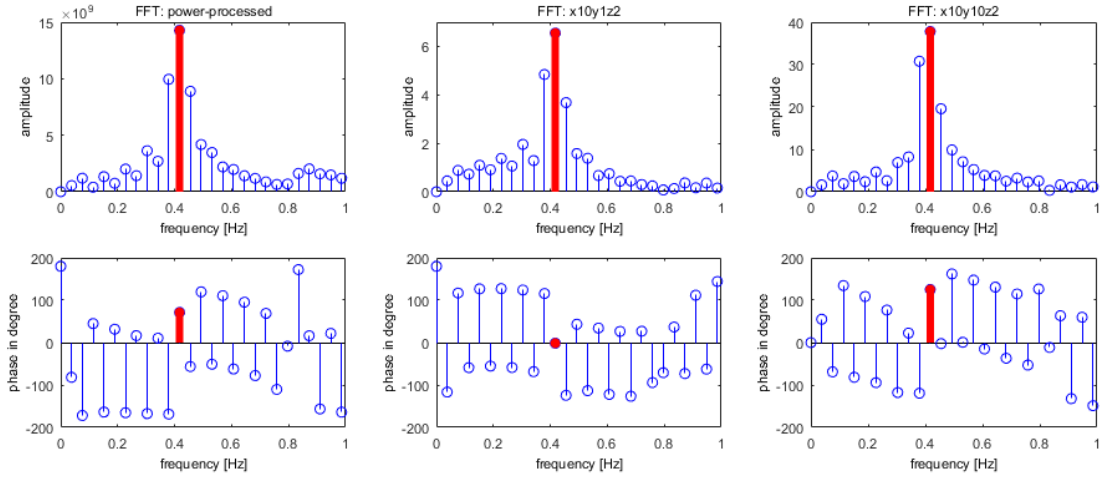

Figure 6.14: Spectral analysis output and phase, with dominating frequency and associated phase marked red.

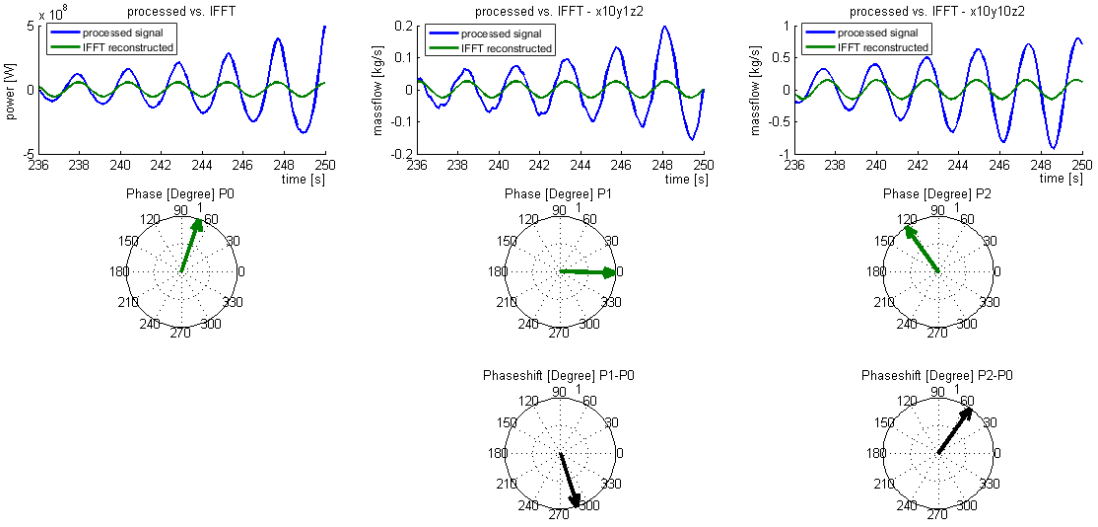

Figure 6.15: First row: processed signal vs. IFFT; second row: phase of dominant signal; third row: phase shift of signal 1 (x10 y1 z2) and signal 2 (x10 y10 z2) with respect to the total power as reference phase.

Chapter 7

Analysis of the O2-1999 Feedwater Transient

This chapter describes the analysis of the coupled TRACE/PARCS simulation of the Oskarshamn-2 reactor with regard to the oscillation in local core regions. The FFT analysis method is employed together with the calculation of phase shifts of local parameters as described in chapter 6.
The data used in this chapter are the simulation results of the Oskarshamn-2 1999 feedwater transient obtained with the coupled system code TRACE/PARCS presented in section 5.3.

7.1 Application of the FFT-Procedure to the Simulation's Output Values

The values selected for the application of the FFT-procedure are the power of each individual channel (assembly power), the channel power in the axial direction (node power), as well as, fluid pressure, fluid density and fluid total mass flow in both axial and radial directions. The selected time interval for the spectral analysis of these parameters is from 237.0 s to 242.0 s as shown in Figure 7.1.

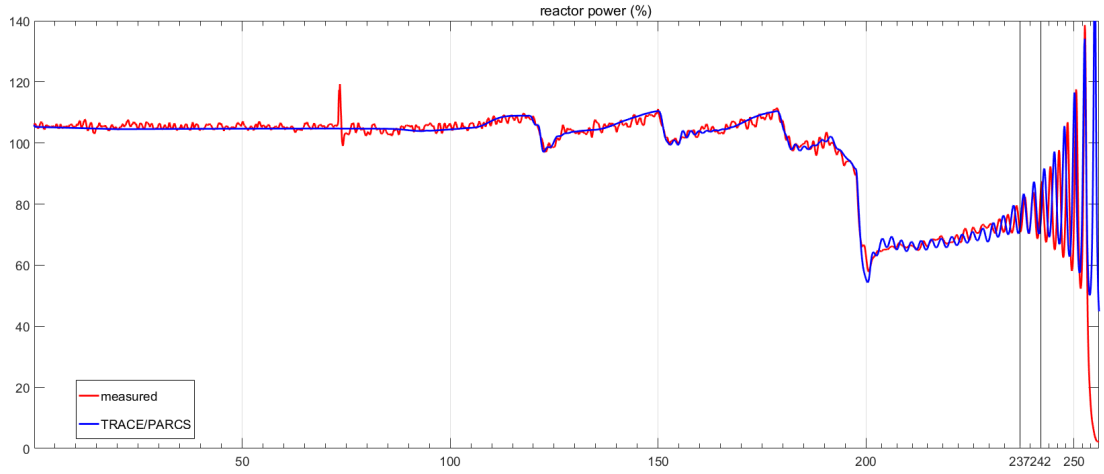

Figure 7.1: O2-1999 FW-Transient: reactor power.

7.1.1 Reactor Power

The channel powers of the 444 individual fuel channels are the selected input signals and their spectral analysis is shown in Figure 7.2. This Figure clearly presents homogeneous oscillations, even though the channels located in the core periphery and semi-pheriphery regions show lower oscillations compared to the central channels.

The spectral analysis of the node power in the axial direction at the radial location corresponding to x=8, y=1-22 is shown in Figure 7.3. Again the channles in the peripheral areas show lower oscillations compared to those in the central core regions. It is remarkable that some central channels (marked with red arrows) show higher oscillations compared to direct adjoining channels. All of these channels have their maximum oscillation amplitude in the axial location of about z=13 which corresponds to an elevation of about 1 meter.

Selecting the axial location of z=13 for the spectral analysis of the node power in the radial direction, Figure 7.4 shows nodes with slight tendencies for enhanced oscillation. However, a clear determination can not be done.

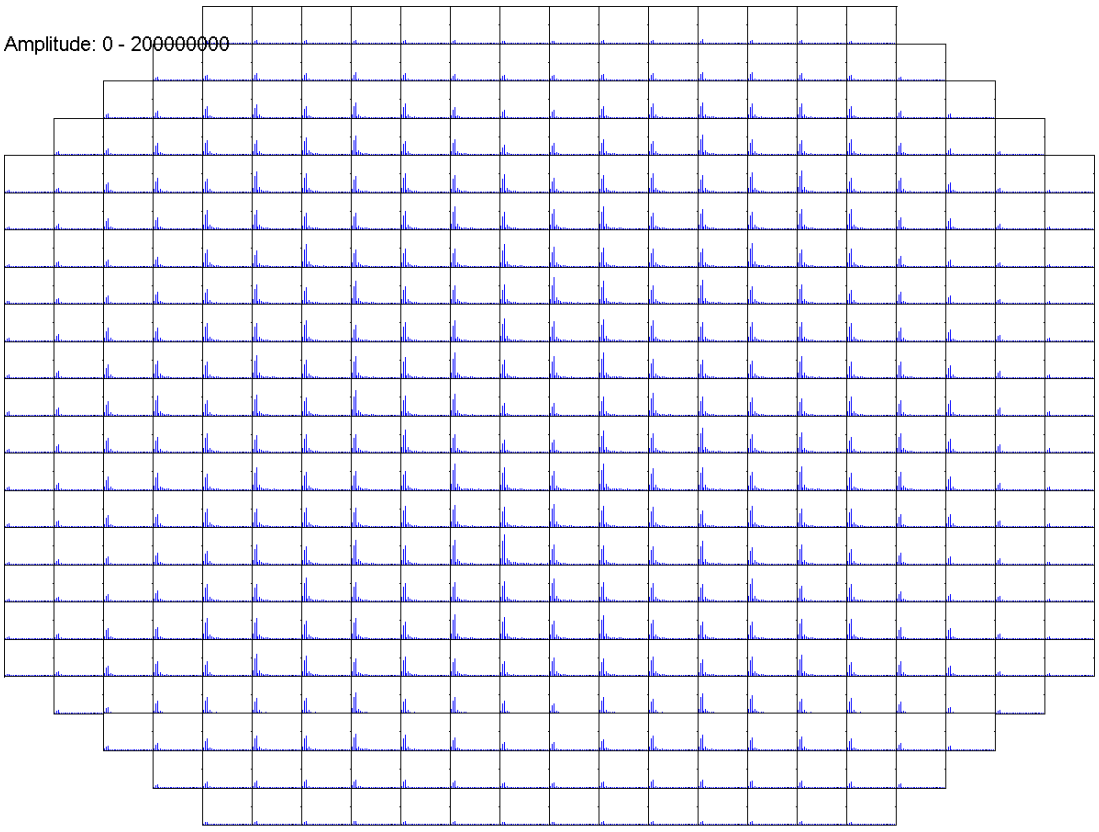

Figure 7.2: FFT applied on the assembly total power.

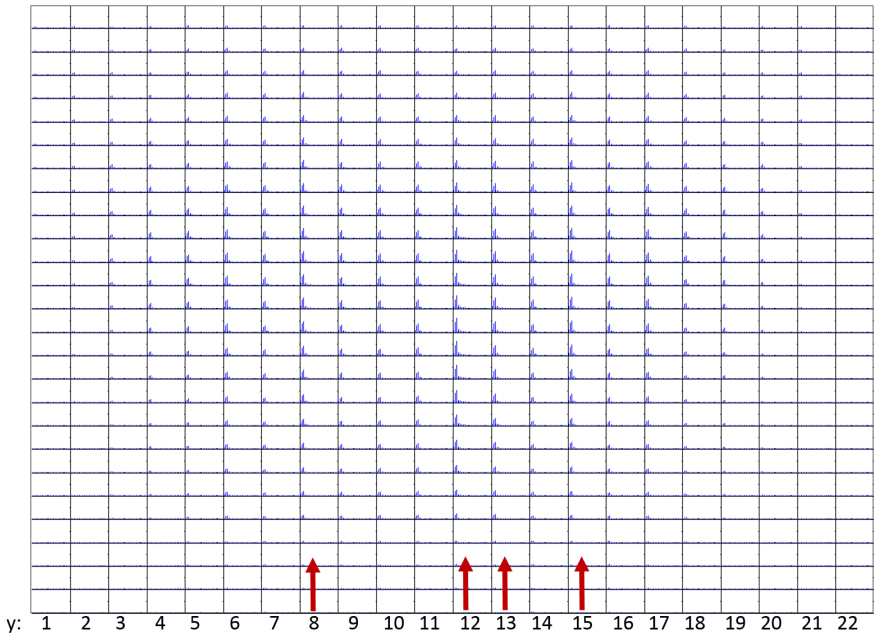

Figure 7.3: FFT applied on the nodal power in axial direction x=8, y=1-22, 237.0 s $\leq$ t $\leq$ 242.0 s.

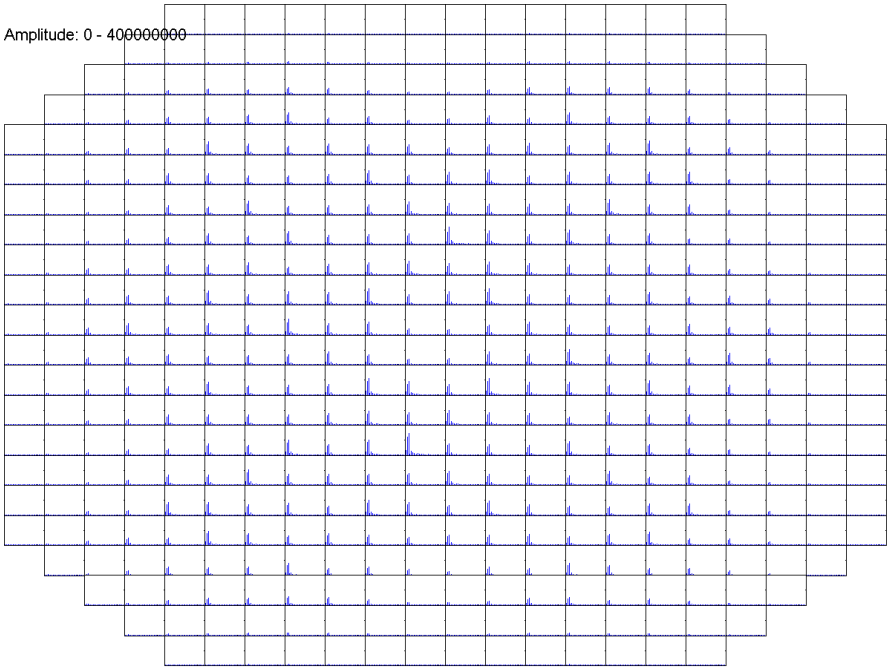

Figure 7.4: FFT applied on the nodal power in radial direction, z=13, 237.0 s $\leq$ t $\leq$ 242.0 s.

7.1.2 Fluid Pressure

The FFT-procedure for the fluid pressure is performed and the spectral analysis is presented for both axial (Figure 7.5) and radial direction (Figure 7.6). The oscillation behaviour is in both cases very homogenous, wherefore the analysis of the pressure seems not to be an appropriate parameter in order to detect local particularities in the oscillatory behaviour.

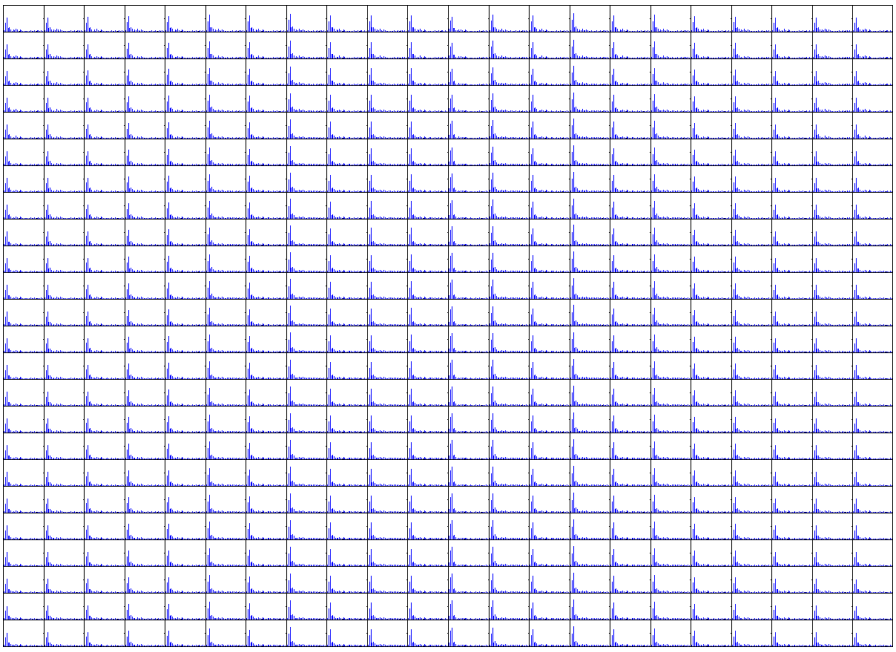

Figure 7.5: FFT applied on the pressure in axial direction, x=8, y=1-22, 237.0 s $\leq$ t $\leq$ 242.0 s.

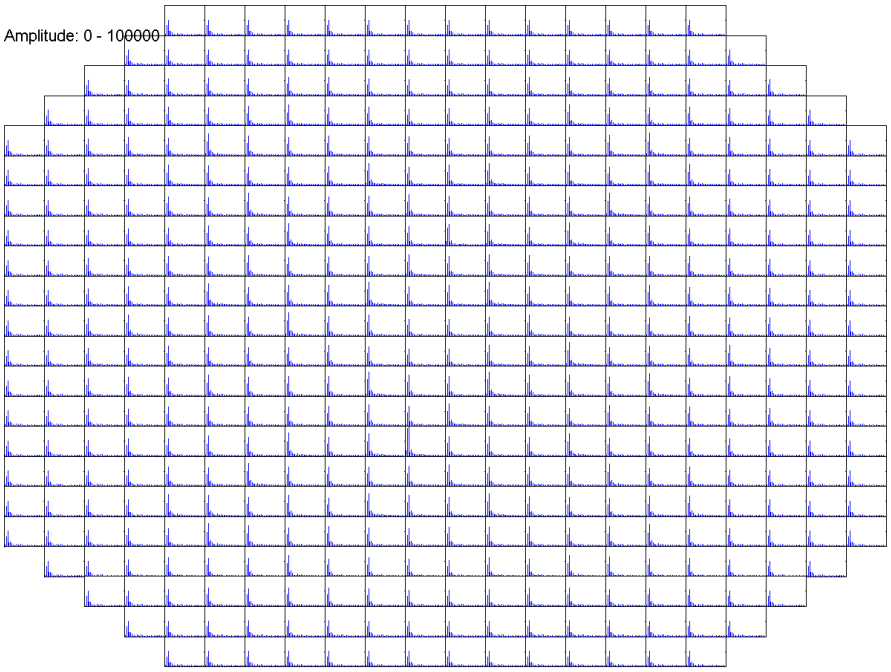

Figure 7.6: FFT applied on the pressure in radial direction z=13, 237.0 s $\leq$ t $\leq$ 242.0 s.

7.1.3 Fluid Density

The spectral analysis of the fluid density in axial direction x=8, depicted in Figure 7.7, shows outstanding oscillation of channel y=12 at an axial position around level z=13. The fluid density oscillation in the channels y= 8, 13, 15 is much lower compared to channel y=12 but still recognizable. For all other channels there is no, or almost no, oscillation in density detectable.

According to Figure 7.8, the spectral analysis is performed in the radial direction for the axial level z=13 where density oscillations in the axial direction are the strongest. Striking oscillations in the density of the channels corresponding to x=8, y=12 and x=15, y=11 are recognizable. Besides these two strongly striking channels, a pattern of channels with oscillations of the fluid density is clearly recognizable.

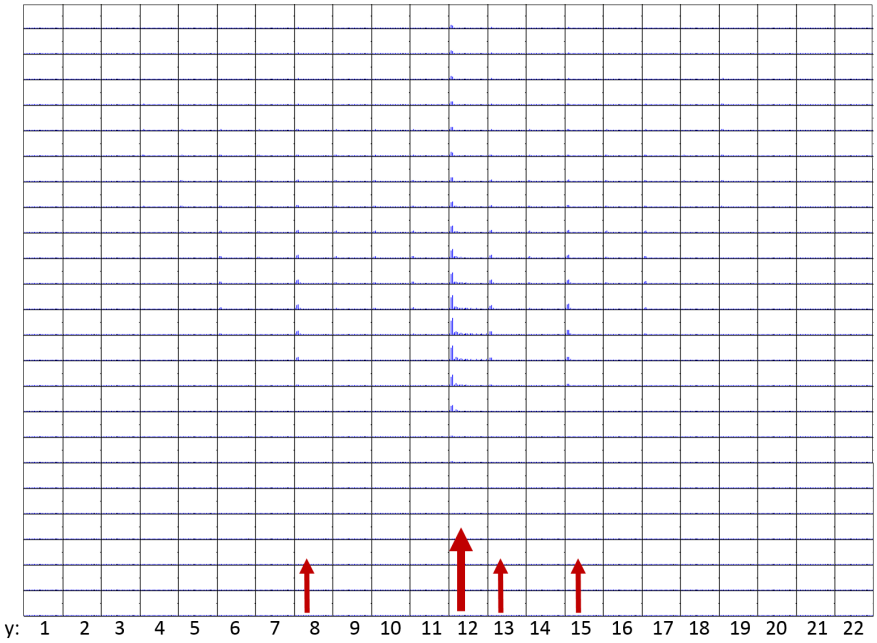

Figure 7.7: FFT applied on the density in axial direction, x=8, y=1-22, 237.0 s $\leq$ t $\leq$ 242.0 s.

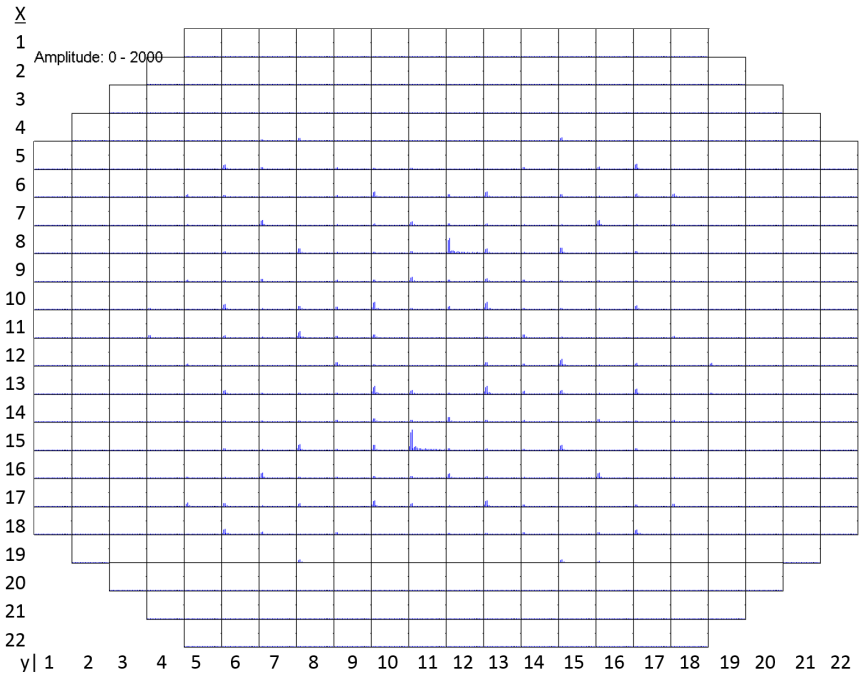

Figure 7.8: FFT applied on the density in radial direction z=13, 237.0 s $\leq$ t $\leq$ 242.0 s.

7.1.4 Fluid Mass Flow Rate

The FFT-procedure is applied to the total mass flow rate in axial direction x=8 and the spectral analysis results are shown in Figure 7.9. In accordance with the analysis of the fluid density in the axial direction, the mass flow rate in channel y=12 shows again considerable oscillations. Accordingly, the mass flow rate oscillation of the channels y= 8, 13, 15 is lower compared to channel y=12. In contrast to the axial analysis of the density, the remaining channels still show oscillations, even though their magnitude is very small compared to the before mentioned channels. However, for the spectral analysis of the mass flow rate in the axial direction, for all channels is to be noted that the oscillations are highest at the bottom part of the channels, but are prevailing throughout the whole axial length of the channel. Considering the spectral analysis of the total mass flow in the radial direction at level z=13, as shown in Figure 7.10, the channels with the position x=8, y=12 and x=15, y=11 can be repeatedly identified as the channels with governing oscillation. The same channels have already been identified by means of the spectral analysis of the fluid density presented in section 7.1.3.
Further, a pattern with channels with lower, but clearly recognizable oscillation can be identified. This pattern of channels is congruent with the pattern of channels of the fluid density analysis.
Generally it can be noted that the spectral analysis of the mass flow shows stronger oscillation amplitudes compared to the spectral analysis of the density.

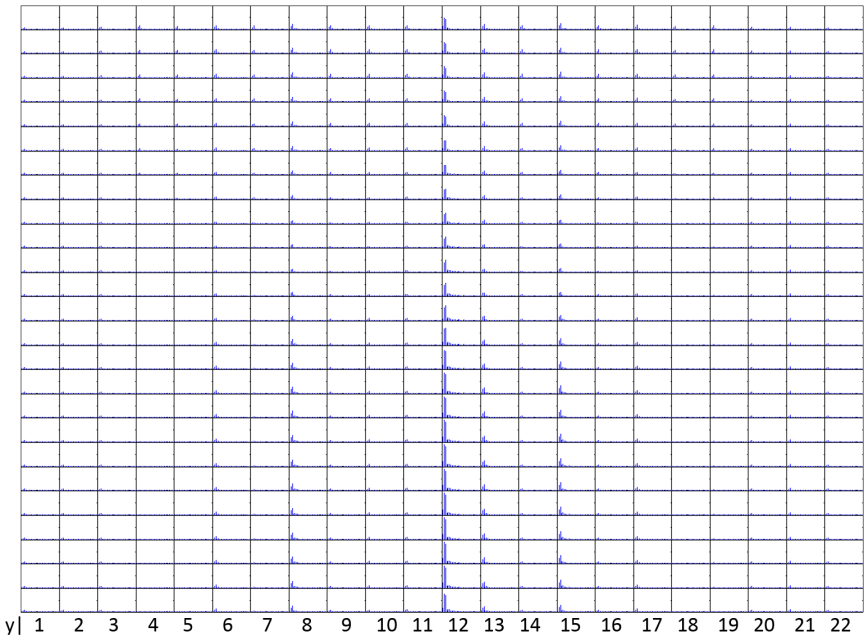

Figure 7.9: FFT applied on the mass flow in axial direction x=8, y=1-22, 237.0 s $\leq$ t $\leq$ 242.0 s.

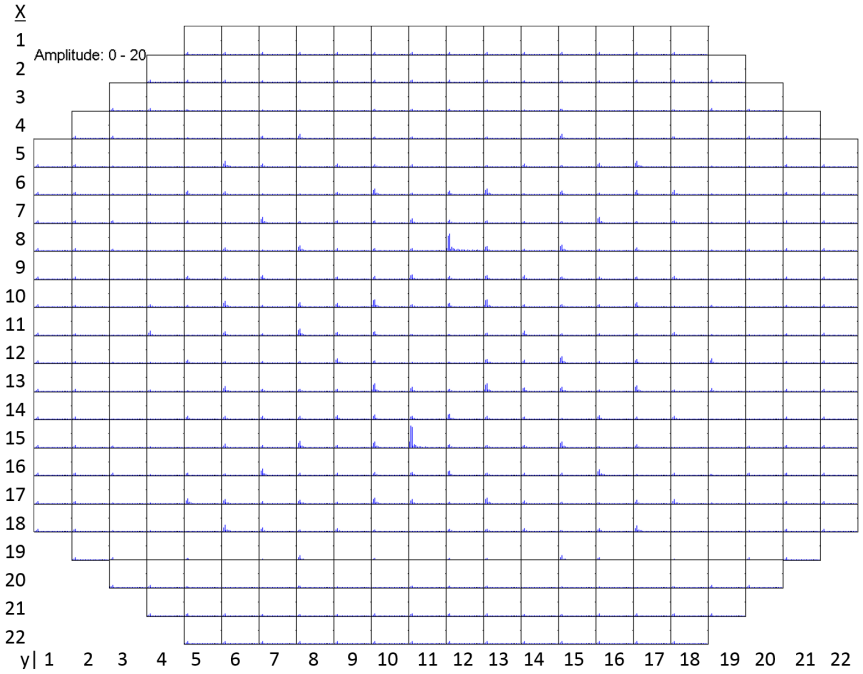

Figure 7.10: FFT applied on the mass flow in radial direction z=13, 237.0 s $\leq$ t $\leq$ 242.0 s

7.2 Application of the FFT - Method considering the time-dependent Evolution of the Oscillation

In the previous section 7.1 the FFT-procedure was applied to several output parameters from the TRACE/PARCS simulation of the O2-1999 FW-Transient. Amongst all examined parameters, the total mass flow rate through the channels showed the clearest expression of the oscillations. This is in accordance with theory presented in chapter 2. The present O2-1999 FW-Transient is a instability event with core-wide (in-phase) mode of oscillation.
Relying on the theory that the channel with the highest power is the most unstable one which tends to dominate the overall response [1], Figure 7.11 shows the radial power distribution together with the spectral analysis of the radial channel mass flow rate. Channel 754 (x=15, y=11 and marked as **1**) is the hottest channel with a relative power ratio of 1.8332 followed by channel 719 (x=8, y=12 and marked as **2**) with a relative power ratio of 1.8054. These two channels are, considering the mapping, symmetric channels. Regarding the results of the FFT-procedure of the mass flow rate, it is clearly recognizable that the oscillation of this parameter reaches also a maximum in the channels 754 and 719. The intensity of the mass flow rate oscillation correlates with the relative power. This confirms the observation of the next hot channels, whereby the tendency continues that the lower the power of these channels is, the lower the mass flow oscillation is.
The evolution of the mass flow rate oscillation during the transient after the partial scram is depicted for the time intervals 215 s - 220 s and 225 s - 230 s in Figure 7.12 and for the time frames 235 s - 240 s and 245 s - 250 s in Figure 7.13. With the growth of the the total power oscillation, the mass flow rate oscillation is growing analogously, once more confirming that the channels with the higher powers induce dominating mass flow rate oscillations.

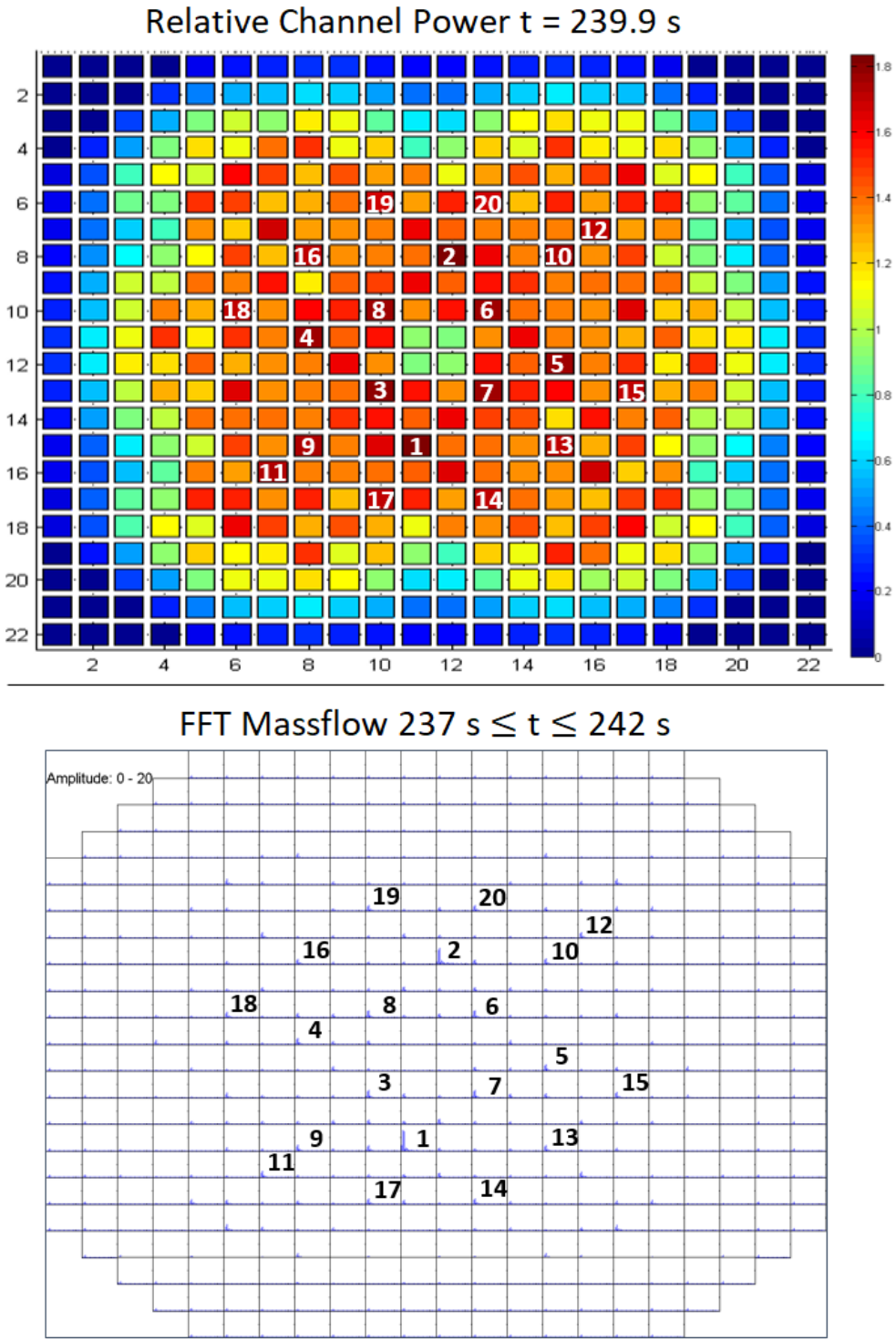

Figure 7.11: Relative channel power at time = 239.9 s (top) and FFT applied on the mass flow for the time interval 237 s - 242 s (bottom).

marker	relative power ratio	channel no.	x-pos.	y-pos.	assembly type
1	1.8332	754	15	11	QD
2	1.8054	719	8	12	QD
3	1.7763	744	13	10	QD
4	1.7739	734	11	8	QD
5	1.7738	739	12	15	QD
6	1.7668	729	10	13	QD
7	1.7659	745	13	13	QD
8	1.7590	728	10	10	QD

Table 7.1: Relative channel power ratio at time 239.9 s.

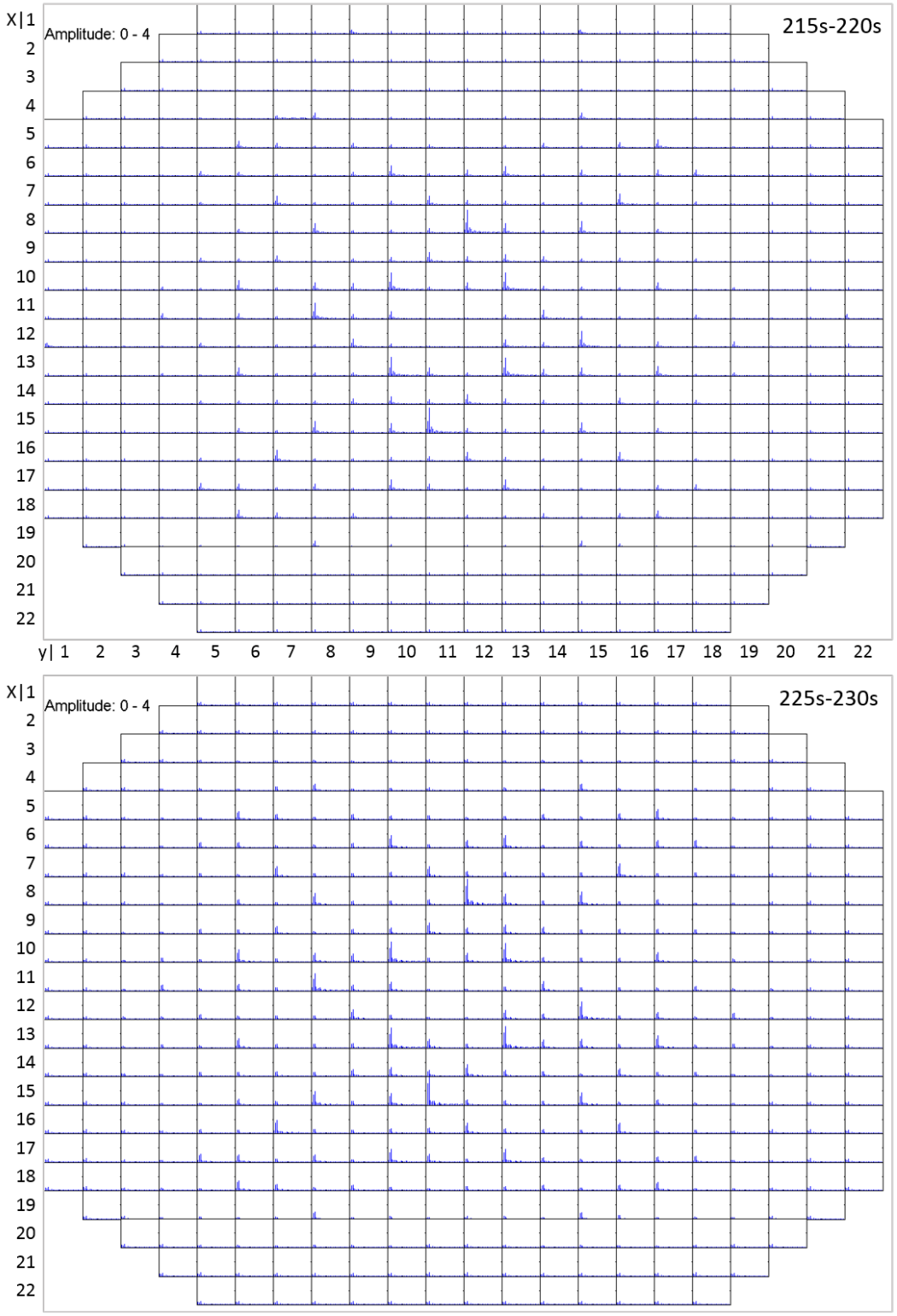

Figure 7.12: FFT applied on the mass flow rate at the channel inlet for the time frame 215 s - 220 s (picture top) and the time frame 225 s - 230 s (picture bottom).

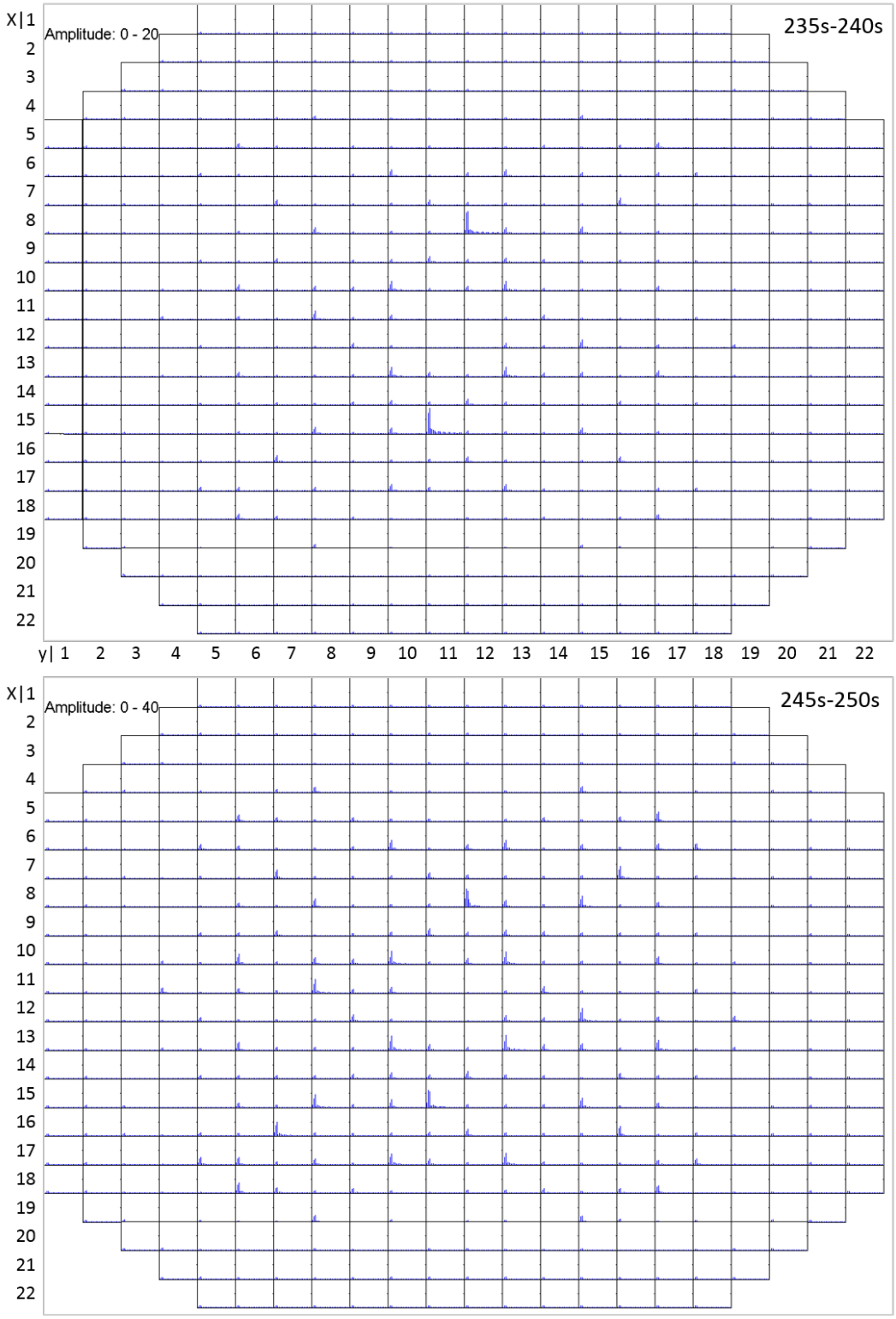

Figure 7.13: FFT applied on the mass flow rate at the channel inlet for the time frame 235 s - 240 s (picture top) and the time frame 245 s - 250 s (picture bottom).

7.3 Application of the Phase Shift Analysis for BWR Instability

7.3.1 Analysis of the Channel Power

The Oskarshamn-2 1999 feedwater transient is described as a pure *in-phase* power oscillation. In order to confirm that the transient is indeed a pure in-phase power oscillation, a phase shift calculation is performed of the total power as a reference compared against the channel-wise total power. The results of this analysis are graphically presented in Figure 7.14. It can be noticed that all core channels have the same phase, that is almost 0 °. The result of this calculation remains unchanged throughout the investigated interval between 220 s and 250 s.

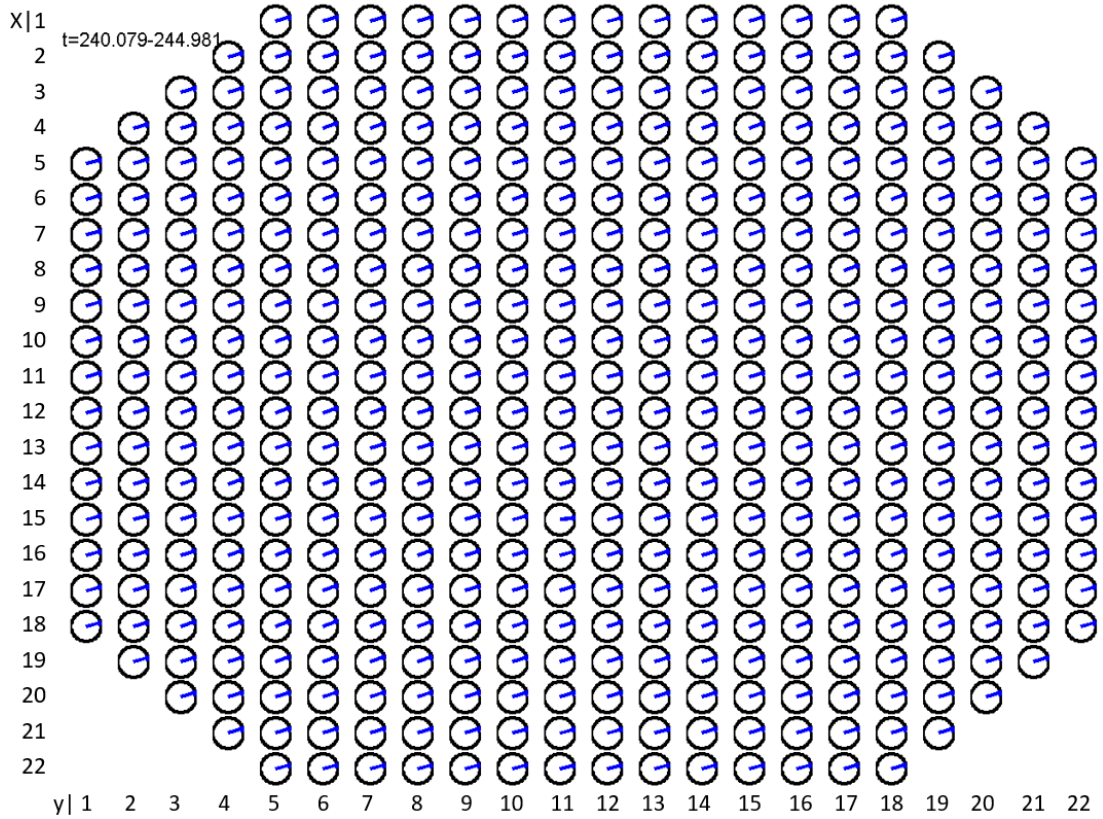

Figure 7.14: Phase shift calculation of the channel power for the time interval 240 s - 245 s.

7.3.2 Massflow Rate Analysis of the Core Channels Inlet

The radial mass flow rate distribution at the channel bottom for the time interval from 234.13 s (image A) to 236.97 s (image O) with a constant image rate of 0.2 s is presented in Figure 7.15. For the mass flow distribution a relative representation was preferred to the absolute one, in order to make small mass flow oscillations visible and easier to compare. The relative representation is generated by dividing the absolute mass flow rate of each core channel by its mean value for the considered time interval. The mass flow of each channel is presented as a colored bar, where blue represents a lower mass flow rate and red represents a higher mass flow rate. It has to be mentioned that for a better visualization the color scheme is selected within a very tight range and therefore becomes overstated, meaning that this figure is intended as a qualitative representation only.
From the first image A at 234.13 s to image E the mass flow rate of the channels in the center part of the core is increasing, thus changing the bar color to red, while simultaneously the mass flow rate of the channels in the periphery and semi-periphery is decreasing and the bar color changes to blue. From image F on, the mass flow rates in the center of the core start to decrease while the mass flow rates of the channels in the periphery and semi-periphery are increasing. This can be observed until the time point corresponding to image K. From image L on, the the mass flow rates in the central core channels increase again, while those in the peripheral and semi-peripheral regions are decreasing.
Summarizing, it can be observed that the mass flow rates at the inlet of the channels oscillate with a phase shift between the central channels and the (semi-) peripheral channels.

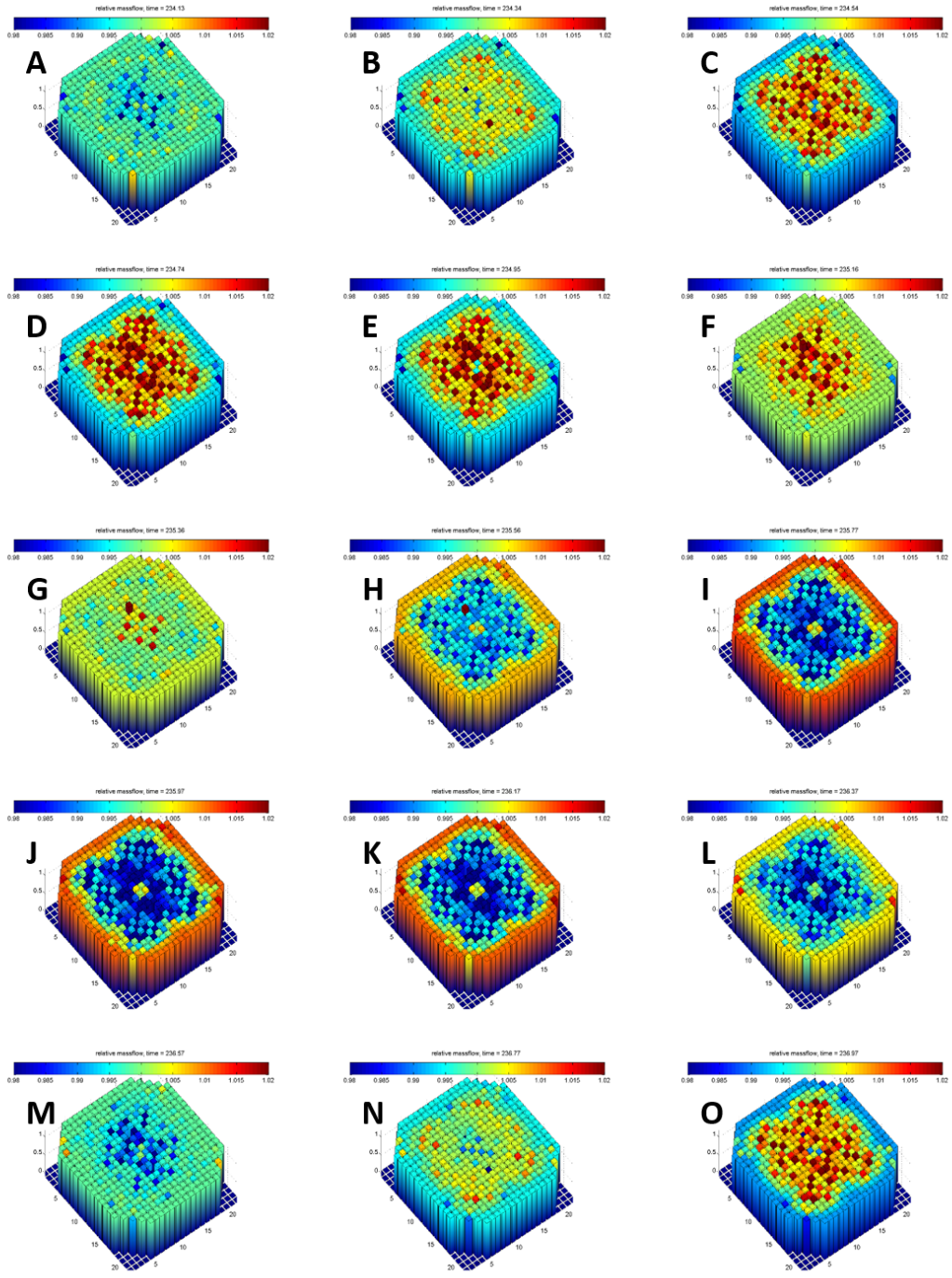

Figure 7.15: Relative mass flow rate at the channel inlet from time point 234.13 s to time point 236.97 s.

7.3.3 Phase Shift Analysis between representative Single Channels

The following analysis corresponds to channel 718 (x=8, y=8) selected as a representative channel for the central part of the core and to channel 426 (x=8, y=1) chosen as a representative for the peripheral core region.

Figure 7.16 shows the absolute mass flow rate of the lower plenum, the mass flow rate through channel 718 at the inlet, the mass flow rate at equidistantly distributed axial positions of the channel, channel outlet, and the mass flow rate of the upper plenum for the time frame from 230 s to 250 s. It can be seen that the mass flow oscillates sinusoidally in all regarded positions. According to the theory described in Chapter 2.1, the density-wave mechanism can be observed here as follows: the sinusoidal wave that arrives at the channel inlet travels upwards in flow direction and reaches the channel outlet with a delay of 180° with respect to the channel inlet flow. The phase shift of 180° between inlet and outlet mass flow is confirmed by the phase shift calculation depicted in Figure 7.17 by applying the method from Chapter 6.4.

As the mass flow and pressure drop are correlated, an increase in pressure drop at the channel inlet results in a decrease of the pressure drop at the outlet, whereby the conditions of a positive feedback on itself are given for a self-sustaining oscillation condition.

The mass flow rate through the peripheral core channel 426 behaves differently to the central core channel 718 as shown in Figure 7.18. The mass flow rate oscillates sinusoidally from channel inlet throughout channel outlet as well as in the upper plenum where the oscillations have all the same phase. There is no density-wave present resulting from the circumstance that the peripheral core channel have low or virtually no void content. The mass flow rate oscillations of the peripheral core channels have therefore a phase shift of 0° between their inlet and outlet.

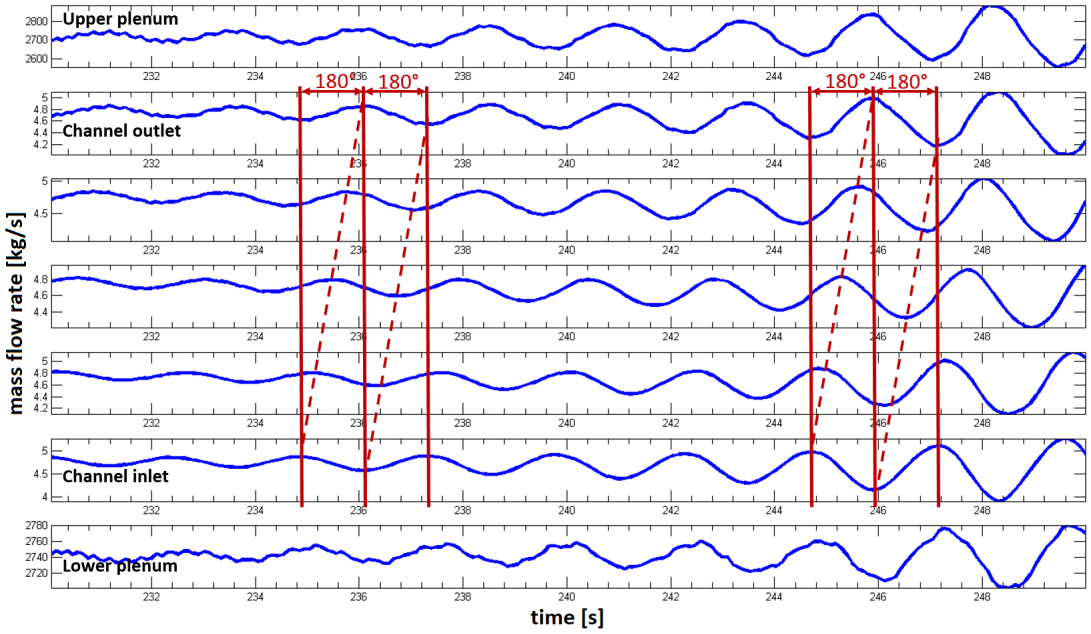

Figure 7.16: Absolute mass flow: lower plenum, channel 718, upper plenum.

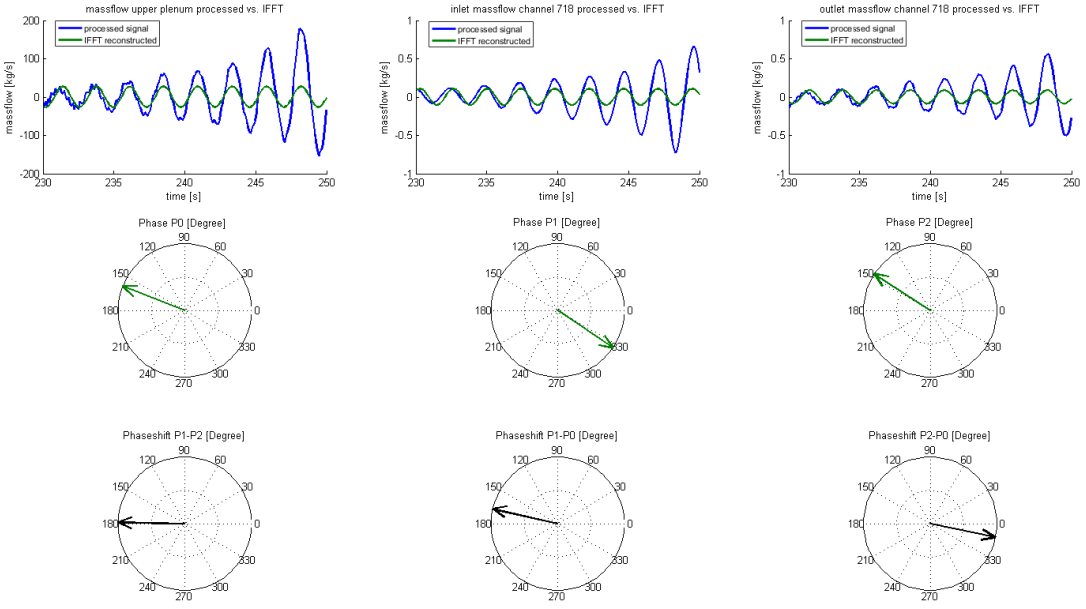

Figure 7.17: Phase shift calculation of the core channel 718 between its inlet and outlet mass flow.

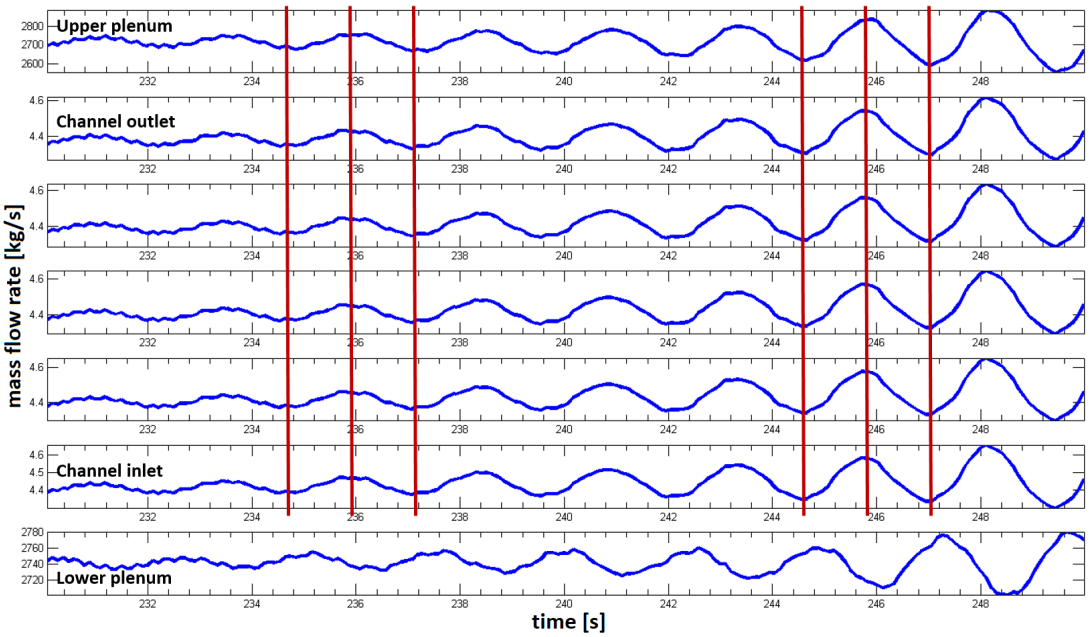

Figure 7.18: Absolute mass flow: lower plenum, channel 426, upper plenum.

The phase shift of the oscillating inlet mass flows of channel 426 and channel 718 with respect to the lower plenum mass flow oscillation for the regarded timeframe 230 s - 250 s are calculated according to the method described in chapter 6.4 and the results are shown in Figure 7.19.

The approximation through the IFFT does not match perfectly for the entire time frame of 20 s. It can, however, be regarded as sufficient for this qualitative analysis. The inlet mass flow rate in the central core channel 718 is shifted by about 30° with respect to the mass flow rate in the lower plenum, while the inlet mass flow rate in the periphery core channel 426 is shifted by approximately 240° with respect to the lower plenum mass flow rate. This results in a phase shift of about 210° between the central core channels and the peripheral ones.
Due to the fact that the mass flow rate of the lower plenum splits up into the mass flow rate through each of the individual core channels and the bypass mass flow rate, it has to be considered how far the bypass mass flow rate oscillates and with which phase. This is shown in Figure 7.20, in which the phase shift calculation is performed for the mass flow rate of the lower plenum as reference compared to

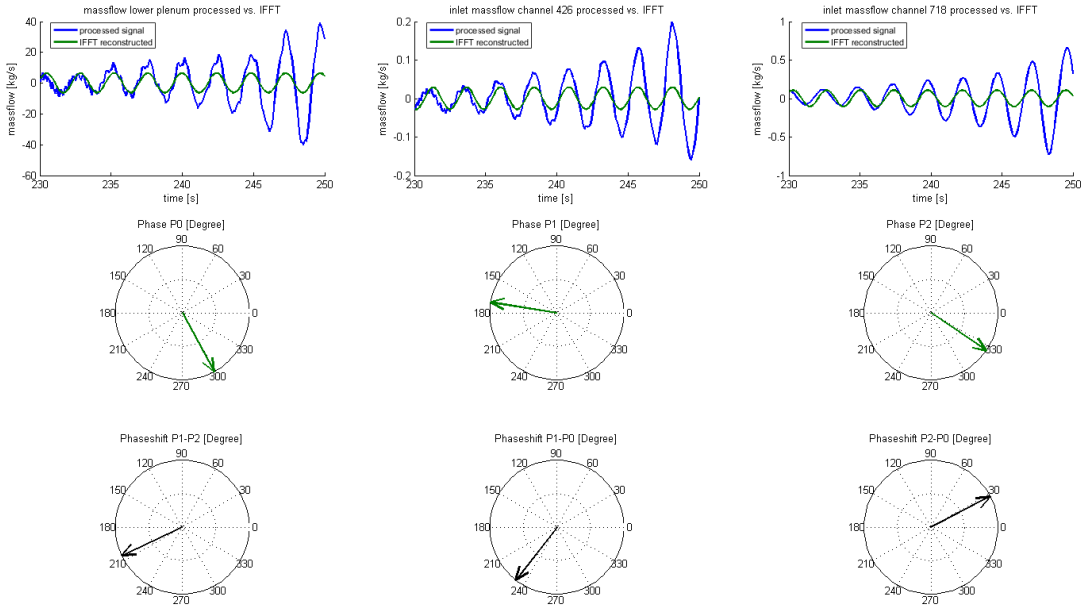

Figure 7.19: Phase shift calculation of inlet mass flow of channels 426 and 718 compared to lower plenum mass flow.

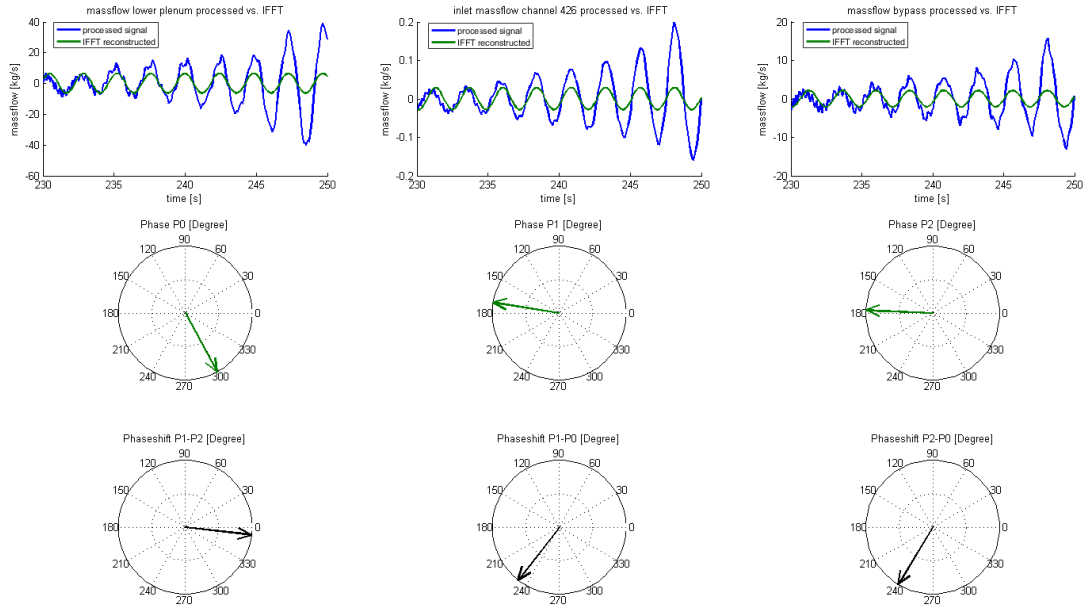

Figure 7.20: Phase shift calculation of inlet mass flow of channel 426 and the bypass inlet mass flow compared to lower plenum mass flow.

the inlet mass flow rate of channel 426 (position x8, y1) and the inlet mass flow rate of the bypass. The phase shift between the bypass mass flow rate and the periphery channel is almost 0°, which means that the bypass mass flow rate and the periphery channels behave in their mass flow rate oscillation simultaneously.

7.3.4 Phase Shift Calculation of all Core Channels in radial Direction at the Inlet and Outlet

Channel 718 (x=8, y=8) was selected to represent the central core channels while channel 426 (x=8, y=1) was chosen being representative for peripheral core channels as a result from the following analysis, where a detailed phase shift calculation of the mass flow rate is performed for all core channels. The considered time interval for this analysis is again from 230 s to 250 s and is subdivided in time frames with a constant length of 5 s. The oscillation of the channel's outlet mass flow rate is referenced to the upper plenum's mass flow rate oscillation while the phase shift is calculated. Accordingly, the phase shift of the oscillation of the channel's mass flow rate at the inlet is calculated with respect to the lower plenum mass flow rate oscillation. With the first Figure 7.21 the time considered interval ranges from 230 s to 235 s, second Figure 7.22 from 235 s to 240 s, third Figure 7.23 from 240 s to 245 s, and the fourth Figure 7.24 from 245 s to 250 s for the phase shift calculation results.
As a general observation, Figure 7.21 to Figure 7.24 show that the mass flow rate of the upper plenum and the mass flow rates of the channels at the outlet have the same phase, which means that the phase shift is almost 0 °.
However, at the channel inlet a distinction between the central core channels and the peripheral core channels with respect to the phase shift of the channel inlet flow and of the lower plenum mass flow has to be made. All peripheral core channels share the same phase. The central core channels have similarly, although with some exceptions, a uniform phase. As already stated in section 7.3.3, channel 426 (x8, y1) is representative for the peripheral core channels and channel 718 (x8, y8) is representative for the central core channels. From the analysis performed here,

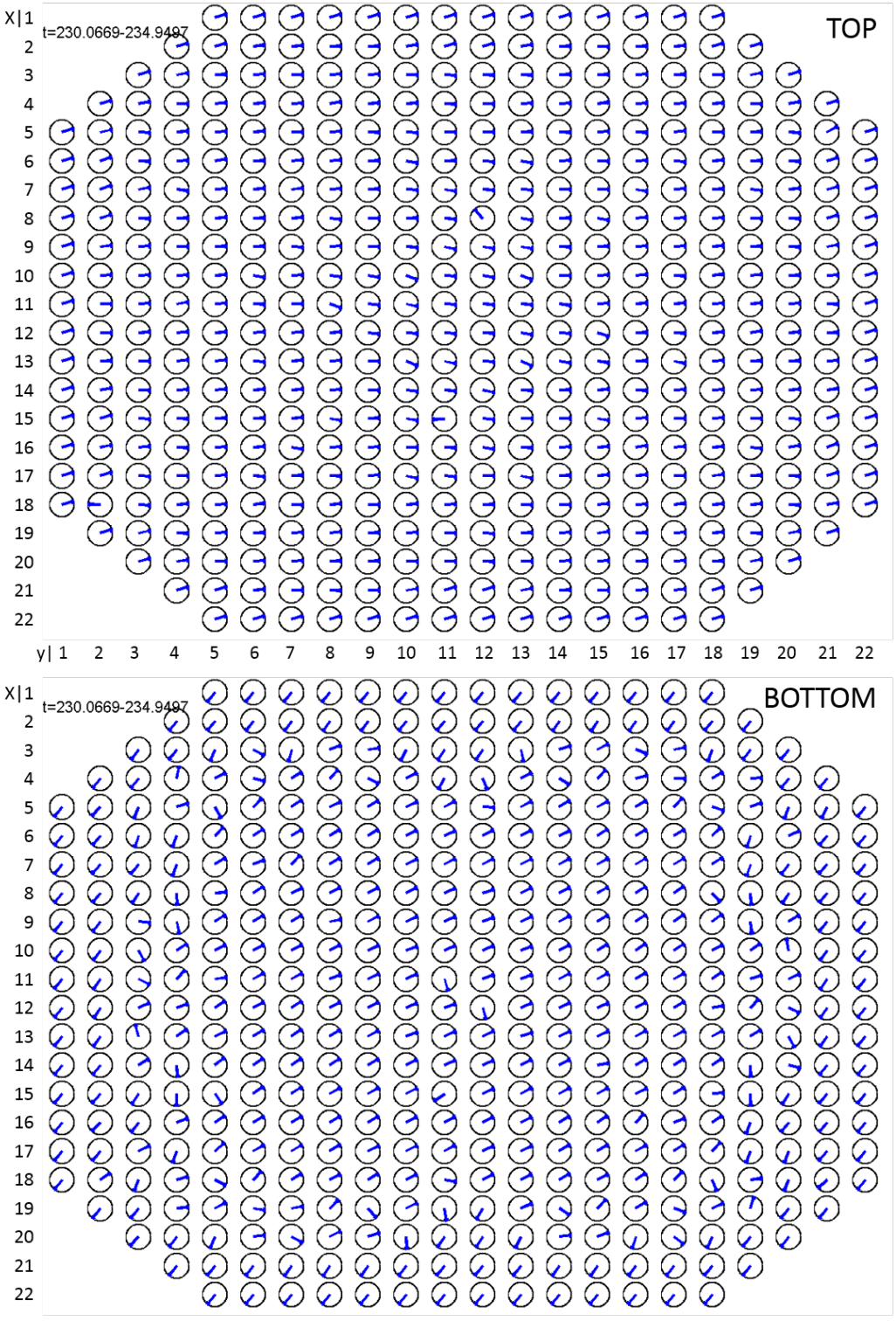

Figure 7.21: Phase shift of channel mass flows at the outlet relative to upper plenum (picture at top) and phase shift of channel mass flow at the inlet relative to lower plenum (picture at bottom), timeframe 230 s - 235 s.

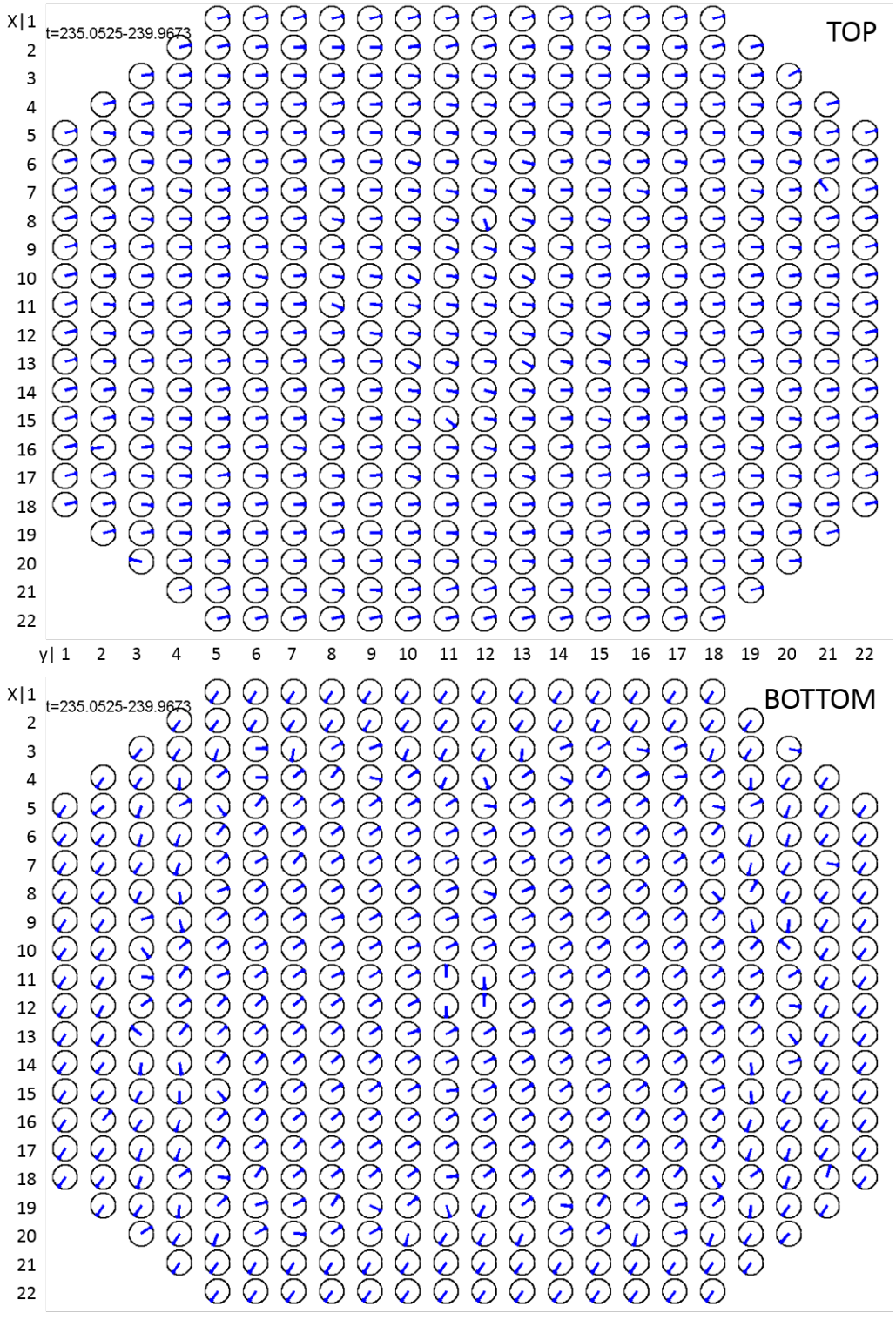

Figure 7.22: Phase shift of channel mass flows at the outlet relative to upper plenum (picture at top) and phase shift of channel mass flow at the inlet relative to lower plenum (picture at bottom), timeframe 235 s - 240 s.

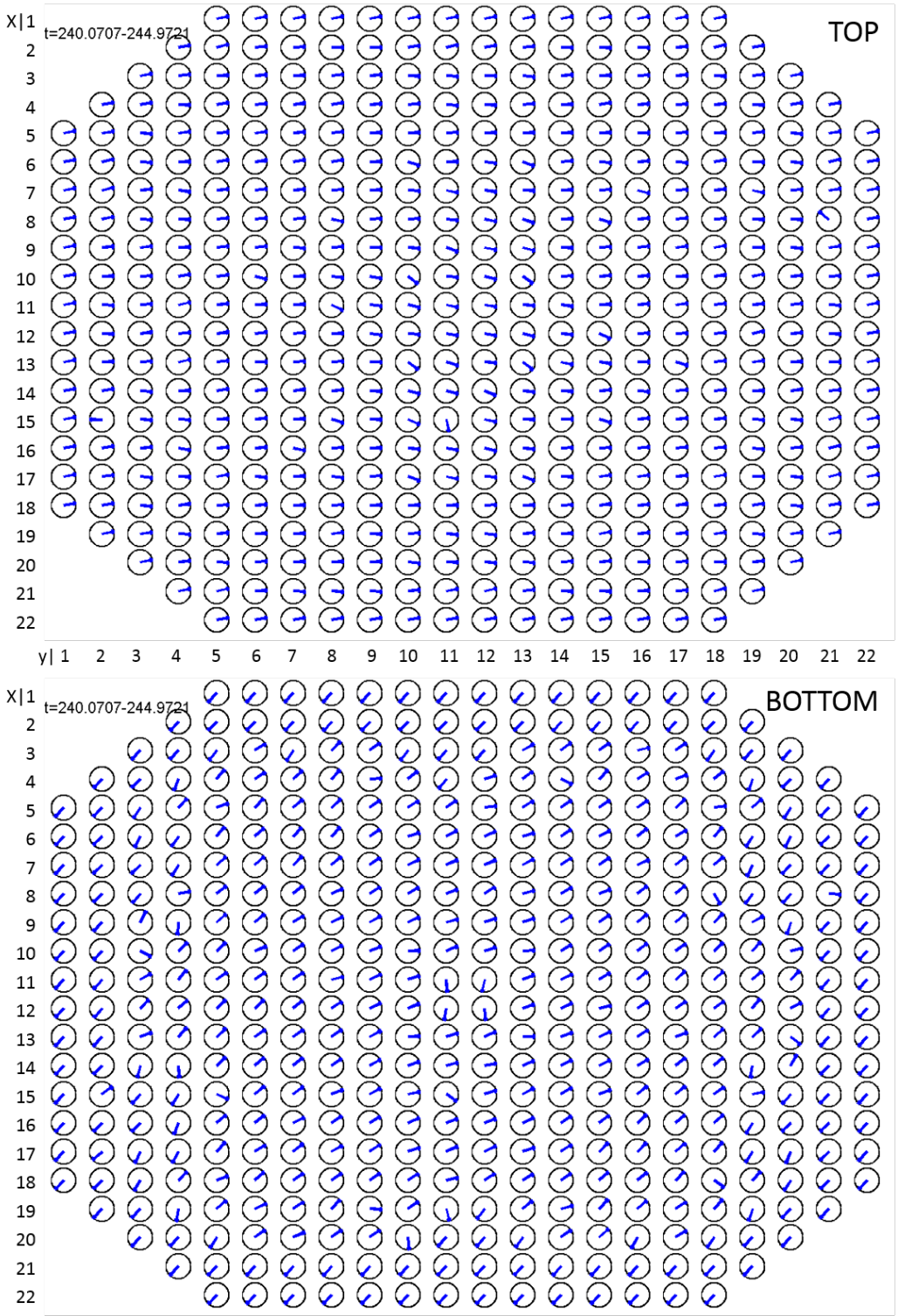

Figure 7.23: Phase shift of channel mass flows at the outlet relative to upper plenum (picture at top) and phase shift of channel mass flow at the inlet relative to lower plenum (picture at bottom), timeframe 240 s - 245 s.

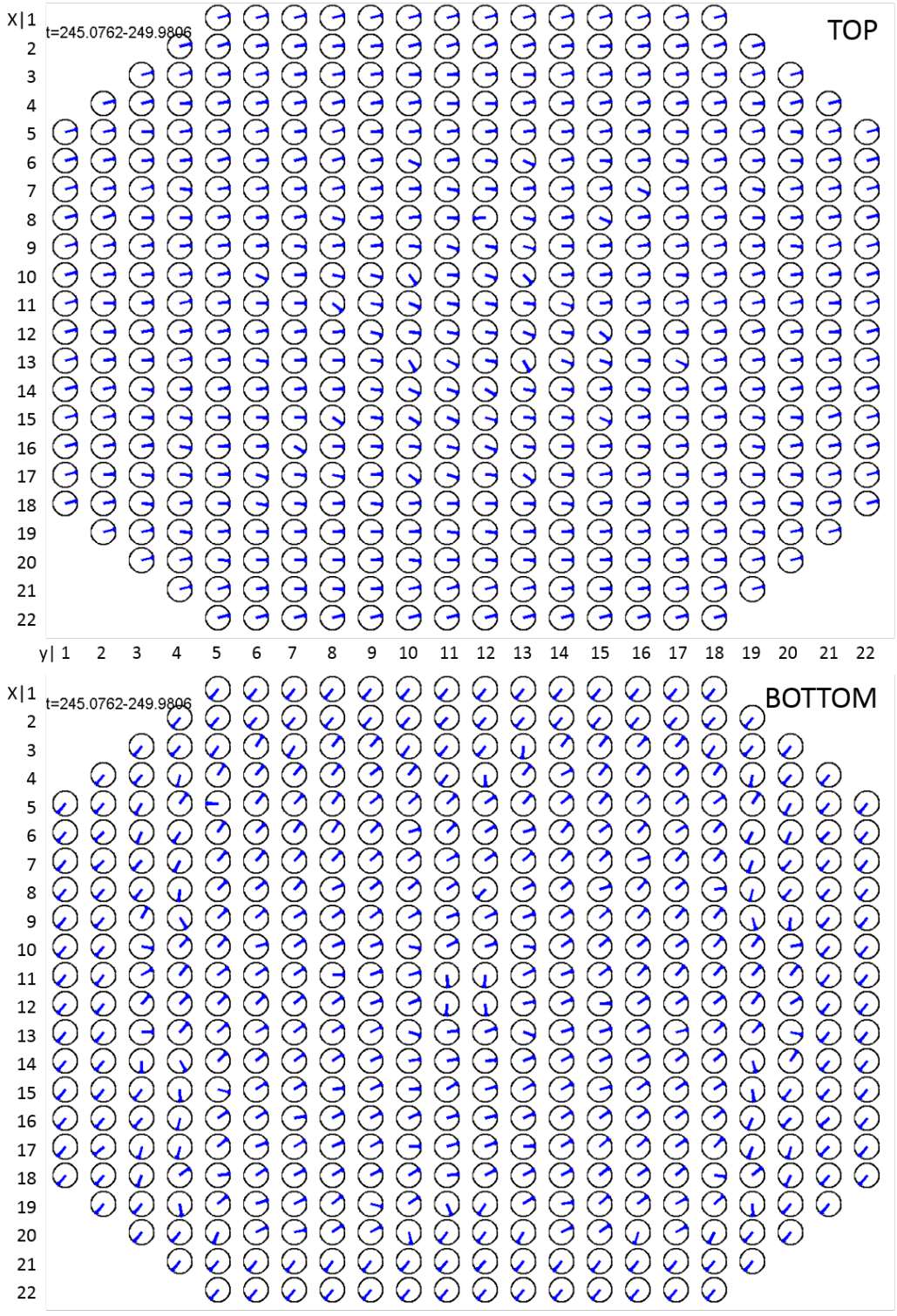

Figure 7.24: Phase shift of channel mass flows at the outlet relative to upper plenum (picture at top) and phase shift of channel mass flow at the inlet relative to lower plenum (picture at bottom), timeframe 245 s - 250 s.

a phase shift between central and periphery channels of about 210° is determined.

Between the peripheral core channels and the central core channels, a transition zone can be identified. In this transition zone the mass flow rates of the channels have non-uniform phase shifts and are disordered.
The attention is now devoted to the mass flow rate oscillations of the central core channels as a kind of out-of-phase oscillation to the peripheral core channels together with the bypass. When the central core channels increase their mass flow rates, the peripheral core channels and the bypass reduce their mass flow rates and vice-versa, although the phase shift between the central and the peripheral channels is 210 ° with 30° differing from an optimum positive feedback of 180 °. However, the occurrence that the peripheral core channel mass flow rates oscillate out-of-phase with respect to the central core channel mass flow rates has a positive effect on the development and preservation of self-sustaining mass flow oscillations.

Chapter 8

Study Case: Redesign of the Core Pattern

The channels 754 and 719 were observed to be the hottest channels and the ones with highest intensity of massflow oscillation as described in section 7.2 and depicted in Figure 7.11. In this study, named Study Case, these two channels are exchanged with two other channels with the aim to investigate the influence of the hottest channels with the highest mass flow rate oscillation on the over-all evolution of the total power oscillation.

8.1 Modelling Description of the Study Case

The requirement to find a new suitable position was to keep these channels in the central part of the core, to not reposition them in the neighborhood of an other QD-type channel, keep core symmetry and to find a region where mass flow oscillations are very low. The applied strategy consisted of exchanging channel 719 (x=8, y=12) with channel 103 (x=3, y=16) and exchanging channel 754 (x=15, y=11) with channel 196 (x=20, y=7) according to Figure 8.1.
The exchange of the channels is performed by adapting the TRACE input file and the PARCS input files, the *geom-file (PMAXS)*, the *depletion-file* and the

maptab-file.

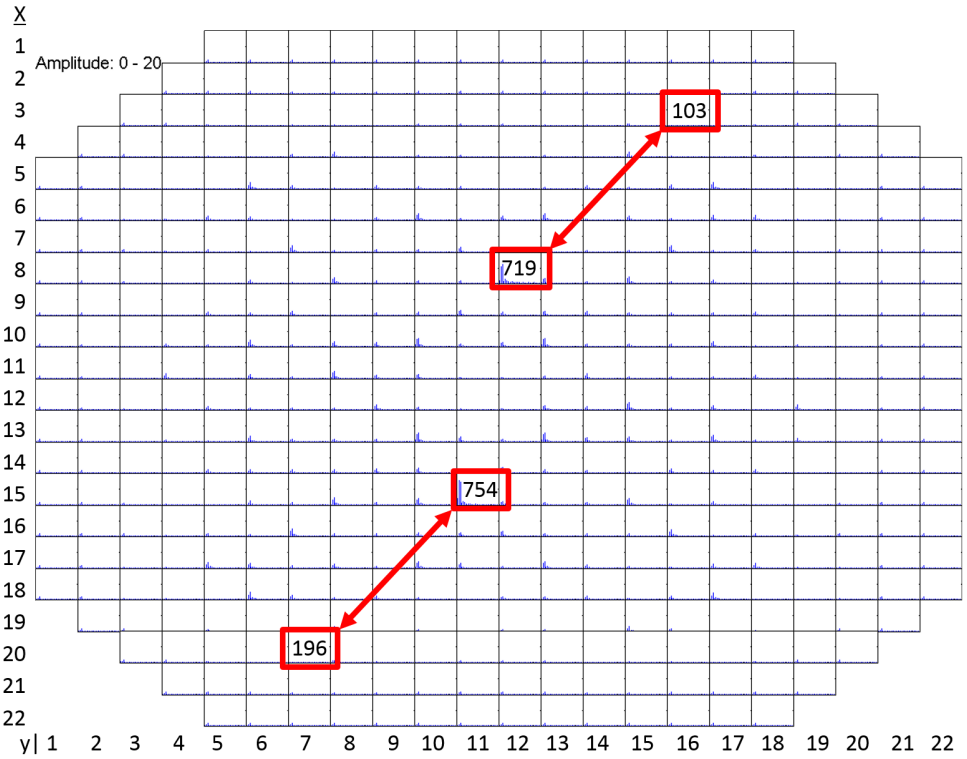

Figure 8.1: Study Case: rearrangement of channels.

8.2 Simulation of the Study Case

Except from the exchange of these four channels, the steady-state and transient-simulation of the Study Case is performed according to the simulation of the O2-1999 feedwater transient with identical input parameters and identical boundary conditions.

The simulation results presented in Figure 8.2 are in good agreement with the measured data and no differences are visible for the first part of the transient until partial scram (t = 197.6s) occurs. After that, the evolution of the total reactor power with the new fuel element pattern shows a much lower oscillation amplitude compared to the measured power, Figure 8.3.

The results of the coupled simulation using the standard core pattern and the

results obtained by redesigning the core pattern are shown in Figure 8.4. This figure gives a detailed insight of the total reactor power time trend immediately after the partial scram. It is evident that the power evolution remained consistent according to the frequency, whereas the amplitude of the oscillation is significantly damped.

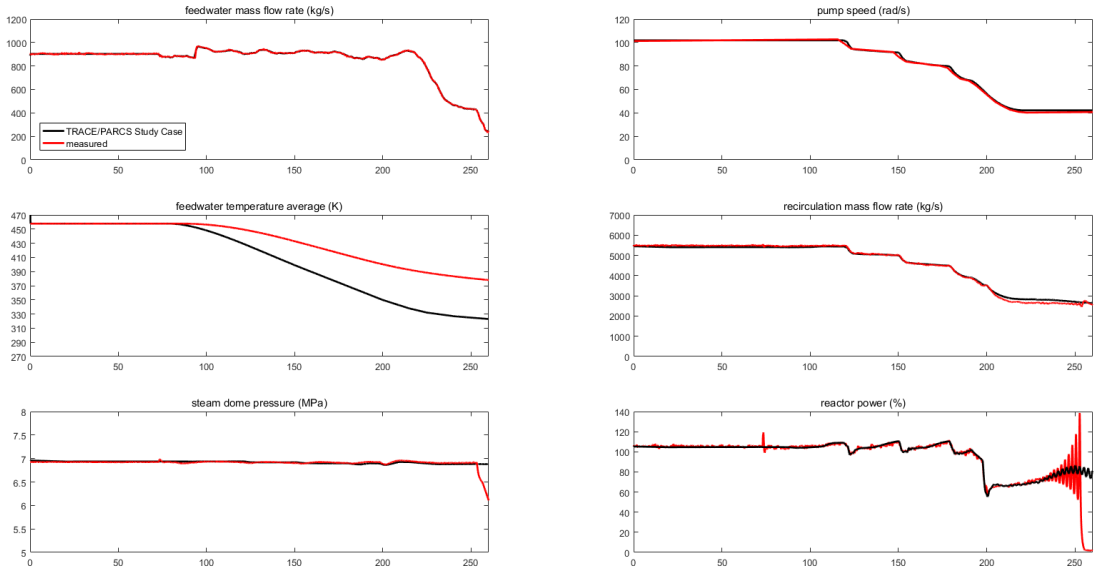

Figure 8.2: Study Case: TRACE/PARCS simulation vs. measurement.

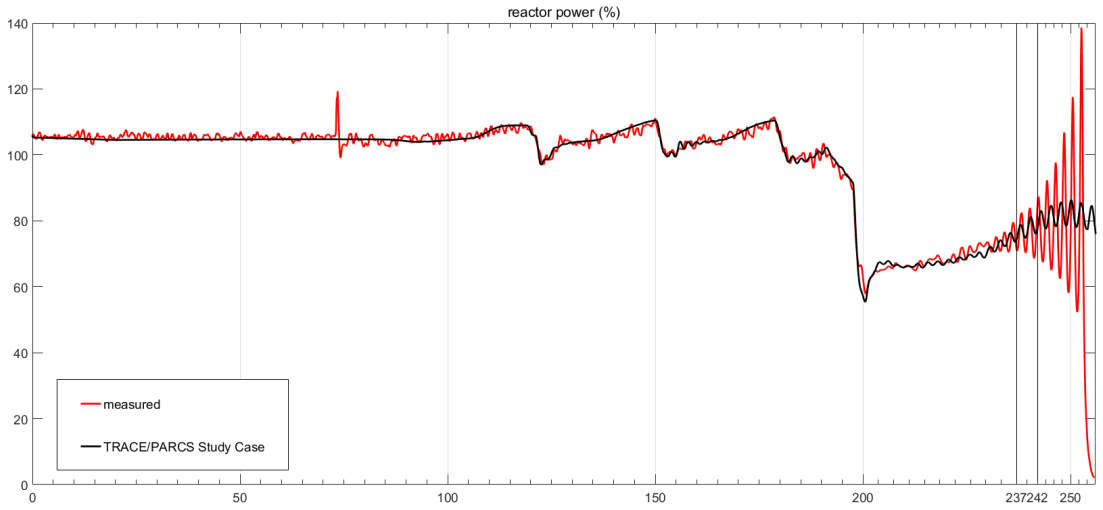

Figure 8.3: Study Case: total reactor power.

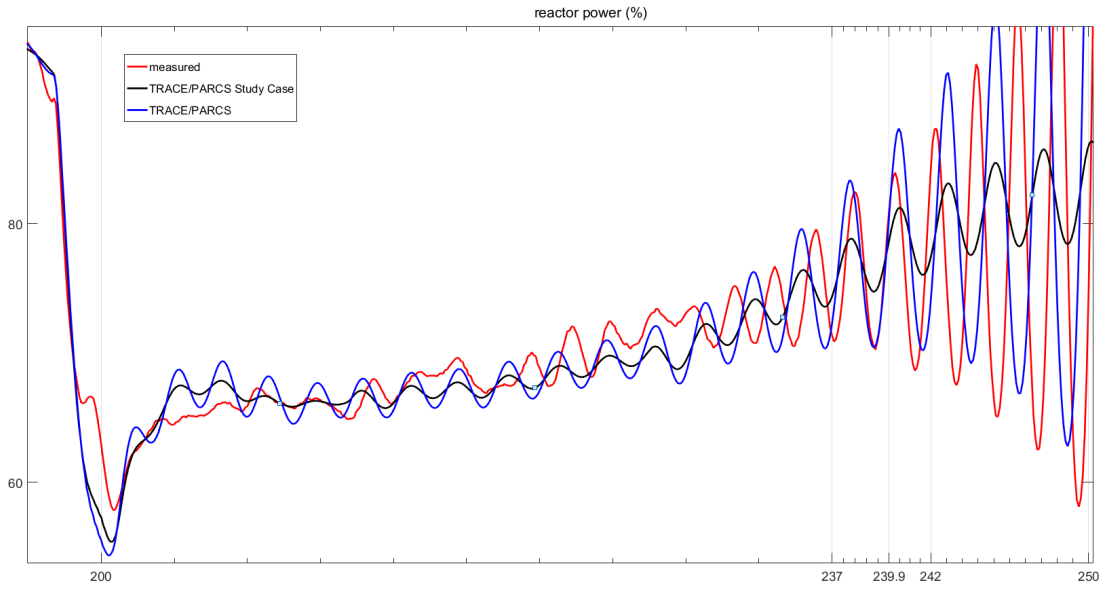

Figure 8.4: Total reactor power, detail: measured, TRACE/PARCS Study Case, TRACE/PARCS.

8.3 Application of the FFT - Method considering the Time-Dependent Evolution of the Oscillation for the Study Case

The evolution of the mass flow rate oscillation during the transient after the partial SCRAM is show in spectral representation for the time intervals 215 s - 220 s and 225 s - 230 s in Figure 8.5 and for the time intervals 235 s - 240 s and 245 s - 250 s in Figure 8.6. The mass flow rate oscillation amplitude is in this Study Case relatively low compared to the original TRACE/PARCS simulation. This can be additionally observed from the calculated relative amplitude scaling factors included in the plots at the top left corner, where, for example, the original simulation reaches in the last time frame (245 s - 250 s) an amplitude factor of 40, whereas the Study Case's amplitude factor is only 4.

According to section 7.1 describing in detail the applied methodology, the spectral analysis of the total mass flow rate for the time interval from 237 s to 242 s is shown in Figure 8.7 (bottom) in comparison with the relative channel power distribution (Figure 8.7, top). In contrast to the original simulation where the channels 719 and 754 showed noticeably higher amplitude peaks compared to the other hot channels, in this Study Case there is no channel outstanding in its mass flow rate oscillation amplitude. As a result it can be highlighted that the mass flow rate oscillations are more uniformly distributed over several channels and that there are no core channels with particularly extreme oscillations. The marked core channel numbers in Figure 8.7 are in a decreasing power order and it can be seen that the higher the power, the higher the oscillation, respectively the lower the power the lower the massflow rate oscillation. That was already described in chapter 7.2 but when the Tables 7.1 and 8.1, that give the values of the relative channel power in both simulations at the same time point, are compared, it becomes clear that in the Study Case the peak powers are lower and also more flattened in the hotter channels.
As stated in [1], the channel with the highest power is the most unstable one and

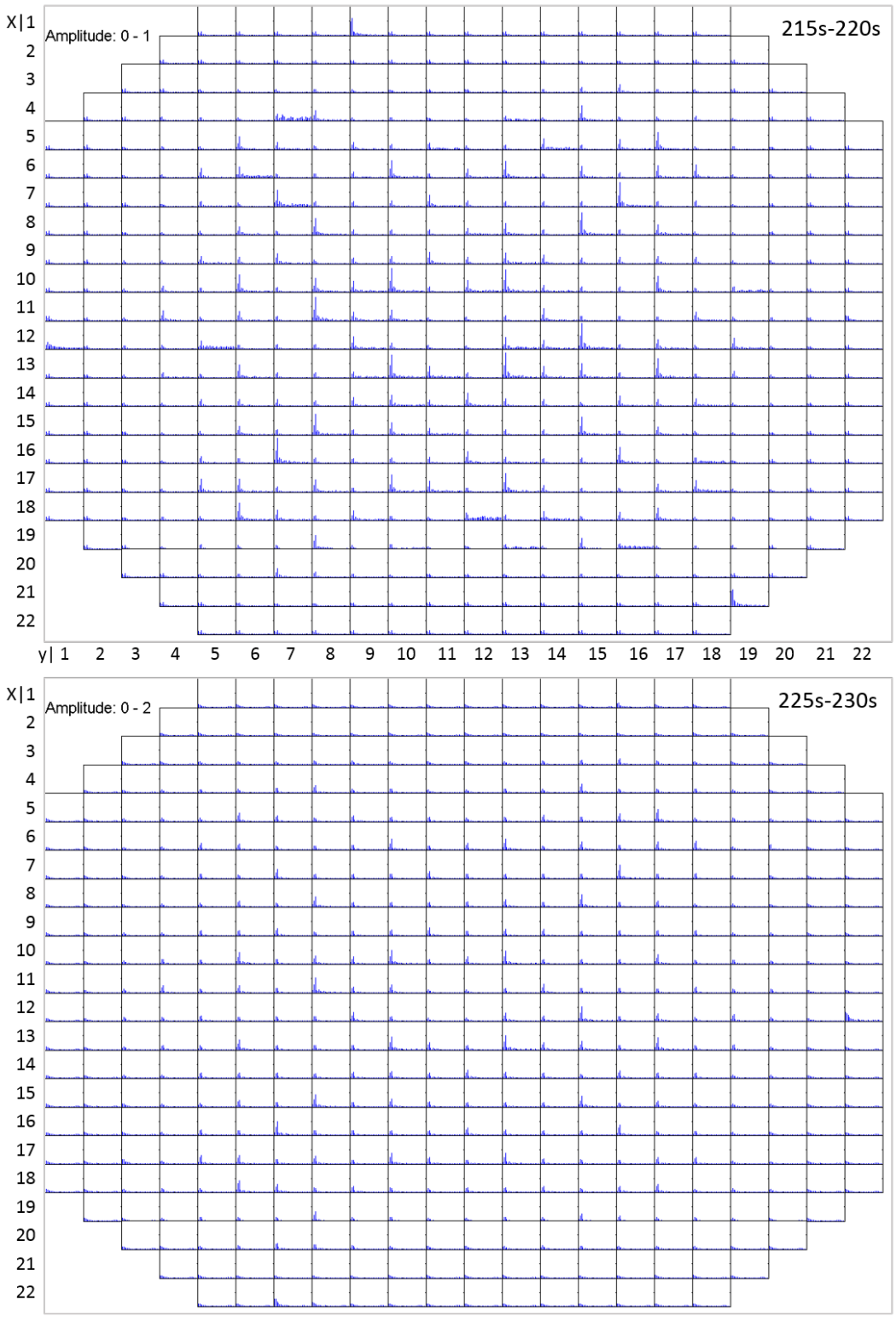

Figure 8.5: FFT applied on the mass flow at the channel inlet for the time frame 215 s - 220 s (picture top) and the time frame 225 s - 230 s (picture bottom).

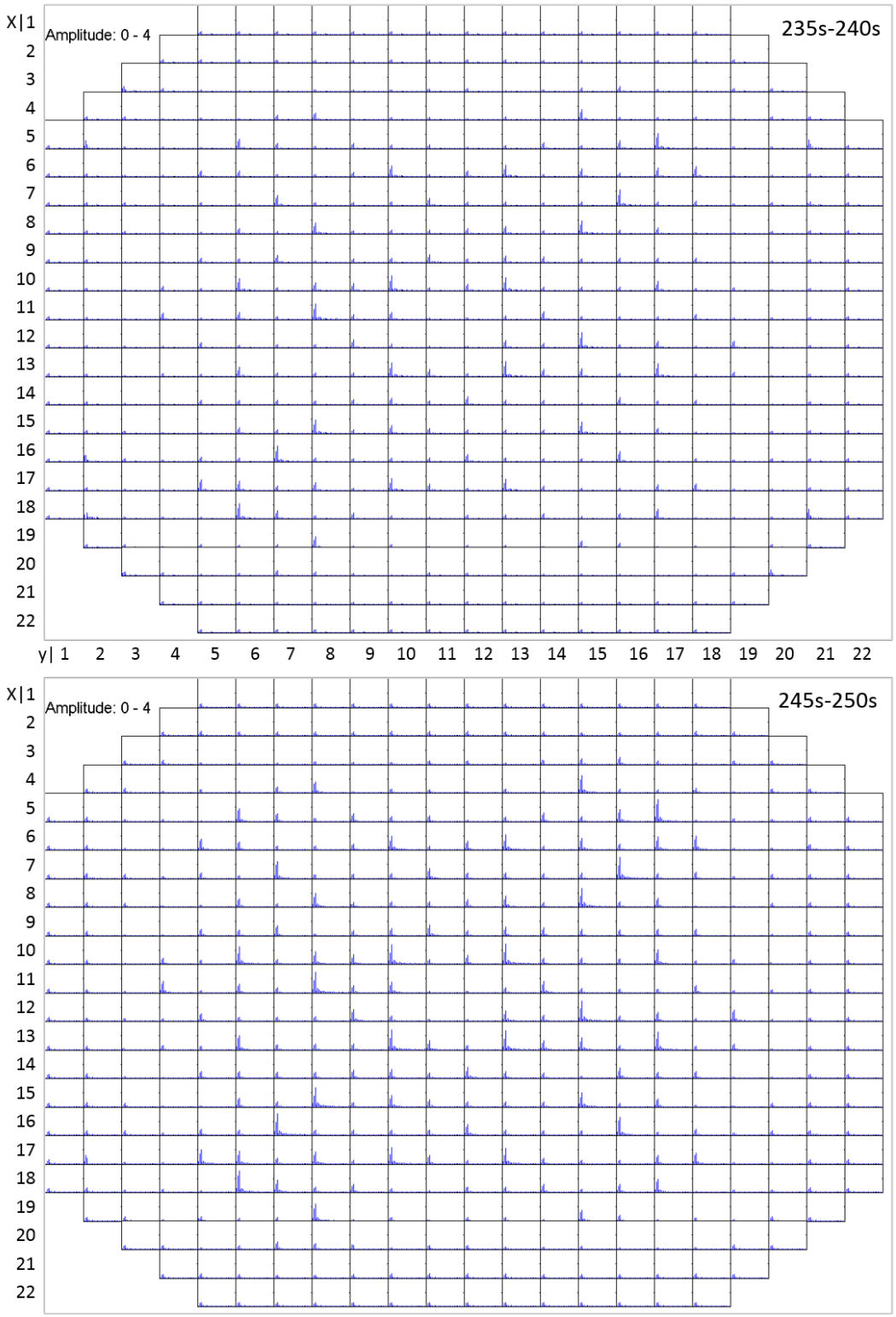

Figure 8.6: FFT applied on the mass flow at the channel inlet for time frame 235 s - 240 s (picture top) and the time frame 245 s - 250 s (picture bottom).

tends to dominate the overall response of the core. The importance of this fact can be demonstrated in the results presented here. The relative power of the hottest channel in the Study Case is merely 4 % lower than in the original TRACE/PARCS simulation, but the overall response of the system, that is, the total reactor power, has a remarkable lower oscillation amplitude. Therefore, the position of a channel together with its neighborhood of channels, has an important influence on BWR stability and the evolution of the transient.

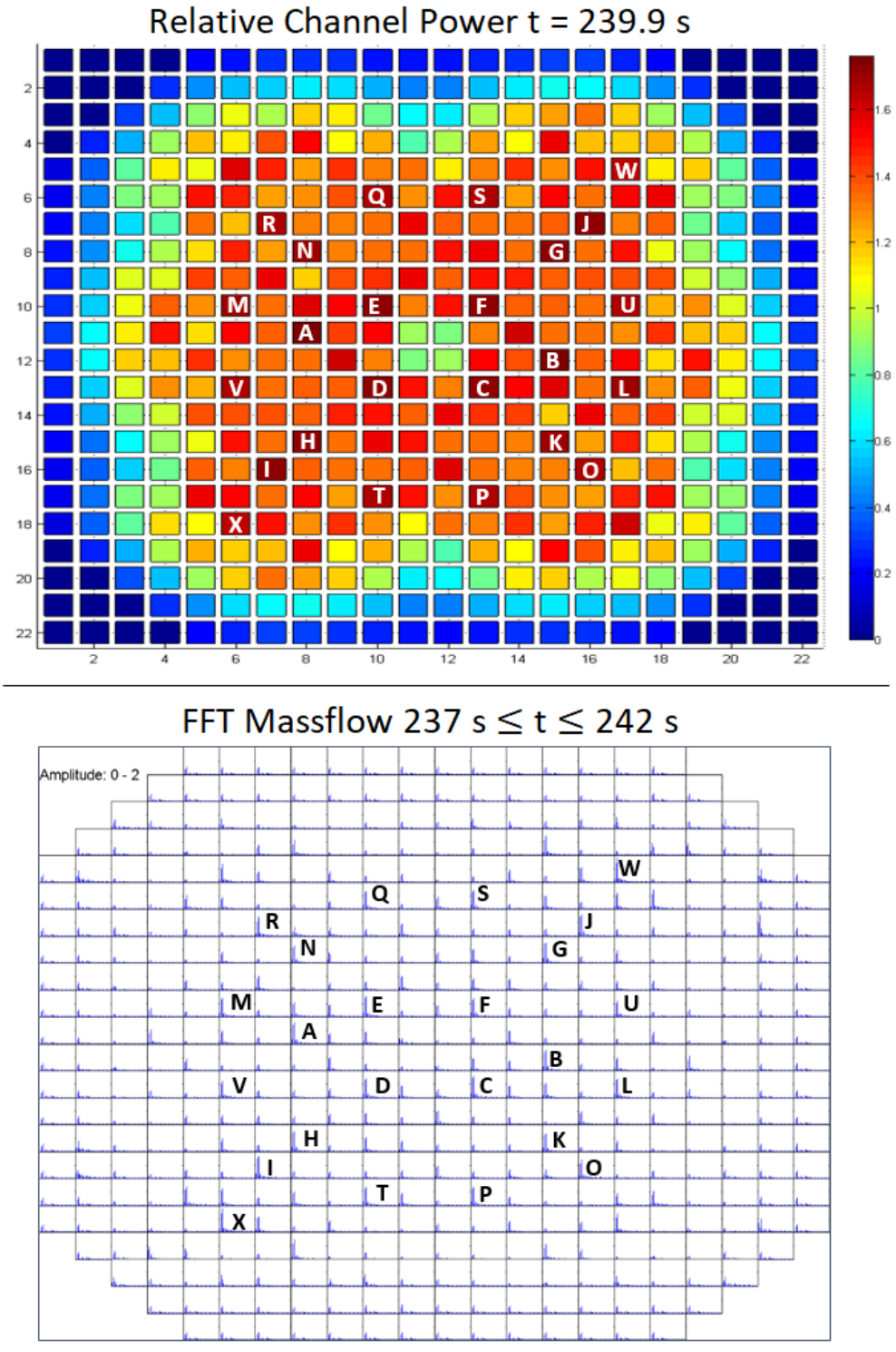

Figure 8.7: Relative channel power at time = 239.9 s (top) and FFT applied on the mass flow for the time interval 237 s - 242 s (bottom).

marker	relative power ratio	channel no.	x-pos.	y-pos.	assembly type
A	1.7600	734	11	8	QD
B	1.7599	739	12	15	QD
C	1.7314	745	13	13	QD
D	1.7310	744	13	13	QD
E	1.7239	728	10	10	QD
F	1.7294	729	10	13	QD

Table 8.1: Study Case: relative channel power ratio at time 239.9 s.

8.4 Application of the Phase Shift Analysis for the Study Case

The phase shift analysis of the mass flow rate oscillations performed according to the method described in section 7.3 is the main topic of this section. For the chosen time interval, 235 s - 240 s, the mass flow rate phase shift calculation is presented in Figure 8.8 with the upper plenum mass flow rate as a reference for the outlet channel mass flow rate (figure top), and the lower plenum mass flow rate as reference for the channel inlet mass flow rate (figure bottom).

One can see that the general behavior of the individual channels' phases has not changed compared to Figure 7.22 in section 7.3.4. The massflow rate at the upper plenum and at the channels outlet mass flow rates still have the same phase. A similar behavior is observed for the phase shift between the lower plenum and the channels inlets mass flow rates, where the central core channels phase is close to that of the lower plenum mass flow rate while the peripheral channels show an opposite behavior.
The channel 718 (x=8, y=8) and 426 (x=8, y=1) shows again a representative behavior for the central channels and respectively the periphery channels. A detailed analysis of these two channels is given next.

The absolute mass flow rate of the lower plenum, the mass flow rate through channel 718 at the inlet, the mass flow rate at equidistant distributed axial positions of the channel, the channel outlet and the mass flow rate of the upper plenum for the time frame from 230 s to 250 s is shown in Figure 8.9. It can be seen that the mass flow oscillates sinusoidally throughout the entire time interval in all observed positions but the mass flow trends in the upper and lower plenum are not smooth and also affect the channel mass flow at the outlet. The density wave travels through the channel and reaches a phase shift of 180° between inlet and outlet, compare Figure 8.10. The mass flow rate oscillations of the peripheral channel 416 are analogous to those observed in the original transient simulation and have throughout the channel the same phase, as shown in Figure 8.11. The mass flow rate of the peripheral channel outlet and of the upper plenum are in the

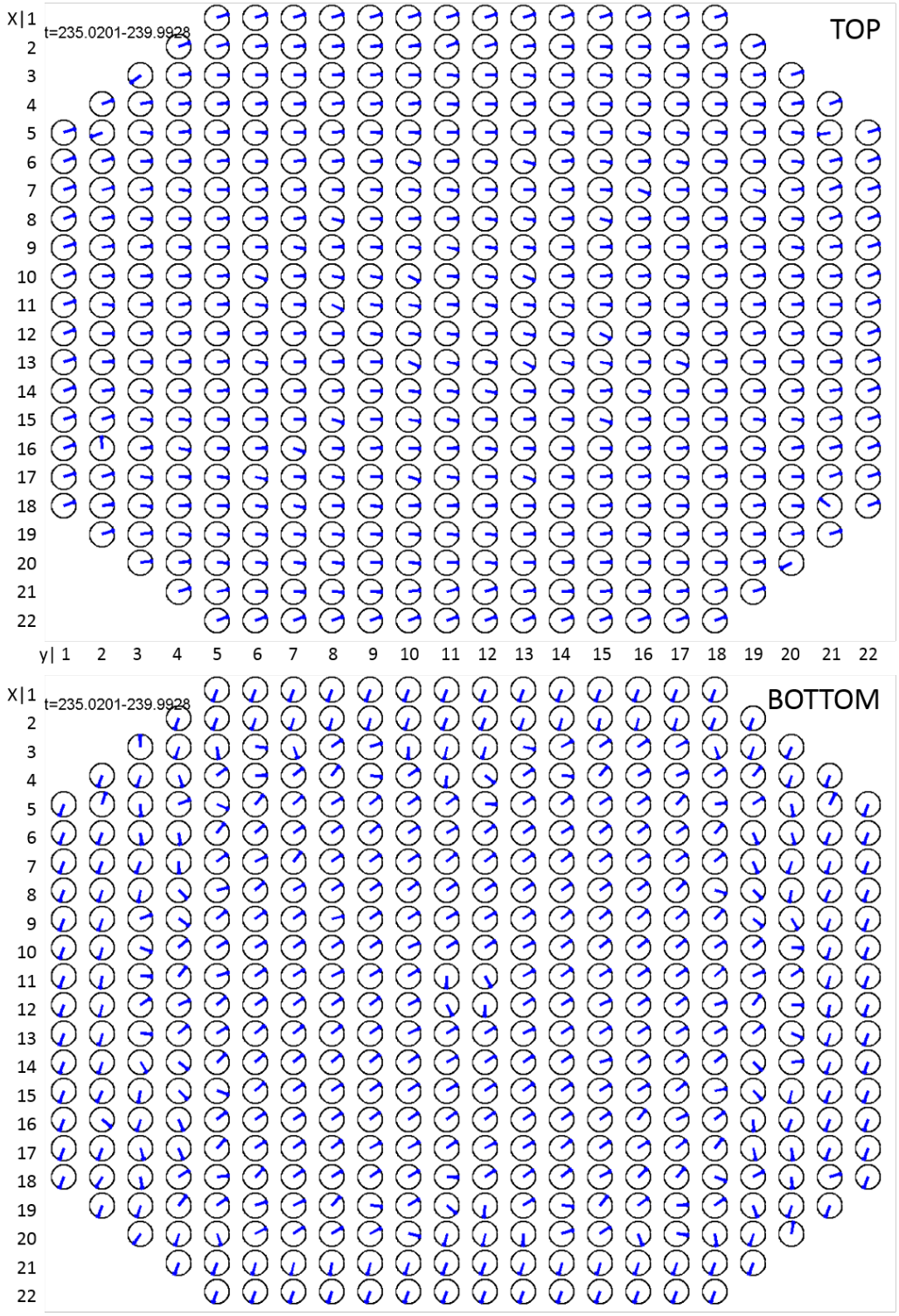

Figure 8.8: Phase shift of channel mass flows at the outlet relative to upper plenum (picture at top) and phase shift of channel mass flow at the inlet relative to lower plenum (picture at bottom), time frame 235 s - 240 s.

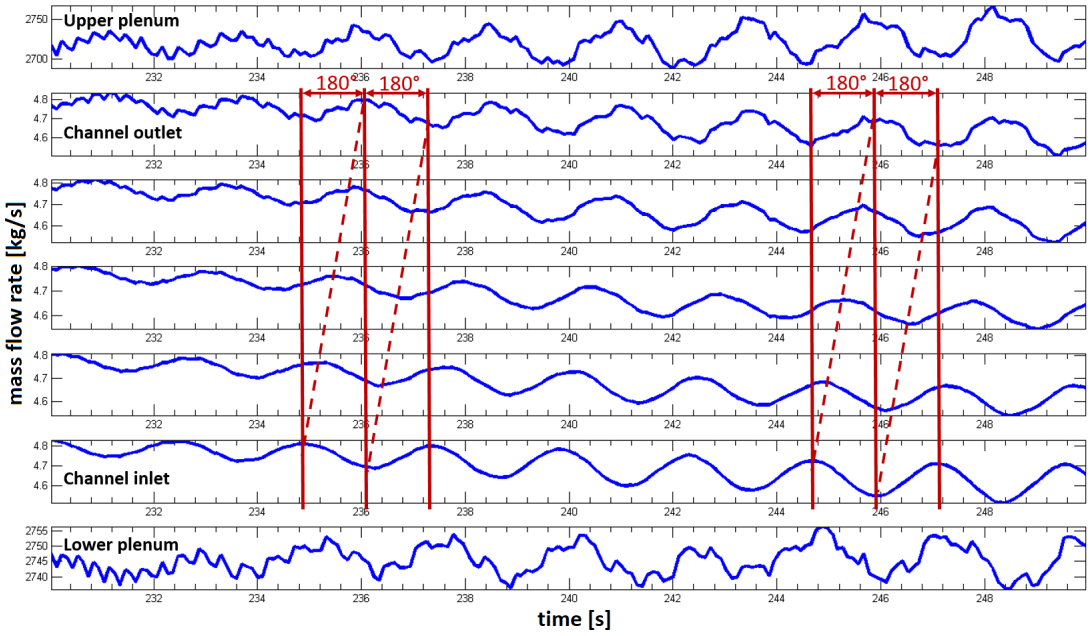

Figure 8.9: Absolute mass flow: lower plenum, channel 718, upper plenum

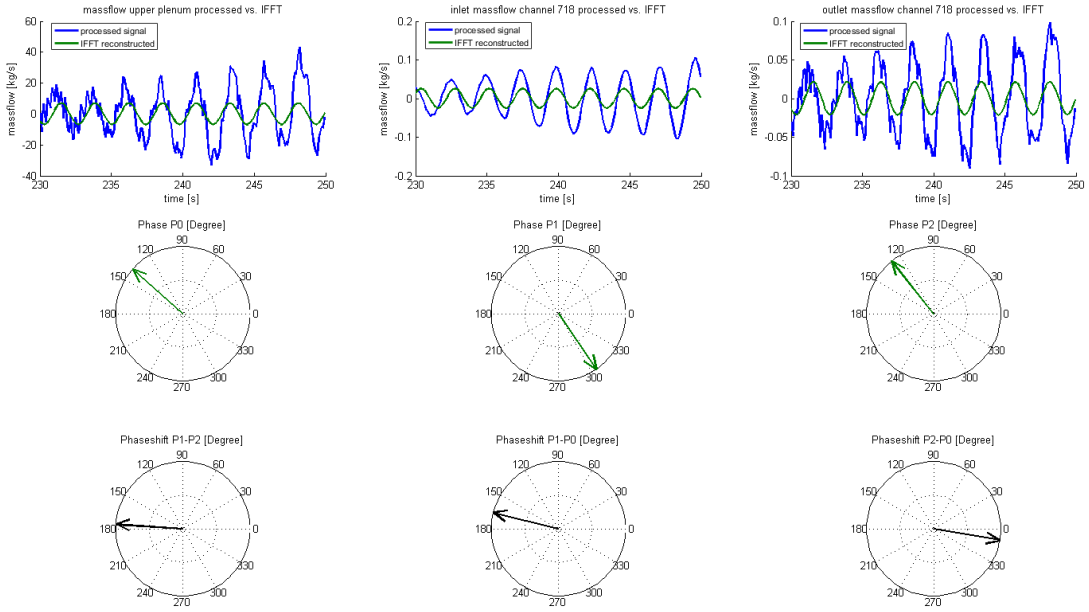

Figure 8.10: Phase shift calculation of the core channel 718 between its inlet and outlet mass flow.

same phase, while the phase of the peripheral channel inlet mass flow is shifted with respect to the lower plenum one. Though the mass flow rate oscillates sinusoidal it is apparent that the oscillation is not smooth.
The phase shift of the mass flow at the channel inlet between the central channel 718 and the periphery channel 416 is 210° as can be seen in Figure 8.12 and corresponds to the same value as in the original transient.
The mass flow rate oscillations of the bypass and the peripheral channel 416 are in phase, as can be observed in Figure 8.13. It has to be mentioned that the phase shift calculation, as it is here performed, does not match perfectly with the original very noisy measured signal.

As a summary for the Study Case with the rearranged core pattern, it can be noted that the local effects are equal to those observed in the original transient. The mass flow rate oscillations in the peripheral channels and in the bypass are quasi out-of phase with respect to the central core channels. The trends of mass flow oscillation in the upper and the lower plenum, in the bypass and in the peripheral channels are not smooth any more and show many intermediate peaks, highlighting a damped oscillation process. By only exchanging the position of four channels, the observed influence on the evolution of the power oscillation is very strong. The frequency of the total power oscillation remained the same as in the original simulation but the amplitude growth of the power oscillation is reduced clearly. From this is shown that the position of certain channels and the effect of the channels in their neighborhood are important on the global stability behavior of the reactor core.

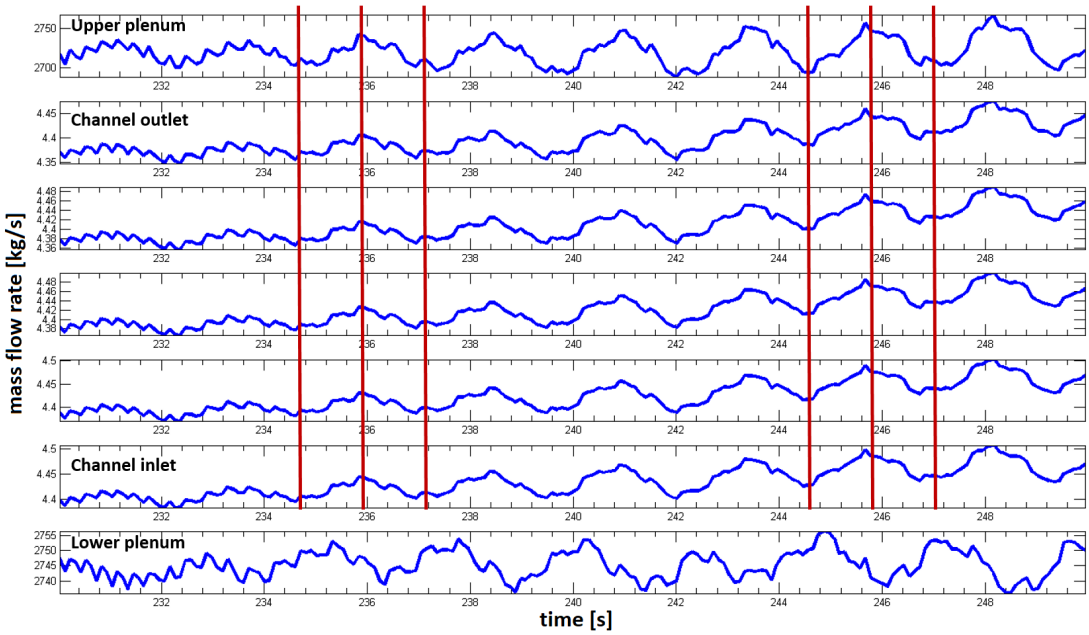

Figure 8.11: Absolute mass flow: lower plenum, channel 426, upper plenum.

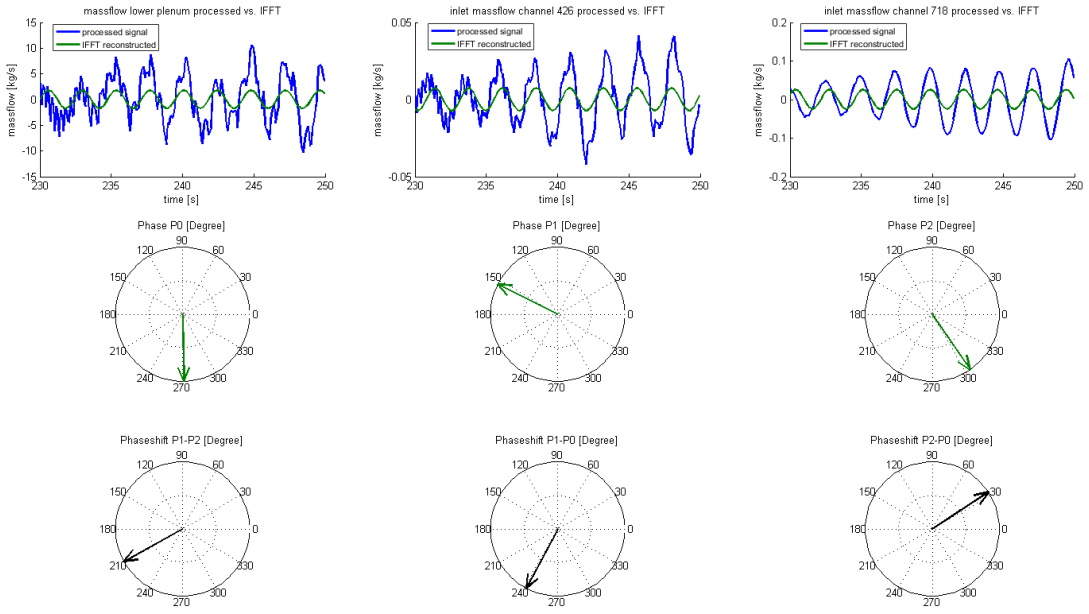

Figure 8.12: Phase shift calculation of inlet mass flow of channels 426 and 718 compared to lower plenum mass flow.

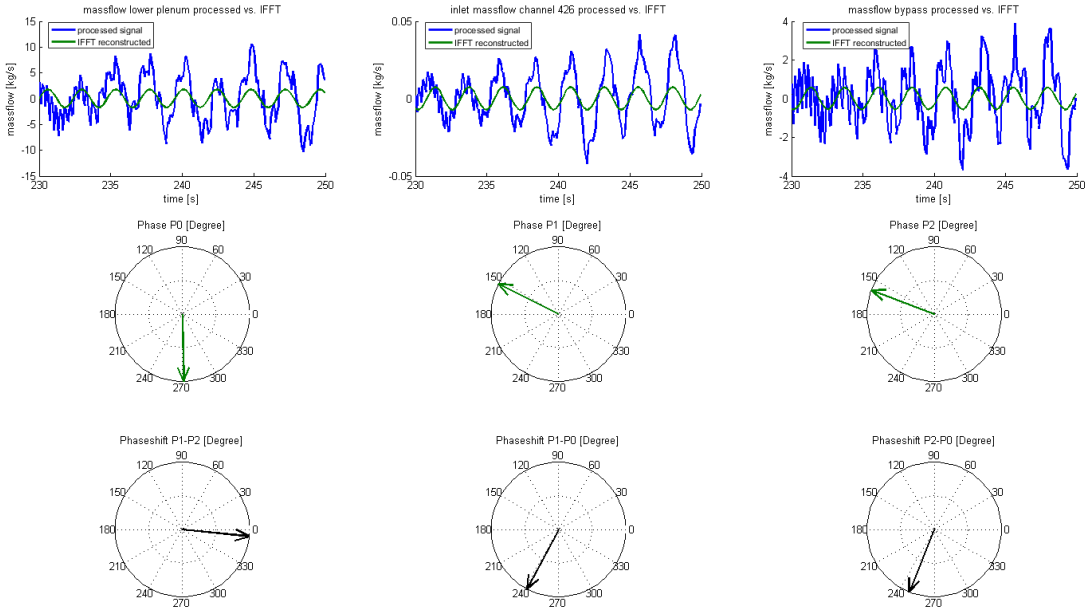

Figure 8.13: Phase shift calculation of inlet mass flow of channel 426 and the bypass inlet mass flow compared to lower plenum mass flow.

Chapter 9

Summary and Outlook

The OECD/NEA Oskarshamn-2 BWR stability benchmark provides the data used as a basis for the thesis work. A coupled TRACE/PARCS model with one-to-one core channel representation for the Oskarshamn-2 reactor was developed based on this information. The final model is not fine tuned to achieve the best possible reproduction of the measured power signal, and a trade-off in favor of decreasing the calculation time was necessary. This results consequently in a lower calculation accuracy, however, the simulation results showed good agreement with the measured data of the O2-1999 feedwater transient. Further, a new post-processing tool for the spectral analysis of simulation output parameters was developed and applied to the simulation results of the coupled TRACE/PARCS system code.

The post-processing tool uses the Fast-Fourier Transform algorithm to transform time-domain signals to the frequency domain. The methodology of the new analysis tool can be summarized as follows. A certain time interval of interest within the transient is selected; the time length of the time interval has to be selected in compliance with the oscillation frequency, for it should be at least twice the oscillation cycle time. The parameters that can be analyzed with the tool are arbitrarily selectable. The tool analyzes data in two-dimensional spacial direction, in either axial direction or planar direction. The algorithm performs a normalization of the data in order to eliminate global transient influences on the signals

as solely the oscillating component of the signals are subject to the analysis. The normalization of the data implies the advantage of directly comparable results in spectral representation.

In its application, the spectral analysis results show for each data node the oscillation amplitude to its corresponding frequency. Due to the comparability of the signals, statements can be made, at which local sector, where amplitude oscillations are higher compared to other sectors. The next step in the methodology is the prediction of the phase shift between the dominating oscillating components. The analysis detects to what extent parameter oscillations are shifted in time.

This two-step approach represents first, the detection of the relative amplitude distribution and, second, the determination of the phase shift of the dominating oscillation components. It thus delivers the basis for the interpretation of physical phenomena at a local scale. For this reason it becomes possible to "look" into the reactor core during a simulated instability occurrence of a BWR.

The analysis of the coupled TRACE/PARCS simulation data of the Oskarshamn-2 1999 feedwater transient was performed with the described method and it demonstrated the following physical phenomena.
The Oskarshamn-2 1999 feedwater transient is characterized as a in-phase oscillation type. The analysis of the fuel assembly power showed that all fuel elements have an uniform phase in the power oscillation whereas the analysis of the assembly mass flow rate showed a heterogeneous behavior. It was pointed out that a pattern of assemblies with striking mass flow rate oscillation amplitudes exist. This pattern corresponds to the assemblies relative power fraction this means those assemblies with high relative power have high mass flow rate oscillation amplitudes. The channel mass flow rate oscillations showed among all investigated parameters the clearest differences in the local expression of oscillation and is a governing factor for BWR instability due to the density wave mechanism.
An interesting observation was made in the quasi out-of-phase behavior of inlet

mass flow rate oscillations between the central core channels and peripheral core channels together with the bypass. Such a behavior suggests a positive feedback on the mass flow rate oscillations in the central core channels.

The influence of the two hottest channels with the highest amplitudes of the mass flow rate oscillations was studied qualitatively with respect to the over-all evolution of the total core power oscillation. These channels were rearranged in their radial core position, in the frame of a study case, by the exchange of location with two other channels. The coupled TRACE/PARCS simulation results of the O2-1999 feedwater transient with this redesigned core pattern reproduced the original core pattern transient simulation results with the difference that the total reactor power oscillation amplitude is noticeably lower although the oscillation frequency remained identical. The Fourier Transform based method was applied in the same manner and to the same local parameters as in the original core pattern simulation and showed the presence of a similar physical behavior. However, the mass flow rate oscillation amplitudes are lower as well as the relative power fraction of the hot channels. It is shown in this study, that the position of a channel in the core together with its neighboring channels has a remarkable influence on the evolution of a BWR instability transient.

As a proposal for further research, the described Fourier Transform based analysis method can be further extended on the basis of improvements in the algorithm. The accuracy of the calculation of the phase shift can be described with the rank correlation coefficient between the initial signal and the reconstructed dominant signal component. This would move the informative value of the method from a qualitative to a quantitative approach. Further, the method could profit from an improvement in the determination of the time interval length. The smallest time interval length that achieves sufficient accuracy in the outcomes of the method should be determined within the algorithm in order to obtain a more generally applicable tool.
If the analysis method can be improved to achieve a higher accuracy of the phase

shift calculation, while at the same time reducing the time interval length, the methodology can be applied to study other scenarios with higher complexity such as out-of-phase oscillation instability events.
Finally, for the extensive development of the analysis method, a bigger data base of simulation results is necessary for the confirmation of the observed phenomena. This can be done by a further refinement of the TRACE/PARCS model that provides a higher accuracy if compared to the measured data and avoids the possibility of discovered phenomena which are sensitive to the model refinement. Also simulation results obtained with other coupled simulation codes should be a basis for the improvement of the method.

Appendix A

Study of the Time Frame Length

Within the herein performed work, the core channel mass flow rate is the most investigated parameter. On this basis, the mass flow rate is the chosen parameter to show the influence of the selected time frame length on the analysis output of the FFT application and the calculation of the phase shift .
The starting point represents the characteristic frequency of this oscillation system and has a frequency of 0.4 - 0.5 Hz, resulting in a period length of 2.0 - 2.5 s. In order to capture an oscillation period, the selected time frame length must be at least 2.0 seconds. Further it is to remember that a discrete signal with a discrete number of sample points is considered. Therefore, the question regarding the selected time frame length includes the system inherent frequency and the number of sample points of the discrete signal.

A.1 FFT and Time Frame Length

The FFT (first-step) is applied on the mass flow rates at the inlet of the core channels in planar direction. The considered time interval starts from 2 seconds and is increased in 1 second steps up to 10 seconds. The results are represented in the Figures A.1 to A.9.
The general pattern of channels with striking mass flow rate amplitude oscillations

is apparent for all time frame lengths. However, the longer the time frame length is, the more sample points are processed and the sharper the dominant frequency strikes out. From that it can be concluded that the application of the FFT is also suitable for short time frame lengths. However, as the results of the FFT calculation are employed for the calculation of the phase shift (second-step) the focus for the determination of the time frame length is set in the following section A.2.

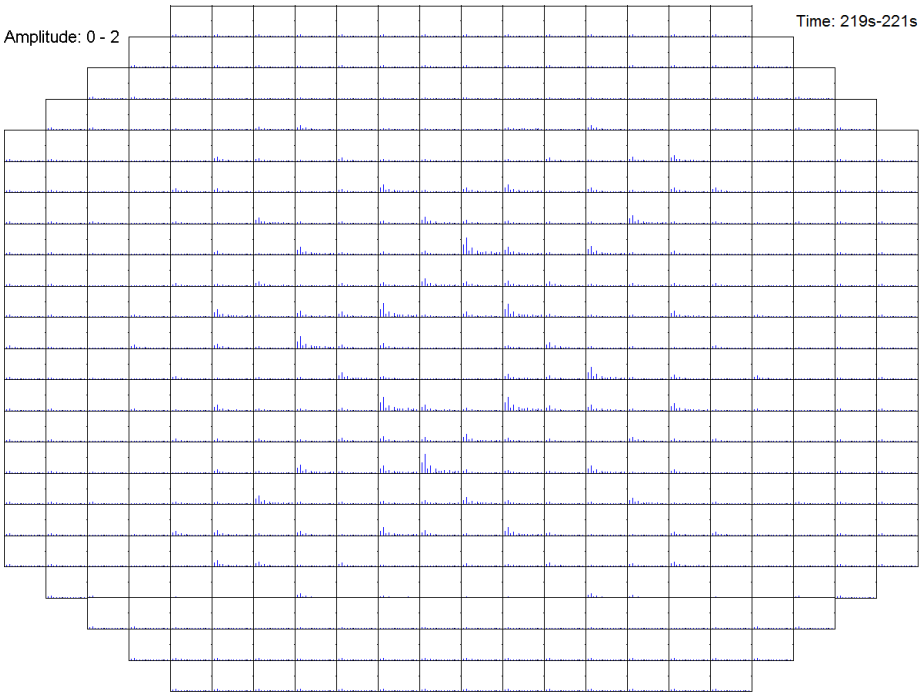

Figure A.1: FFT mass flow, z2, time: 219 s - 221 s, time frame length 2 s.

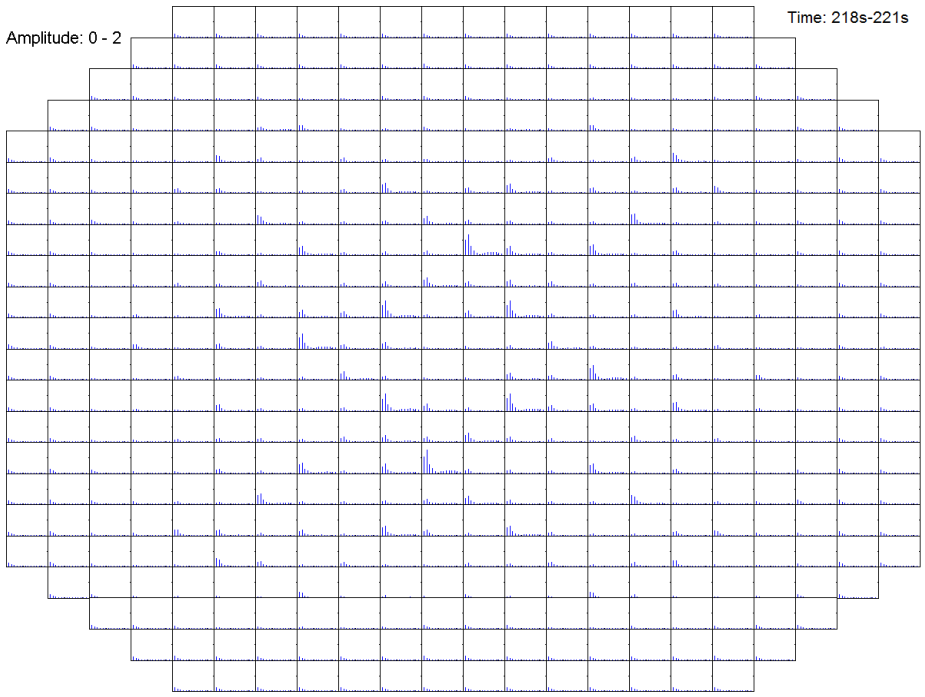

Figure A.2: FFT mass flow, z2, time: 218 s - 221 s, time frame length 3 s.

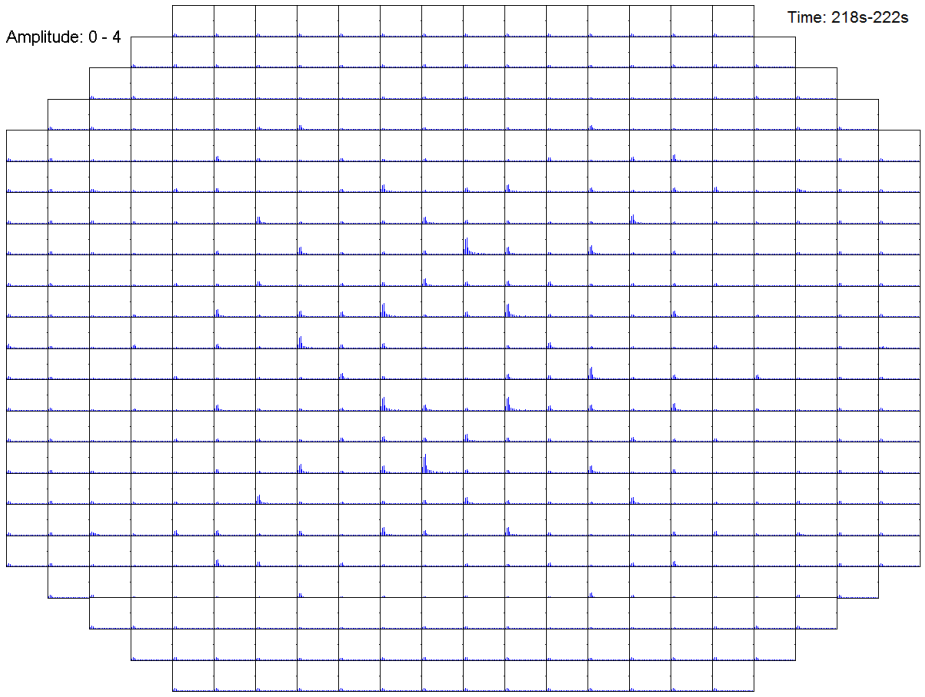

Figure A.3: FFT mass flow, z2, time: 218 s - 222 s, time frame length 4 s.

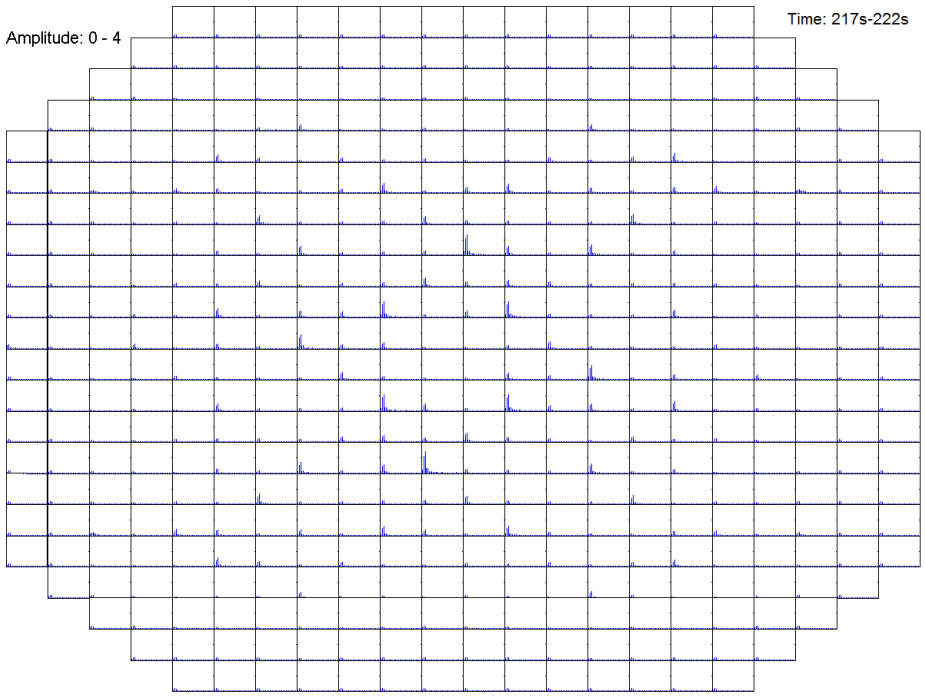

Figure A.4: FFT mass flow, z2, time: 217 s - 222 s, time frame length 5 s.

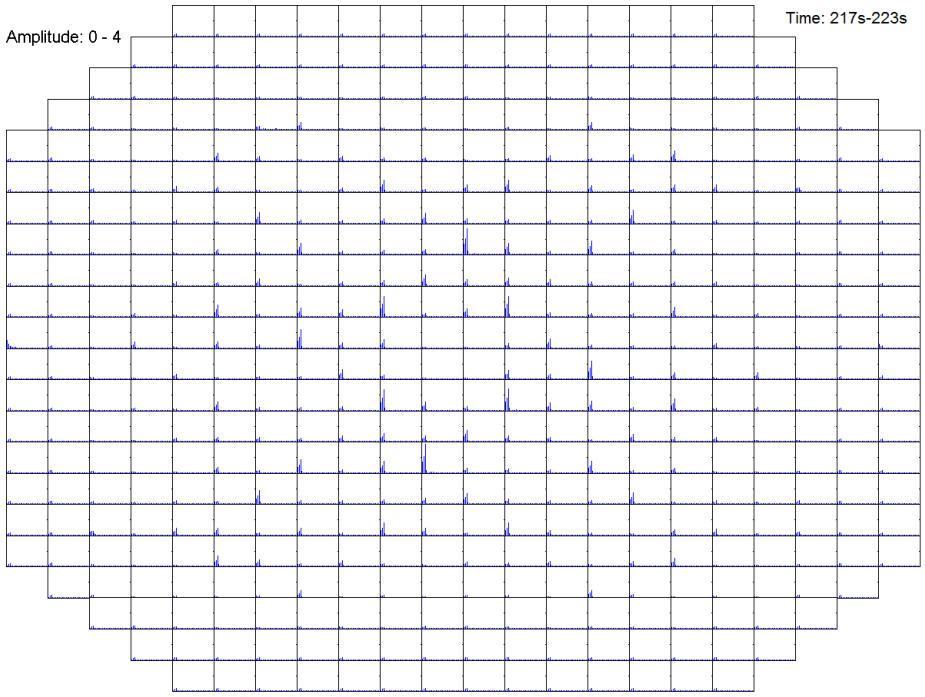

Figure A.5: FFT mass flow, z2, time: 217 s - 223 s, time frame length 6 s.

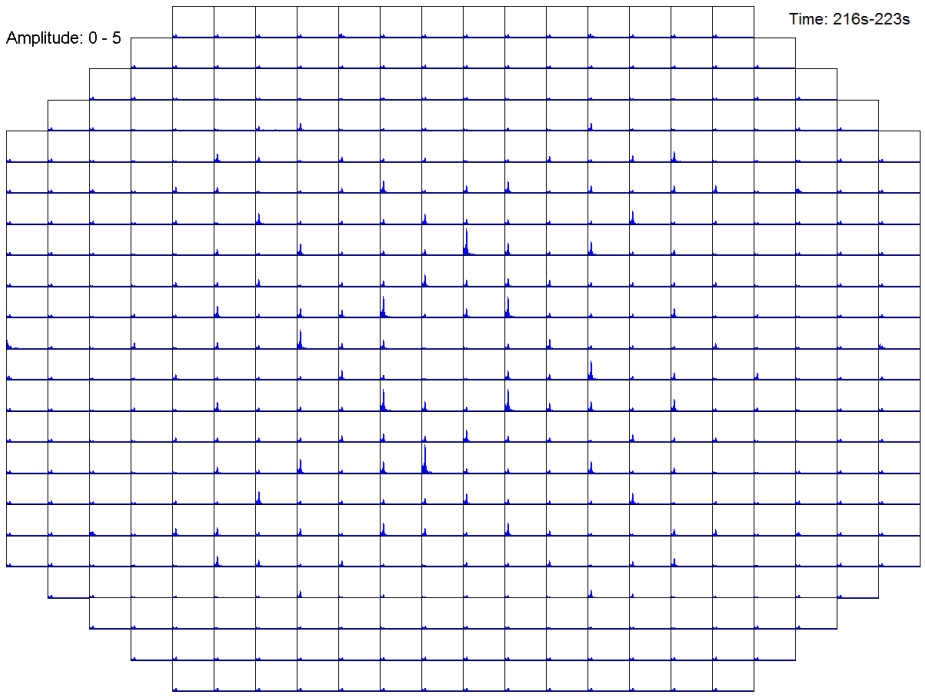

Figure A.6: FFT mass flow, z2, time: 216 s - 223 s, time frame length 7 s.

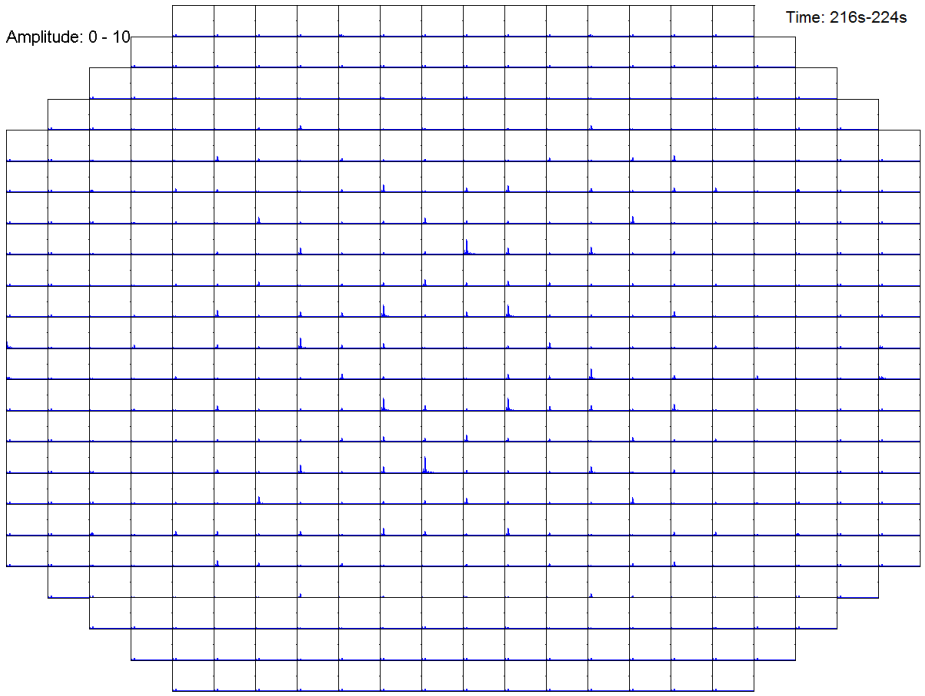

Figure A.7: FFT mass flow, z2, time: 216 s - 224 s, time frame length 8 s.

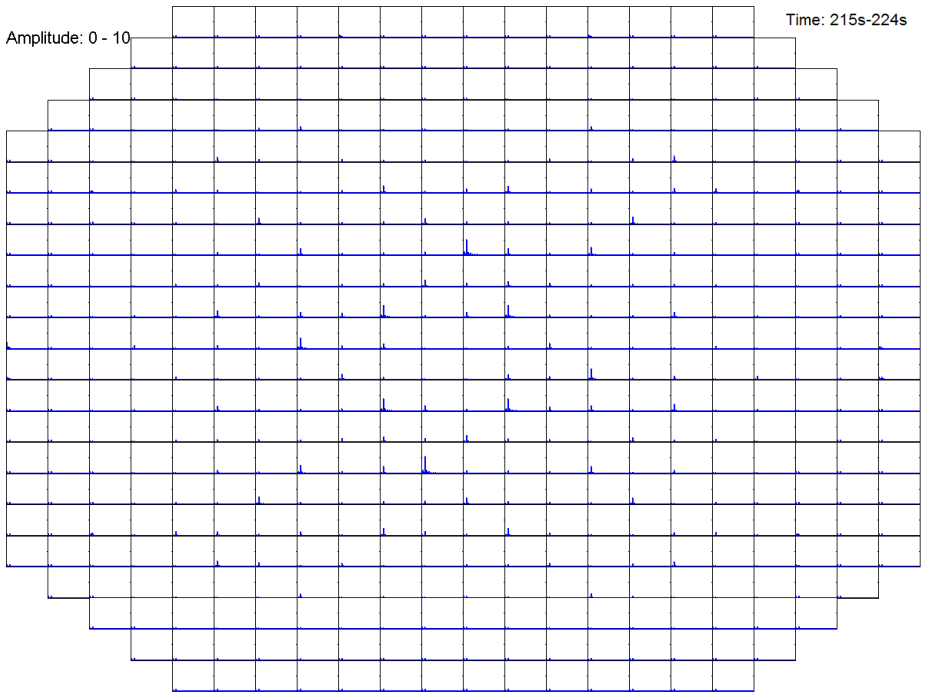

Figure A.8: FFT mass flow, z2, time: 215 s - 224 s, time frame length 9 s.

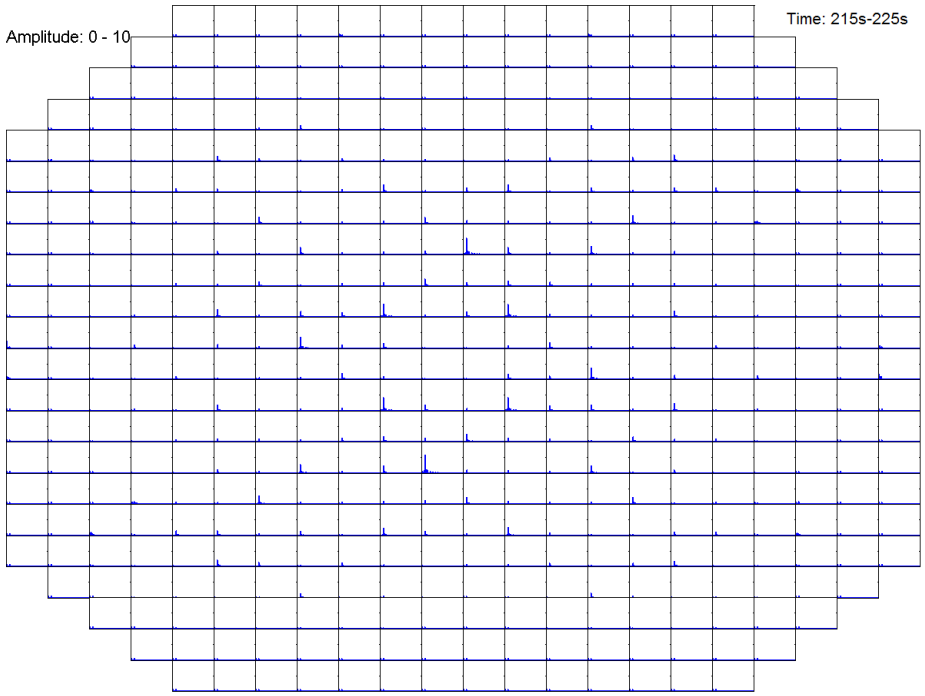

Figure A.9: FFT mass flow, z2, time: 215 s - 225 s, time frame length 10 s.

A.2 Phase Shift and Time Frame Length

The application of the FFT as the first step in the methodology is followed by the second step which is the calculation of the phase shift between the signals. Therefore, in each FFT output the frequency with the maximum amplitude together with the corresponding phase angle is determined. In the following it is estimated to what extend the dominant signal represents the original one with respect to the selected time frame length, however only considering the frequency and not according to the amplitude.
The considered time intervals are around the time point 240 s and spanning from 2 seconds up to 15 seconds with an 1 second steps increase as presented in the Figures A.10 to A.23. The figures are arranged in three rows and three columns. The first row shows the original signal (blue curve) compared to the re-transformed signal of the dominant component (green curve). The total reactor power (left column) is used as reference signal against which the other two signals are compared. These two signals correspond to the mass flow rates at the inlet of the channel 430 which represents a peripheral core channel, and the channel 728, a central core channel. The second row shows the phase angles, of the dominant component represented in a polar form with phase angles are named P0 for the reference signal, with P1 for the peripheral channel 430 and P2 for the central channel 728 respectively. The third row represents the phase shift of the two channel signals with respect to the reference signal and is termed "relative phase" in the following . The relative phase for channel 430 is P1-P0 while for channel 728 it is P2-P0.
A change of relative phase values with a change in the time frame length is evident for short time frame lengths of 2 s and 3 s. From time frame lenght 4 s on and larger, the changes in the value of the relative phase become relatively small. From this qualitative consideration a time frame length of 5 s, that corresponds to 2 oscillation periods, is regarded as sufficiently long.
Further considerations between the re-transformed signal of the dominant component and the original signal show that the re-transformed frequency agrees only to a limited degree. However, a quantitative evaluation can not be performed within the scope of this work and is subject to possible future work.

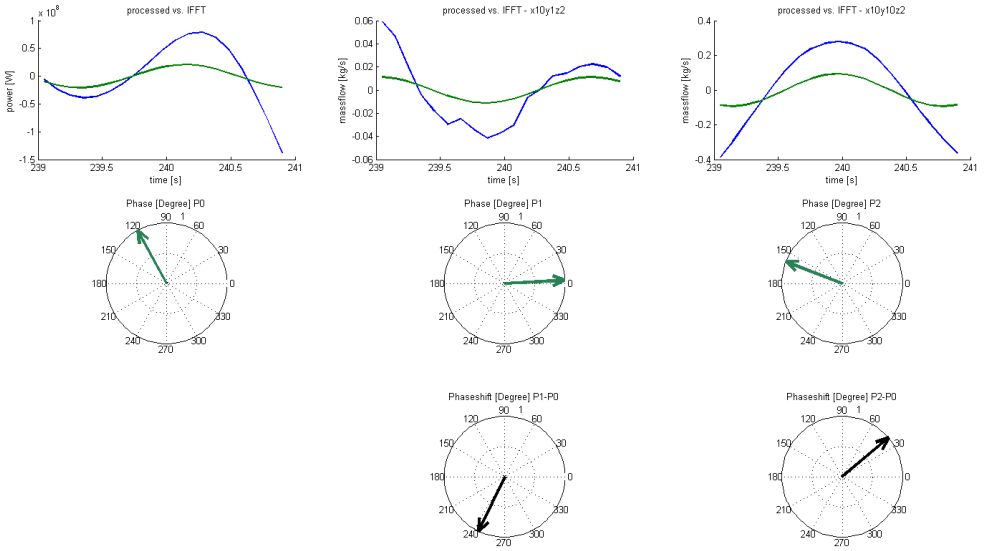

Figure A.10: Phase shift mass flow, time frame length 2 s, channel 430 (x10, y1, z2) and channel 728 (x10, y10, z2)

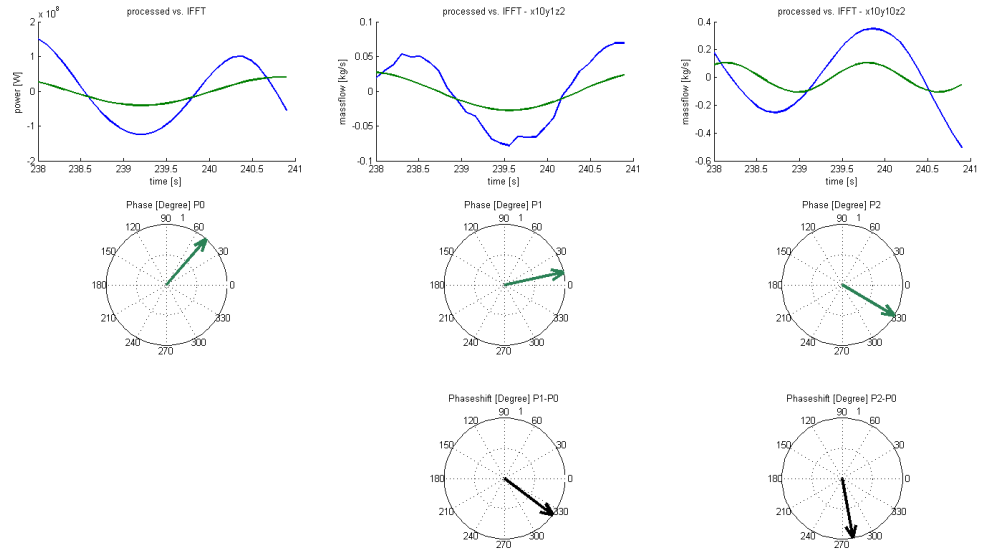

Figure A.11: Phase shift mass flow, time frame length 3 s, channel 430 (x10, y1, z2) and channel 728 (x10, y10, z2)

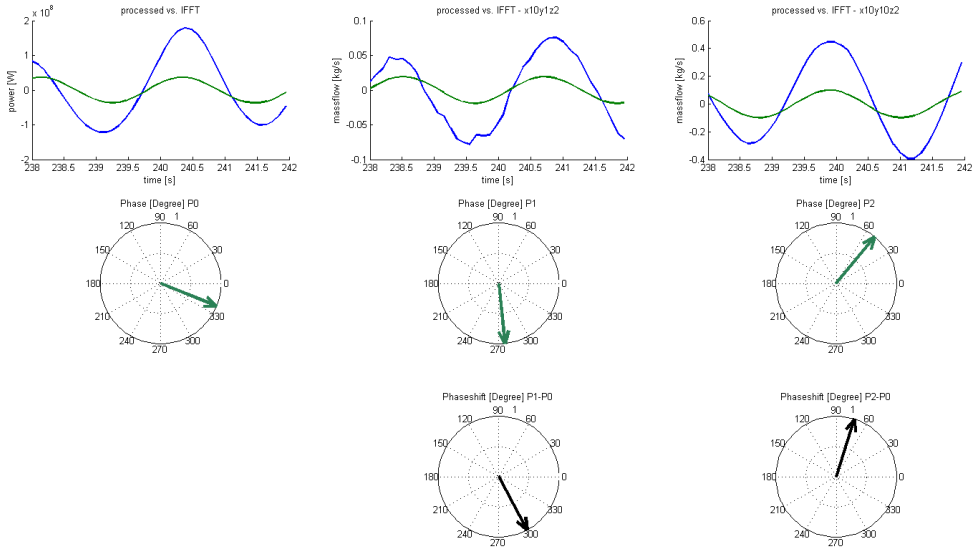

Figure A.12: Phase shift mass flow, time frame length 4 s, channel 430 (x10, y1, z2) and channel 728 (x10, y10, z2)

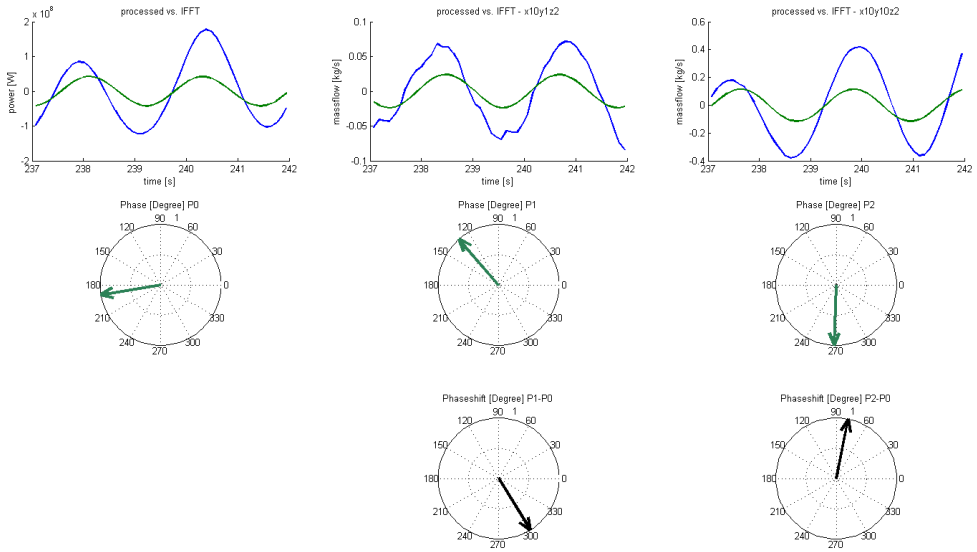

Figure A.13: Phase shift mass flow, time frame length 5 s, channel 430 (x10, y1, z2) and channel 728 (x10, y10, z2)

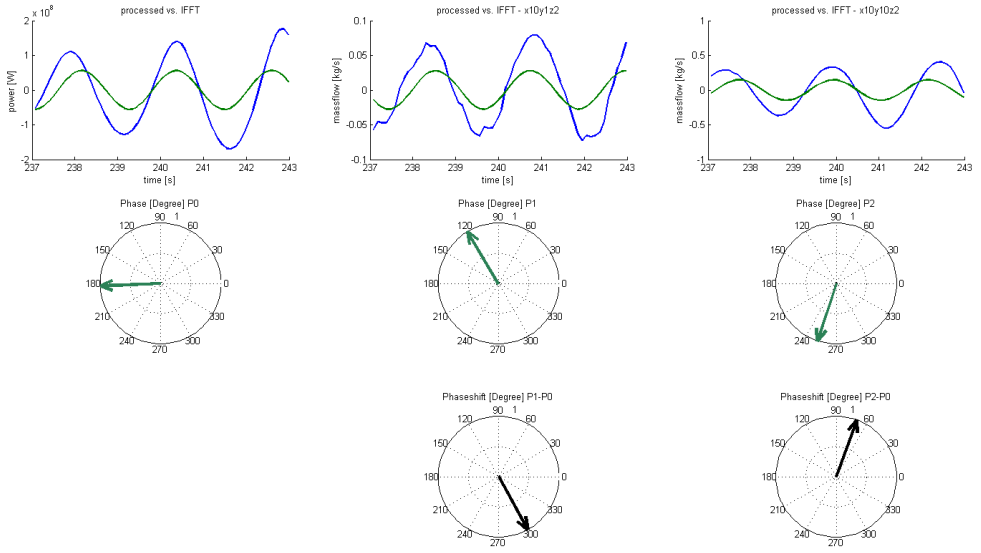

Figure A.14: Phase shift mass flow, time frame length 6 s, channel 430 (x10, y1, z2) and channel 728 (x10, y10, z2)

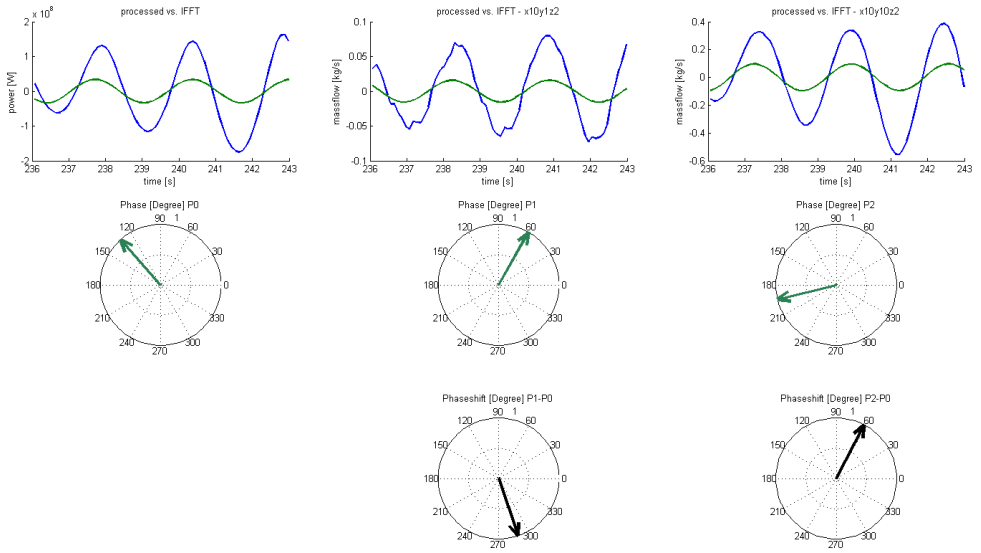

Figure A.15: Phase shift mass flow, time frame length 7 s, channel 430 (x10, y1, z2) and channel 728 (x10, y10, z2)

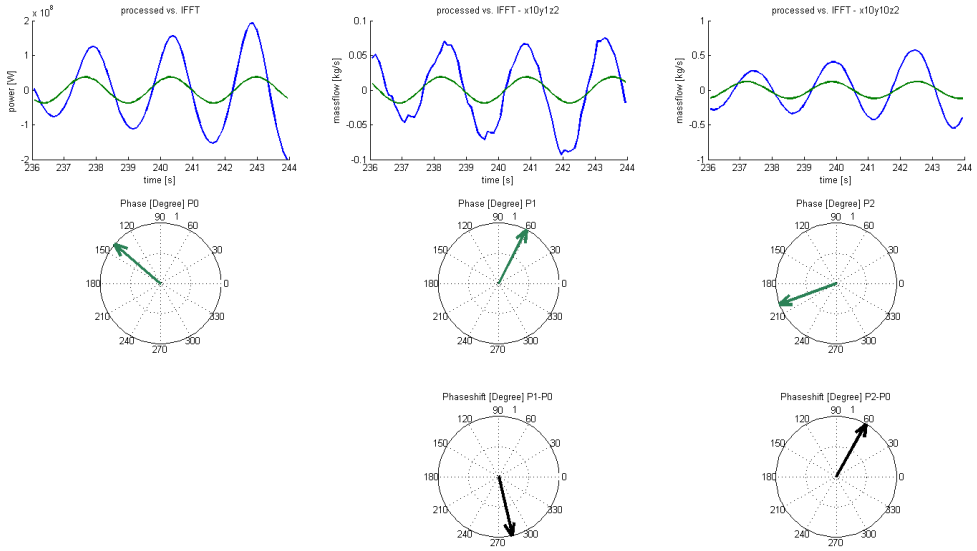

Figure A.16: Phase shift mass flow, time frame length 8 s, channel 430 (x10, y1, z2) and channel 728 (x10, y10, z2)

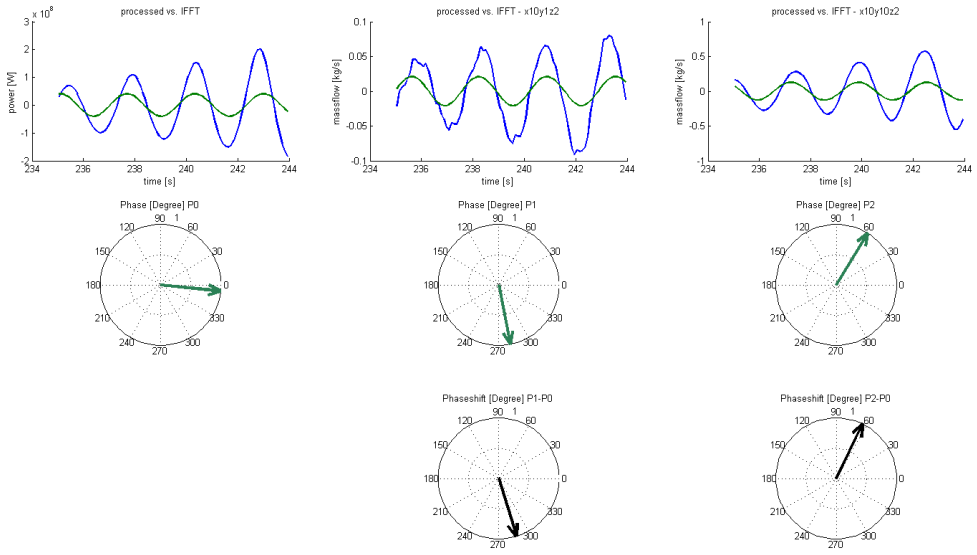

Figure A.17: Phase shift mass flow, time frame length 9 s, channel 430 (x10, y1, z2) and channel 728 (x10, y10, z2)

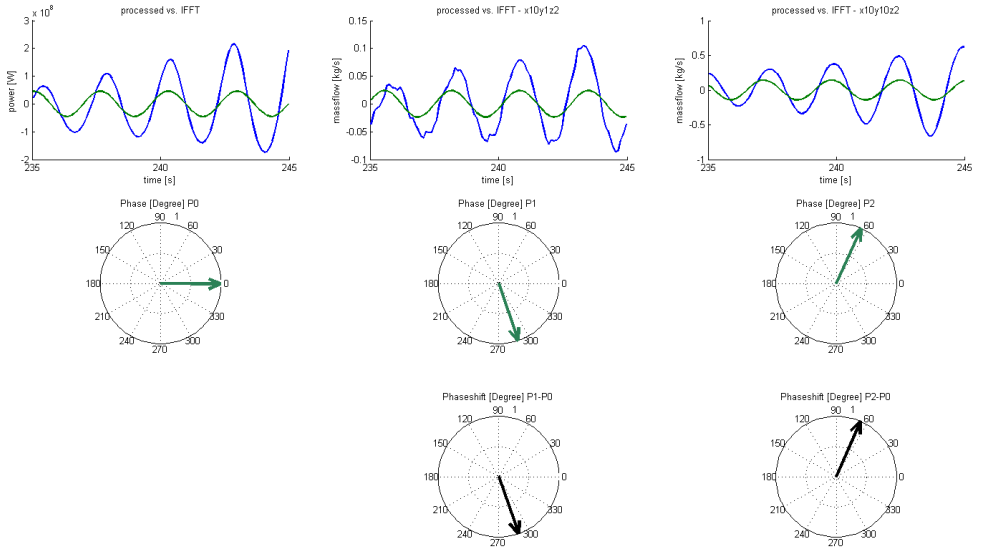

Figure A.18: Phase shift mass flow, time frame length 10 s, channel 430 (x10, y1, z2) and channel 728 (x10, y10, z2)

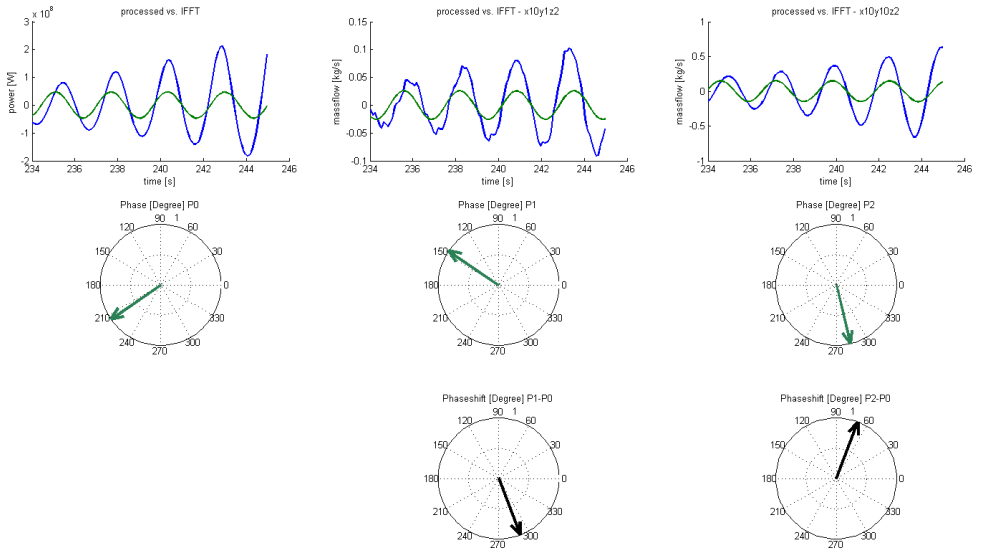

Figure A.19: Phase shift mass flow, time frame length 11 s, channel 430 (x10, y1, z2) and channel 728 (x10, y10, z2)

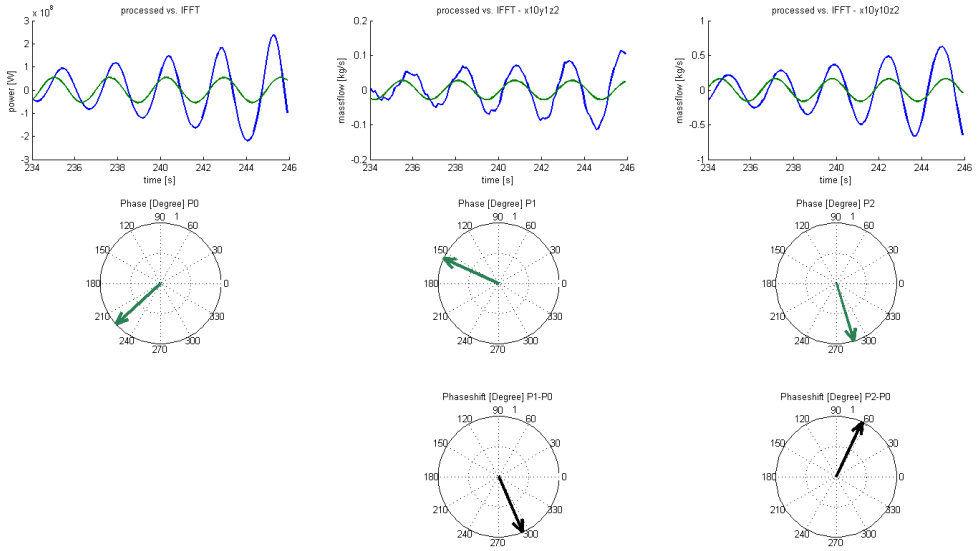

Figure A.20: Phase shift mass flow, time frame length 12 s, channel 430 (x10, y1, z2) and channel 728 (x10, y10, z2)

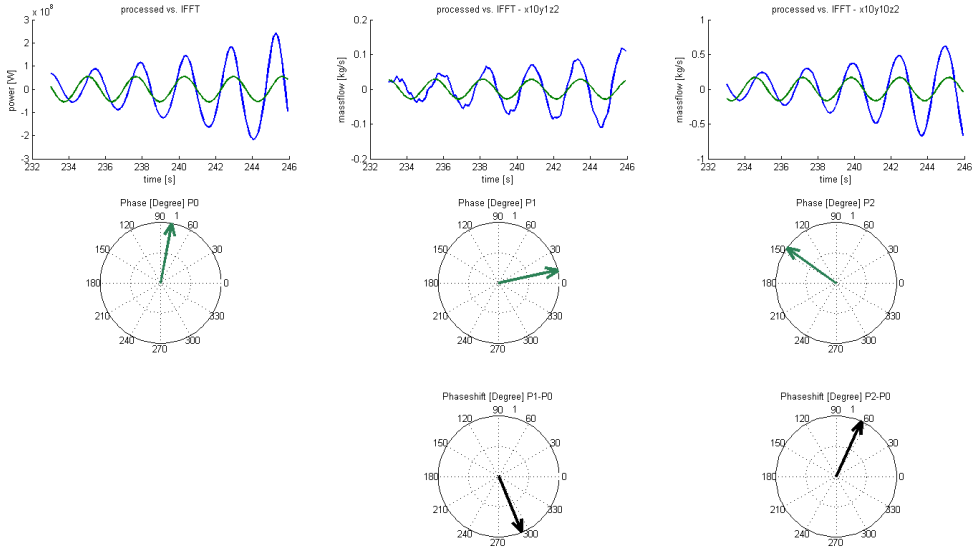

Figure A.21: Phase shift mass flow, time frame length 13 s, channel 430 (x10, y1, z2) and channel 728 (x10, y10, z2)

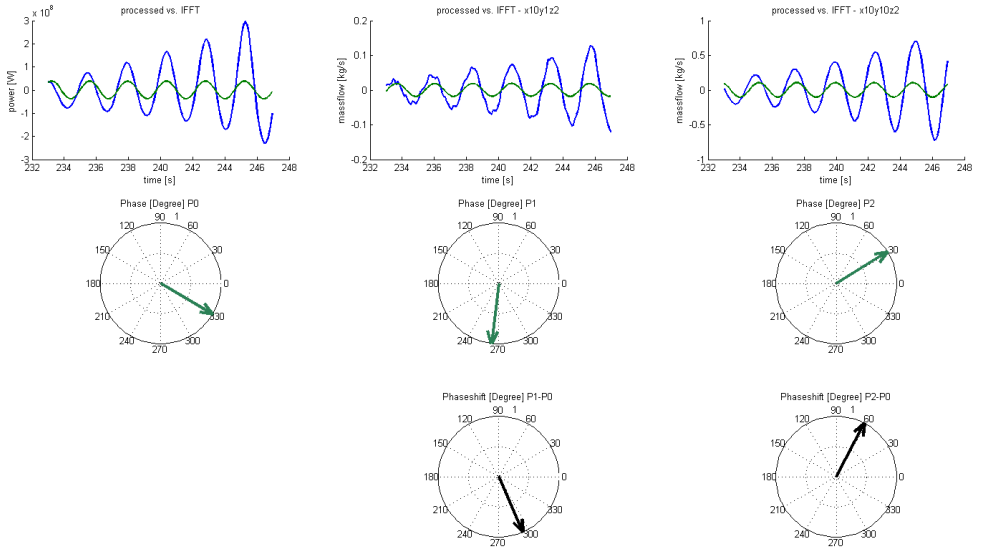

Figure A.22: Phase shift mass flow, time frame length 14 s, channel 430 (x10, y1, z2) and channel 728 (x10, y10, z2)

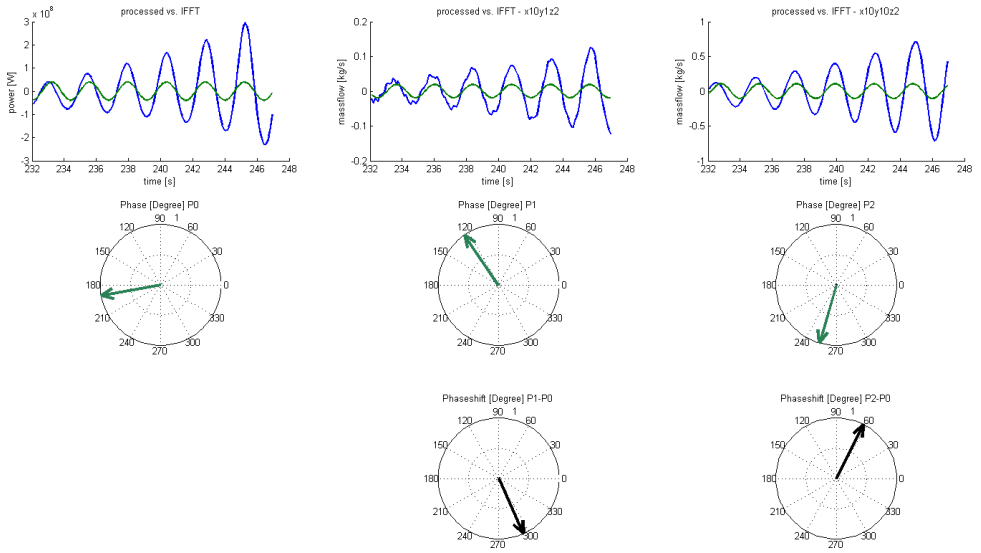

Figure A.23: Phase shift mass flow, time frame length 15 s, channel 430 (x10, y1, z2) and channel 728 (x10, y10, z2)

Bibliography

[1] J. March-Leuba. AN INTRODUCTION TO THE MECHANISMS LEADING TO DENSITYWAVE INSTABILITIES IN BWRs. *The 6th International Conference on Nuclear Thermal Hydraulics, Operations and Safety (NUTHOS-6) Nara, Japan, October 4-8, 2004. Paper ID. KN-09*, 2004.

[2] T. Kozlowski, S. Roshan, I. Gajev, T. Lefvert, C. Netterbrant, T. Downar, Y. Xu, A. Wysocki, K. Ivanov, J. Magedanz, M. Hardgrove, and J. March-Leuba. BWR Stability Event Benchmark based on Oskarshamn-2 1999 Feedwater Transient. *NEA/NSC/DOC(94)15*, 2014.

[3] U.S. Nuclear Regulatory Comission. *TRACE V5.0 USERS MANUAL Volume 2: Modeling Guidelines*, July 2011.

[4] F. Albrecht, S. Walser, S. Roshan, and R. Macián-Juan. Optimized Nodalization for the BWR Stability Analysis with TRACE/PARCS. In *Jahrestagung Kerntechnik / 45th Annual Meeting on Nuclear Technology in Frankfurt*, 2014.

[5] F. D'Auria, A. Lombardi-Costa, and A. Bousbia-Salah. THE BOILING WATER REACTOR STABILITY. *Natural circulation in water cooled nuclear power plants*, Annex 10, 2005.

[6] T. Kozlowski, A. Wysock, I. Gajev, Y. Xu, T. Downar, K. Ivanov, J. Magedanz, M. Hardgrove, J. March-Leuba, N. Hudson, and W. Ma. Analysis of the OECD/NEA Oskarshamn-2 BWR stability bechmark. *Annals of Nuclear Energy*, 67:4–12, 2014.

[7] J. March-Leuba and J. Rey. Coupled thermohydraulic-neutronic instabilities in boiling water nuclear reactors: a review of the state of the art. *Nuclear Engineering and Design*, 145:97–111, 1993.

[8] R. Hu. *STABILITY ANALYSIS OF THE BOILING WATER REACTOR: METHODS AND ADVANCED DESIGNS*. PhD thesis, Massachusetts Institute of Technology, 2010.

[9] R. Lahey and F. Moody. *The Thermal-Hydraulic of a Boiling Water Nuclear Reactor*. American Nuclear Society, 1993.

[10] U.S. Nuclear Regulatory Comission. *TRACE V5.0 USERS MANUAL Volume 1: Input Specification*, Dezember 2011.

[11] M. Avramova, A. Velazquez-Lozada, and A. Rubin. Comparative Analysis of CTF and Trace Thermal-Hydraulic Codes Using OECD/NRC PSBT Benchmark Void Distribution Database. *Science and Technology of Nuclear Installations*, 2013(725687), 2012.

[12] U.S. Nuclear Regulatory Comission. *TRACE V5.0 THEORY MANUAL*, May 2012.

[13] V. Seker T. Downar, Y. Xu. *PARCS v3.0 U.S. NRC Core Neutronics Simulator USER MANUAL*, 2012.

[14] Y. Xu, T. Downar, R. Walls, K. Ivanov, J. Staudenmeier, and J. March-Leuba. Application of TRACE/PARCS to BWR stability analysis. *Annals of Nuclear Energy*, 36:317–323, 2009.

[15] J.H. Mahaffy. The advantages and limitations of the SETS method. In *International Conference on Numerical Methods in Nuclear Engineering, Canadian Nuclear Society, Montral, Quebec, pp28-39*, 1983.

[16] J.H. Mahaffy. Numerics of codes: stability, diffusion, and convergence. *Nuclear Engineering and Design*, 145:131–145, 1993.

[17] F. Albrecht. Optimization of a neutronkinetic model for the simulation of a boiling water reactor using the system-codes TRACE/PARCS. Semesterarbeit, TU München, 2013.

[18] T. Kozlowski I. Gajev, W. Ma. Space time convergence analysis on BWR stability using TRACE/PARCS. *Annals of Nuclear Energy*, 51:295–306, 2013.

[19] I. Gajev, T. Kozlowski, Y. Xu, and T. Downar. Sensitivity and Uncertainty of the OECD Benchmark Ringhals-1 TRACE/PARCS Stability Prediction. *Nuclear Technology*, 180:383–398, 2012.

[20] I.Gajev, W.Ma, and T.Kozlowski. Sensitivity analysis of input uncertain parameters on BWR stability using TRACE/PARCS. *Annals of Nuclear Energy*, 67, May 2014.

[21] Mathworks Documentation. Fast fourier transform http://de.mathworks.com/help/matlab/ref/fft.html, January 2015.

[22] M. Sek. Frequency analysis, fast fourier transform, frequency spectrum http://www.staff.vu.edu.au/msek/frequency

[23] F. Albrecht. Entwicklung einer Analysemethode für die Ermittlung des lokalen Leistungsverhalten in Siedewasserreaktortransienten. Master's thesis, TU München, 2014.

[24] T. Kozlowski, S. Roshan, T. Lefvert, T. Downar, Y. Xu, A. Wysocki, K. Ivanov, J. Magedanz, M. Hardgrove, C. Netterbrant, J. March-Leuba, N. Hudson, O. Sandervåg, and A. Bergman. TRACE/PARCS VALIDATION FOR BWR STABILITY BASED ON OECD/NEA OSKARSHAMN-2 BENCHMARK. *The 14th International Topical Meeting on Nuclear Reactor Thermalhydraulics, NURETH-14 Toronto, Ontario, Canada,*, NURETH14-366, 2011.

[25] OECD-NEA. International Workshop on Boiling Water Reactor Stability. Proceedings of the OECD/CSNI International Workshop on Boiling Water

Reactor Stability, Brookhaven, Hotsville NY, October 17th-19th 1990. CSNI Report 178.

[26] F. D'Auria, W. Ambrosini, and T. Anegawa. State of the Art Report on Boiling Water Reactor Stability, 1997. OECD/GD(97)13.

[27] Y. Xu, T. Downar, K. Ivanov., J. Veldovi, A. Petruzzi, and J. Staudenmeier. Analysis of the OECD/NEA Ringhals instability benchmark with TRACE/PARCS. *ANS Mathematics and Computation Meeting, Avignon, France*, 2005.

[28] Y. Xu and T. Downar. *GenPMAXS Code for Generating the PARCS Cross Section Interface File PMAXS*. Purdue University, School of Nuclear Engineering, November 2006.